

POLITECNICO DI TORINO



DEPARTMENT OF ELECTRONICS AND TELECOMMUNICATIONS
Master's Degree Course in Nanotechnologies for ICTs

MODELLING OF NON-TRIVIAL SPIN TEXTURES IN MAGNETIC THIN-FILMS

Supervisor

Prof. Mariagrazia GRAZIANO

Candidate

Federica NASR (262935)



Internship Tutors

Spintec, CEA

Prof. Liliana D. BUDA-PREJBEANU

Prof. Hélène BÉA

ACADEMIC YEAR 2020 – 2021

This work is subjected to the Creative Commons Licence CC BY-NC-ND

Thesis environment

The present thesis was entirely conducted at SPINTEC, a R&D laboratory at the crossroads of nanosciences and technology, jointly operated by CEA, CNRS, University of Grenoble Alpes (UGA) and Grenoble INP. Located on the MINATEC campus in Grenoble, SPINTEC (SPINtronique et TEchnologie des Composants), founded in 2002, is one of the major international spintronics research laboratories, which aims to joint fundamental research in nanomagnetism and pioneering device technology.

The main results of this master's degree thesis, that fits into the context of the ANR project ADMIS, come from a collaborative work of [SPINTEC](#) Theory/Simulation and Magnetic Sensors groups. The ADMIS project intends to establish a regulated local, dynamic and reversible control of interfacial Dzyaloshinskii-Moriya Interaction (*i*DMI), an antisymmetric exchange interaction set up in multilayer thin-film systems and responsible of the occurrence of localized whirling magnetic textures, such as Néel magnetic skyrmions.

In detail, the headline targets of ADMIS are:

- to enhance the understanding of the physics underneath *i*DMI in Heavy Metal/Ferromagnet/Insulator (HM/FM/MOx) ultra-thin trilayers;
- to establish a local – reversible or irreversible – control of *i*DMI strength and sign, by operating a voltage gating of interfacial magnetic properties;
- to explore the impact of *i*DMI strength on the spin-driven motion of domain walls and magnetic skyrmions;
- to study and implement memory, logic and bio-inspired devices based on the electric field control of *i*DMI.

The present master's degree thesis is part of the ADMIS project. The studies carried out by micromagnetic modelling are intended to support the understanding of the *i*DMI effect in HM/FM/MOx trilayer systems.

Summary

Topological non-trivial whirling spin textures such as magnetic skyrmions have recently triggered a lot of interest by virtue of their particle-like nature, stability and tunability. All these attributes make them enticing when envisioned as elementary units of digital information to build efficient, fast, reliable, and versatile spintronic devices. Particularly, due to their nanoscale size, combined with the efficient current induced motion via Spin–Orbit Torque (SOT) [1], magnetic skyrmions are potential candidates to develop miniaturized ultra-low power, high-speed and high-density devices, implementing a Logic in-Memory (LIM) approach. Also, their peculiar solitonic nature makes them attractive in the field of neuro-morphic computing. The mingled features of stable chiral spin arrangements and Néel-type domain walls are ascribable to an antisymmetric exchange interaction called interfacial Dzyaloshinskii-Moriya Interaction (*i*DMI). This latter is set up in ultra-thin films with Perpendicular Magnetic Anisotropy (PMA), e.g. of the type Heavy Metal/Ferromagnet/Insulator (HM/FM/MOx), by the coaction of strong Spin–Orbit Coupling (SOC) in the HM and the broken inversion symmetry (SIA) – also responsible for the emergence of novel physics, such as Spin–Orbit Torque [2].

Among the possible topological quasi-particles stabilised in such peculiar trilayer systems, a lower dimension (1-D) non-trivial spin texture, named Domain Wall Skyrmion (*DWSk*), has been newly reported and experimentally observed using Lorentz Transmission Electron Microscopy (LTEM). The *DWSk* is a 1-D topological excitation sharing the same topological charge Q as conventional skyrmionic bubble ($Q = \pm 1$) and describable as a localized $2 - \pi$ rotation of the In-Plane (IP) component of magnetization within a Néel domain wall, which stands between two Out-Of-Plane (OP) magnetic domains. Such spin texture can intuitively be viewed as the counterpart of a $2 - \pi$ Vertical Bloch Line coming about in Bloch instead of Néel domain walls.

Chiral skyrmionic bubbles with localised 1-D skyrmion inside the otherwise homochiral Néel domain wall, hereinafter called Double Skyrmions (*DSk*), have been numerically predicted as a soliton solution [3]. However, the dipolar energy term, accounting for their stabilization, was not included in the analytical expression of

the total energy. The dipolar contribution was held in consideration in the work of Je (2020) [4], who numerically investigated the dynamics of the skyrmion nucleation process, still object of the study. The nucleation and annihilation of 1-D skyrmions, contributing to the modification of domain wall morphology, were to just assist the topological charge evolution in the transient time frame.

The aim of this thesis work was to pursue a systematic study for magnetic stack of the type Pt/Co(0.9 nm)/MgO, using the open source GPU-accelerated micro-magnetic simulation software MuMax3. Formerly, this sample has been intensively characterized – both experimentally and numerically – since chiral magnetic skyrmions can be there stabilised at room temperature and zero external magnetic field, owing to the large i DMI of such system [5]. Such topological solitons have been further demonstrated to reach a steady-state spin driven motion and to be nucleated and manoeuvred by external magnetic field and/or spin polarized current [6]. After a first study of usual skyrmionic bubbles, the analysis carried out during this thesis work concentrated upon a more exotic skyrmion generation process, i.e. the heating-induced writing, accomplished by an ultra-fast laser pulse inducing a localised thermal demagnetization of the material. Particularly, such experimental protocol has been proved to make it easily accessible peculiar stable states that are not attainable by conventional approaches, due to high energy barriers [7].

In the present master thesis work, it is demonstrated that, by tuning the magnetic field applied during the magnetization recovery process, an initially randomly demagnetized state can numerically converge either to the hexagonal-like skyrmion bubble lattice, consistently with experimental evidences in literature [7], or to the here named magnetic multidomain state. Notably, this latter represents a stable magnetization state where a smooth domain wall of well-defined chirality and distinct non-trivial spin textures survive concomitantly. In detail, beyond the conventional skyrmionic bubble, the magnetic outline reveals the stability of two new topological excitations, namely the domain wall skyrmion and, more importantly, the double skyrmion. Such numerical prediction portrays the double skyrmion as stable state of the magnetic stack, pushing forward the earlier observations of this novel magnetic texture as a transient metastable state. The aforesaid multidomain state was tested against both thermally induced fluctuation and granularity, which validated simulation results and ruled out the numerical artefacts.

Firstly, the static behavior of usual skyrmionic bubble was characterized. Particularly, the distinctive response to magnetic anisotropy and/or i DMI strength modification is presented in a phase diagram, which could be used to find how skyrmion stability and size would be modified via voltage gating of interfacial magnetic properties. Also, the hysteresis loop of the skyrmionic bubble regime was generated, to typify the rebound to an external magnetic field.

Secondly, the double skyrmion was cross-referenced with conventional skyrmion static and dynamic behaviour. As in the case of usual single 2-D magnetic skyrmion, any point of a unit sphere can be covered by the magnetization distribution of the 1-D skyrmion situated in the domain wall. Accordingly, the double skyrmion spin texture maps twice the possible orientations of magnetization, which translates into $Q = +2$. The double skyrmion could be the expressions of a stable state which, although energetically unfavoured with reference to conventional skyrmionic bubble, is sustained by an energy barrier mainly supported by dipolar interaction. The local magnetization twist within the Néel domain wall makes it possible to abate the volume magnetic charges by way of closure of magnetic field flux lines, in analogy to the reason underneath the nucleation of magnetic domains in a ferromagnetic material. Nonetheless, the internal structure of a 1-D skyrmion reveals the existence of a narrow region where chirality is opposite to the one favoured by i DMI energy. Representative of the 1-D skyrmion exceeding cost in terms of antisymmetric exchange energy is the characteristic bending of the domain wall, that leads to a *kink* [8]: in order to keep the IP magnetization vector perpendicular to the plane of the domain wall for the maximum possible extent, a local arching is induced to reduce at minimum the Bloch nature of the domain wall, disfavoured by the Dzyaloshinskii-Moriya Interaction.

Micromagnetic simulation results reveal the DSk strong responsivity to Zeeman field and resilience against i DMI reduction and chirality switching, with properties similar to conventional skyrmionic bubble. Particularly, the accomplishment of DSk size tuning operated by external control parameter, i.e. magnetic field, and internal material parameter, such as the i DMI strength, is numerically predicted. The static analysis is complemented with the investigation of the dynamic behavior under electrical current. Analogously to conventional skyrmionic bubble, it is shown that Current In-Plane Spin Transfer Torque (CIP-STT) and/or Spin-Orbit Torque (CIP-SOT) may displace the $Q = +2$ topological charge in a track, with a characteristic space orientation of the *kink*. However, a distinctive behavior is observed in high-current regime, where the strength of the Spin-Orbit Torque may induce the DSk conversion either into two or into one isolated $Q = +1$ charge(s), or even annihilate it. This opens perspectives to conceive high-density skyrmionic devices.

Finally, a more exotic physical phenomenon is presented: the injection of a Current Perpendicular-to-Plane (CPP) STT in a magnetic tunnel junction (MTJ), with the magnetic stack conceived as *free layer* and the *reference layer* perpendicularly polarized, could nucleate double skyrmions and further induce their auto-oscillation. Specifically, it consists in the DSk spinning motion driven by the confined *kink*, where the 2-D rotation direction (clockwise or anticlockwise) is controlled by the specificity of 1-D skyrmion, either Head-To-Head (H2H) or Tail-To-Tail (T2T).

Contents

1	Introduction	11
1.1	The end of Moore’s law	12
1.2	Spintronics	15
1.3	Micromagnetic concepts	19
1.3.1	Gibbs free energy terms	19
1.3.2	Phenomena due to Spin–Orbit Coupling	23
1.3.3	Landau–Lifshitz–Gilbert–Slonczewski equation	32
1.4	Micromagnetic solver	36
1.5	Magnetic skyrmions	39
1.5.1	Characteristic quantities and topology	39
1.5.2	Skyrmion motion under current	41
1.6	Overview and objectives of the thesis	44
2	Micromagnetic simulations	47
2.1	The magnetic skyrmionic bubble	49
2.2	The skyrmion bubble lattice	58
2.3	The magnetic double skyrmion	62
2.3.1	Introduction and state of the art	62
2.3.2	Numerical characterization results	67
2.4	Other non-trivial spin textures	82
3	Conclusions & perspectives	85
	Bibliography	89

Glossary

ACW	Anticlockwise
BM	Beyond Moore
CIP	Current In-Plane
CMOS	Complementary Metal-Oxide Semiconductor
CPP	Current Perpendicular-to-Plane
CPU	Central Processing Unit
CW	Clockwise
DL	Damping-Like
DMI	Dzyaloshinskii-Moriya Interaction
DRAM	Dynamic Random Access Memory
Dsk	Double Skyrmion
DW	Domain Wall
DWRC	Domain Wall Racetrack Memory
DWsk	Domain Wall Skyrmion
EUV	Extreme Ultraviolet
FET	Field Effect Transistor
FL	Field-Like
FM	Ferromagnet(ic)
FSAL	First-Same-As-Last
GAA	Gate All Around
GAAFET	Gate All Around Field Effect Transistor
GMR	Giant Magnetoresistance
HDD	Hard Disk Drive
HM	Heavy Metal
H2H	Head-To-Head
IC	Integrated Circuit
<i>i</i> DMI	interfacial Dzyaloshinskii-Moriya Interaction
IP	In-Plane
IRDS	International Roadmap for Devices and Systems
LH	Left-Handed

LL	Landau-Lifshitz
LLG	Landau-Lifshitz-Gilbert
LLGS	Landau-Lifshitz-Gilbert-Slonczewski
LTEM	Lorentz Transmission Electron Microscopy
MCA	Magnetocrystalline Anisotropy
MD	Magnetic Domain
MM	More Moore
MOSFET	Metal Oxide Semiconductor Field Effect Transistor
MRAM	Magnetoresistive Random Access Memory
MTJ	Magnetic Tunnel Junction
MtM	More than Moore
OOMMF	Object Oriented Micro Magnetic Framework
OP	Out-Of-Plane
OV	Operating Voltage
PBC	Periodic Boundary Condition
PEEM	Photoemission Electron Microscopy
PMA	Perpendicular Magnetic Anisotropy
RAM	Random Access Memory
RDF	Random Dopant Fluctuation
REE	Rashba-Eldestein Effect
RH	Right-Handed
RK	Runge-Kutta
R&D	Research & Development
SAF	Synthetic Antiferromagnet
SCE	Short Channel Effect
SEM	Scanning Electron Microscopy
SHA	Spin Hall Angle
SHE	Spin Hall Effect
SIA	Structural Inversion Asymmetry
SkHE	Skyrmion Hall Effect
SOC	Spin Orbit Coupling
SOT	Spin Orbit Torque
SRAM	Static Random Access Memory
STT	Spin Transfer Torque
TMR	Tunnel Magnetoresistance
T2T	Tail-To-Tail
ULSI	Ultra Large Scale Integration
VBL	Vertical Bloch Line
VCMA	Voltage Controlled Magnetic Anisotropy
VLSI	Very Large Scale Integration
XMCD	X-ray Magnetic Circular Dichroism

Chapter 1

Introduction

Since its beginning, Si-based complementary metal-oxide semiconductor (CMOS) devices have been dominating over the field of microelectronics, in terms of density of integration and cost: as of 2011, 99% of integrated circuit (IC) chips, including most digital, analog and mixed-signal IC, are fabricated using CMOS technology [9]. The field of spintronics, or spin electronics, is nowadays emerging as one up-and-coming field for next-generation nanoelectronics [10]. Here, the digital encoding of information is performed by combining the advantages of manipulating both the spin and the electrical charge, the two fundamental properties of an electron. The electrical and magnetic phenomena are thus intermingled: this creates new technological scenarios that look promising because of a lower power consumption, higher speed and increased integration density with respect to conventional microelectronic devices. Indeed, the energy required to switch a spin state is much less than the energy budget required to control an electrical current [11]. Furthermore, the exploitation of the magnetic order is expected to incorporate novel functionalities, e.g. non-volatility, unapproachable through conventional CMOS technology and beneficial to lower stand-by power consumption during the digital signal processing and propagation.

The purpose of the next section, wholly addressed to the field of conventional CMOS micro/nanoelectronics, is that of outlining the semiconductor industry status and pointing out the main technology bottlenecks and side effects faced in the transistor scaling. To follow, a broad overview in the state of the art of spintronics, new branch of electronics, will be profiled. Here, vanguard alternative solutions have been emerging over the years, highly functional for transcending some of conventional electronics limitations and rendering novel ideas to complement CMOS devices. Right after, it will be provided an insight into the basic concepts of micromagnetism, representing the theoretical background essential for the comprehension of spintronics phenomena, followed by a review of MuMax3, the micromagnetic solver used in the course of this thesis work.

1.1 The end of Moore’s law

The Moore’s law is an empirical observation originated in 1965s, founded upon the experimental evidences concerning the evolution of the Silicon microelectronics: it has been representing the Golden Rule of the microelectronic industry over the last decades. In the original draft, Gordon E. Moore foresaw that the number of integrated components per IC would have doubled every two years. On the outlook of semiconductor industry, to be compliant with the Moore’s law has resulted in an exponential increase in terms of performances with an exponential decrease in terms of cost for a given performance, bringing our society into the information era.

To refer to a peculiar semiconductor manufacturing process, coupled with its specific design rules, the expression technological node is employed: the lower the node, the more advanced the circuit generations and architectures, leading to smaller feature sizes, producing even more miniaturized transistors which are increasingly powerful and efficient in terms of energy dissipation.

Historically, gate length and metal half-pitch were roughly interchangeable quantities: they were equivalent to the node number. However, most recently, specifically since the mid-1990s, a discrepancy between nomenclature and physical counterpart has been developing and, to stay on the Moore’s law track, chip makers shrank the gate length more roughly than other features of the devices: as a matter of fact, the gate length became lower than the technological node. Nevertheless, since 2000s device Design & Implementation took a different route to face limitations of power dissipation (Joule’s heating) and current leakage, ascribed to the billions of transistors packed into one chip, as well as to quantum mechanical behavior of electrons at atomic scale, with the associated quantum tunneling effect impacting the device reliability and worsening the thermal issues. As a result, technological manoeuvres have been adopted to keep updating performances with just a soft shrinkage of gate length [12]. This trend is well shown in Figure 1.1.

Currently, the 7-nm node era (about 100 million of transistors in a square centimeter of Si) is running its course; 5-nm node Central Processing Units (CPU) are being manufactured right now and leading corporations expect to be projected on what might be called the 1-nm node (scarcely the width of 5 Si atoms) within a decade [12].

The idea behind Very Large Scale Integration (VLSI) and Ultra Large Scale Integration (ULSI), the latter integrating or embedding hundreds of billion of transistors per chip, is geometric scaling. Indeed, a high miniaturization level offers several advantages, as an improved integration density, together with upgraded circuit complexity.

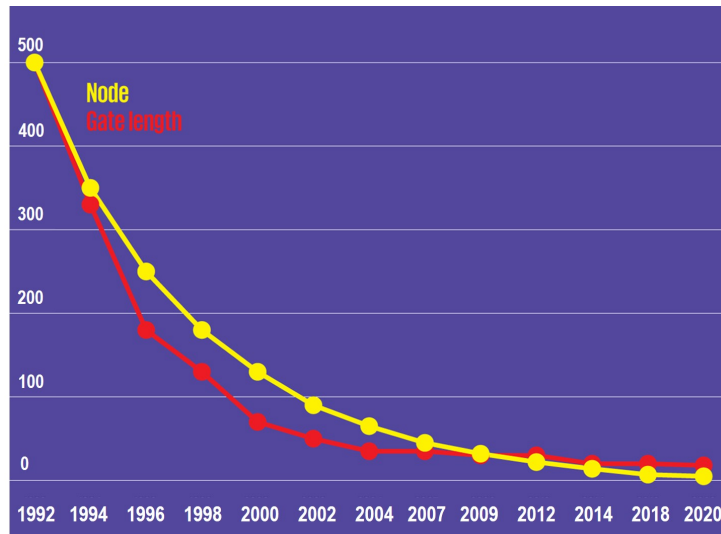


Figure 1.1: SOURCE – Stanford Nanoelectronics Lab, Wikichip, IEEE IRDS 2020.

However, starting from 2000s, the technology node tables entered the nm scale area, where devices are essentially mesoscopic. This has posed serious technological challenges because of non-ideality effects, ascribed to gate length miniaturization, e.g. Short Channel Effects (SCE), ballistic transport [13], quantum effects and technological uncertainty, like Random Dopant Fluctuations (RDF) [14]. As a matter of fact, geometrical (planar) scaling is at an end due to rocketing fabrication cost, technology barriers like extreme ultraviolet (EUV) lithography, power density limits and electrical leakage, diverting R&D labs towards the route of new chip-manufacturing processes and novel technological frontiers.

The International Roadmap for Devices and Systems (IRDS) 2020 entitled *More Moore* states: “System scaling enabled by Moore’s scaling is increasingly challenged by the scarcity of resources such as power and interconnect bandwidth”. This means that it will no longer be favourable from an economical perspective for high-tech industries to keep on facing traditional metal-oxide semiconductor field effect transistors (MOSFET) miniaturization. The scaling scenario for device architectures locates the end of FinFET technology at 2025. Most remarkable cutting-edge tendencies are More Moore (MM), focused on monolithic 3D integration of Gate All Around (GAA) & 3D VLSI [15], More than Moore (MtM), centred on diversification and integration of multiple functions and, last but not least, Beyond Moore (BM), oriented to innovative architectures. Figure 1.2 provides a sketch of Gate All Around (GAA) FET and reports the trend of the Operating Voltage (OV) with the advancement of semiconductor technology.

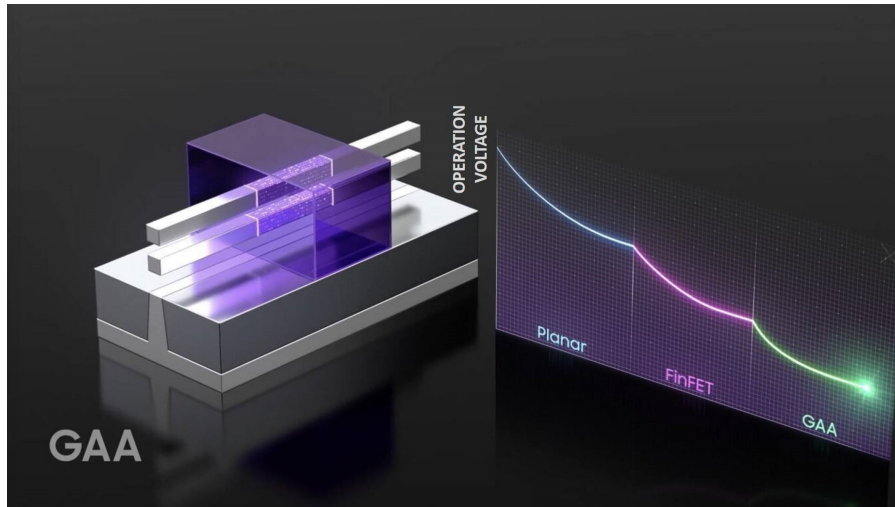


Figure 1.2: Left – Sketch of Gate All Around Field Effect Transistor (GAAFET).
 Right – Qualitative behavior of Operation Voltage vs. semiconductor tech.
 SOURCE: SamsungSemiUS, Youtube.

And it is exactly among the possible purposeful avenues comprised in the framework of Beyond Moore (BM), that the idea of spintronics develops. As already anticipated, spintronics adds a new degree of freedom on which information may be coded. As a matter of fact, data storage has been using magnetism for long time: what is new with spintronics is the coupling between spin and electrical charge. If technologically implemented, this concept may lead to non-volatile and ultra-fast coding of information, e.g. the Magnetoresistive Random Access Memories, (MRAM), beneficial not only for long-time scale storage, but also for faster and shorter-time scale storage, essential for memories close to the processor. One advantage of non-volatility for memories close to the processor is the drastic reduction of stand-by power consumption. Indeed, for standard Solid State Random Access Memories (SRAMs or DRAMs), by decreasing the technological node, the stand-by power, necessary to refresh the info (not to lose it), is becoming even more important if compared to the power consumption of writing or reading operations. This is why spintronics is a very interesting alternative.

The next section will be entirely dedicated to the description of the main steps forward in the field of spintronics, emphasizing the principal limitations of different technologies, to end up with the so-called Skyrmion Racetrack Memory, dealing with the nucleation and manipulation of magnetic skyrmions, which represent the main topic of this thesis.

1.2 Spintronics

A major breakthrough in the field of spintronics was achieved with the discovery of Tunnel Magneto Resistance (TMR), occurring in a Magnetic Tunnel Junction (MTJ), mainly composed by an ultra-thin insulating layer (typically 1 nm) in between two ferromagnets. The TMR led to a considerable amplification in the magnetoresistance effect (more than one order of magnitude), if compared to the earlier Giant Magneto Resistance (GMR), featured by a metallic layer as spacer, directly implying a reduction in the reading power consumption of Hard Disk Drives (HDD) [16].

Basically, the magnetoresistance effect consists on the dependence of the electrical resistance (low/high), on the relative magnetization state (parallel/anti-parallel) of the two ferromagnetic (FM) layers: in reference to the purely quantum mechanical TMR, electrons are more inclined to tunnel through the insulating film in case of parallel orientation than in opposite case. The binary resistance state of the MTJ bears on the concept of the non-volatile Magnetoresistive Random Access Memory (MRAM), where the bottom ferromagnetic layer represents the *fixed layer* or *reference layer*, with magnetization pinned by a Synthetic Antiferromagnet (SAF), while the top one is the *free layer* or *storage layer*, with switchable magnetization orientation. Such an implementation makes it possible to link the two states of electrical resistance (high/low) to the digital encoding of information (0/1 bits).

Each memory cell needs to be read and written: actually the TMR effect is employed just as the simplest approach to implement the reading procedure, while nowadays the writing procedure is mainly accomplished by Spin Transfer Torque (STT). More in detail, a charge current, spin polarized by the thick *fixed layer*, is injected to induce a torque on magnetization of the thinner *free layer* via intrinsic angular momentum (spin) transfer, resulting from the misalignment of the electron moment and the local magnetization, to which electrons have to adapt to, while perturbing it at the same time. Indeed, in analogy to electric current induced by moving charges, in presence of an imbalance between flowing up and down electron spins, spin motion generates a spin current which carries spin angular moment. This, in turn, can be transferred to the material magnetization through a strong and local interaction represented by the torque, as a result of the angular moment conservation law [17]. The STT mechanism is schematically depicted in Figure 1.3. This approach, a major discovery in condensed matter and material physics, was essential for the technological development of high-performance and high-density STT-MRAM, overcoming the classical design (toggle-MRAM), challenging both in terms of power consumption and scaling of dimensions, where a local magnetic field (Oersted field), generated by currents flowing in the so called Bit and Write Word lines, was used to switch the magnetization of the *free layer*.

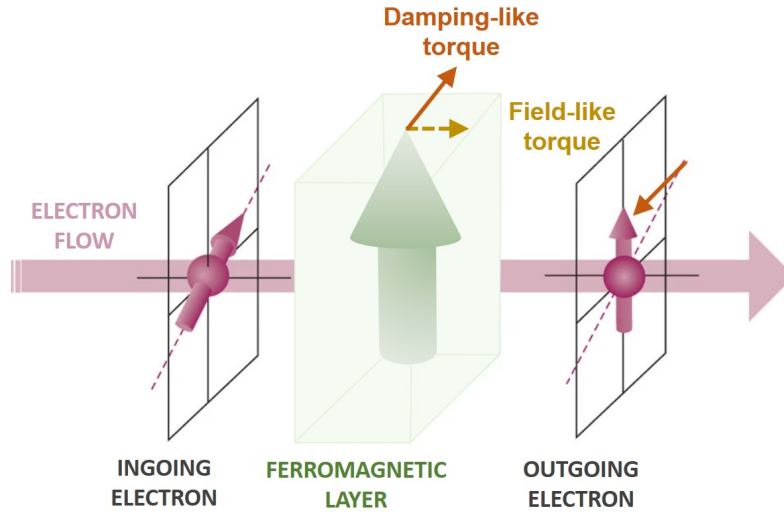


Figure 1.3: Illustration of current-induced STT.

Further improvements in terms of energy efficiency of the writing procedure, write endurance and speed can be gained in magnetization switching through Spin-Orbit Torque (SOT) [18]. This is still the subject of study, that is of great recent interests due to its potential applications in SOT-MRAM, in which the read and write paths are disentangled, as opposed to STT-MRAM, thereby decreasing the read error rate [19]. An SOT-MRAM cell integrates a magnetic tunnel junction (MTJ) on top of a heavy-metal (HM) layer, the latter characterized by strong Spin-Orbit Coupling (SOC). During the writing stage of such system, featured by broken structural inversion symmetry, an in-plane (IP) charge current is injected into the HM layer and, as a result of the Spin Hall effect (SHE), a perpendicular spin current is generated, inducing a spin accumulation HM/FM interface, exerting a torque in the overlying FM layer that can switch its magnetization [18]. Figure 1.4 provides a comparison between STT-MRAM and SOT-MRAM schematics. Compared to conventional Random Access Memories (RAM) based on semiconductor technology, beyond being non-volatile, Magnetoresistive Random Access Memories (MRAM) can operate at higher temperatures, they are radiation resistant and less energy-consuming. However, notwithstanding its several benefits, MRAM technologists are still facing the relatively low storage density [16].

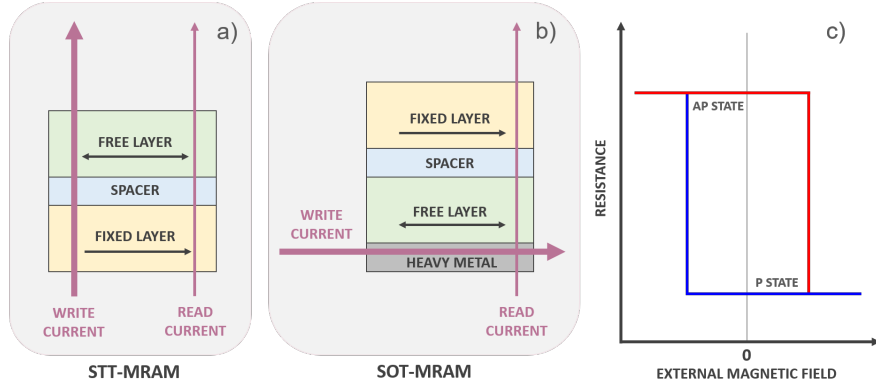


Figure 1.4: Schematics of a) STT-MRAM and b) SOT-MRAM. c) Qualitative resistance hysteresis loop with two stable states at $\mu_0 H_{app} = 0$ mT.

An alternative approach to conventional Random Access Memories (RAM) and Magnetic Hard Disk Drives (HDD) is the so called Magnetic Domain Wall Race-track Memory (DWRM), originally proposed by Stuart Parkin [20]. It may offer the cheapness of HDD but the high performance and reliability of RAM. Also, the truly 3-D architecture is extremely advantageous for the improvement of the integration density. Practically, the vertically configured racetrack, maximizing the storage density, consists on a U-shaped ferromagnetic (FM) nanowire, arranged perpendicularly on the surface of a silicon wafer. Here, the directions of magnetization vectors within magnetic domains (MD) are representative of the binary information, i.e. the spacing between consecutive domain walls (DW), that is the bit length, is the information carrier. “RM is fundamentally a shift register in which the data bits are moved to and fro along any given racetrack to intersect with individual reading and writing elements integrated with each racetrack” [20]. However, there exist challenging facets of DWRM affecting its ultimate performance, as the reproducibility of DW motion, the pinning by the edges and the required high current density [16].

This is exactly where purposeful ideas of operating and manipulating magnetic spin textures, like magnetic skyrmions, enter the game of spintronics. In particular, the circular symmetry of bubble magnetic domains fulfills the idea of avoiding edge effects, while the homochirality is an essential element to displace them as single particles (soliton nature). The energy contribution stabilizing chiral magnetic skyrmions comes from the so called Dzyaloshinskii-Moriya Interaction (DMI), brought out from the combination of strong Spin-Orbit Coupling (SOT) and structural inversion asymmetry (SIA). The DMI, discussed more in detail in Section 1.3.2, is an antisymmetric exchange interaction that leads to a canting of neighboring spins, thus imposing a chiral configuration of the DW.

Magnetic skyrmions can be defined as magnetic spin textures with non-trivial topology, typified by an unambiguous chirality, determined by the sign of DMI. They can hence be depicted as tiny circular magnetic domains encircled by a homochiral domain wall, configured either in clockwise (right-handed) or anticlockwise (left-handed) rotation of magnetization, when crossing the skyrmion radially from left to right, as Figure 1.5 a) illustrates.

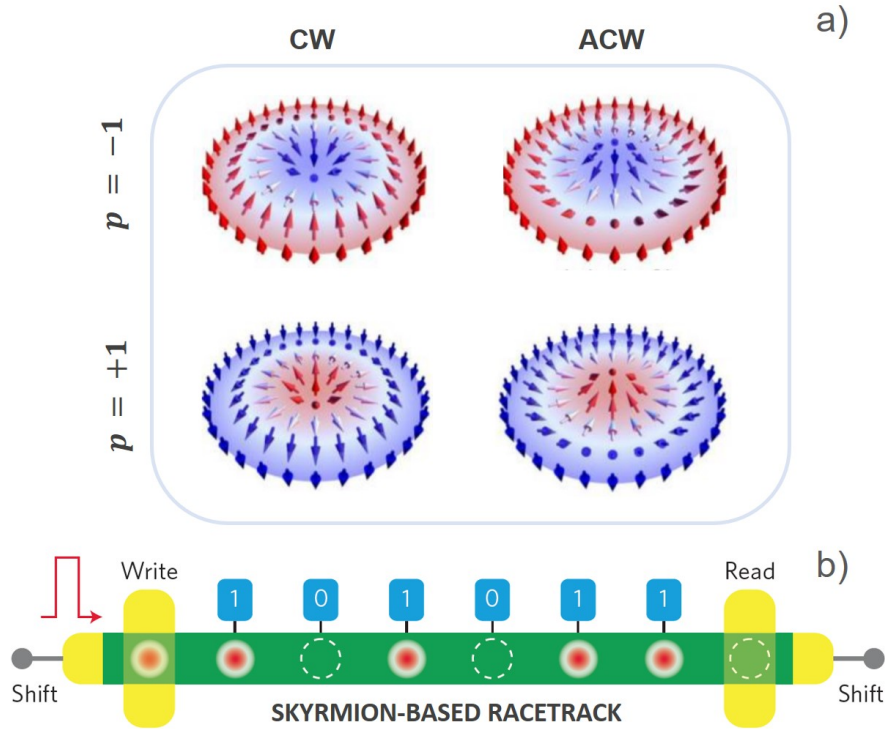


Figure 1.5: a) Illustration of CW and ACW Néel skyrmions [21].

The polarity p indicates the skyrmion core magnetization.

b) Potential realization of a skyrmion-based racetrack [22].

Their potential nanoscale dimension, solitonic nature, high stability and tunability, conjugated with extremely low driving current density (lower than that required for DW motion) [23] [24] [25] and efficient current-induced manipulation by SOT [26] render skyrmions considerably attractive as elementary units for upcoming spintronic devices and systems. An example of skyrmion-based device is the so-called Skyrmion Racetrack Memory of Figure 1.5 b), where the digital information is encoded in the presence (logic 1) or absence (logic 0) of the magnetic skyrmion.

Magnetic skyrmions thus represent the main candidates to get the better over magnetic HDD as regards integration density as well as to overcome the issues related to the control of domain wall motion, i.e. reliability and requested high current densities in Domain Wall Racetrack Memories. More details on magnetic skyrmions will be given in Section 1.5.

On the following, the basics of micromagnetic theory will be provided, with the objective of facilitating the understanding of the micromagnetic simulation outcomes focused on non-trivial spin textures, including magnetic skyrmions, obtained during this thesis work and presented in Chapter 2.

1.3 Micromagnetic concepts

Micromagnetism is the theory upon which the description of the magnetization in a magnetic material relies. In this framework, the magnetization distribution is delineated under the definition of the unit vector $\mathbf{m}(\mathbf{r}, t) = \mathbf{M}(\mathbf{r}, t)/M_s$, on the basis of two fundamental assumptions:

- the inspected length scales are large enough for the discrete nature of the matter, that is the atomic structure, to be ignored (continuum approximation);
- in presence of an homogeneous material, the magnetization vector is uniform in modulus, which matches the saturation magnetization M_s .

The continuum theory of micromagnetism allows to predict the magnetization distribution of a ferromagnet as well as the dynamics between two stable states.

1.3.1 Gibbs free energy terms

The objective of static micromagnetics is to determine the spatial distribution of magnetization \mathbf{M} at equilibrium. Under the assumption of uniform $|\mathbf{M}| = M_s$, this problem is reduced to finding the magnetization direction vector or unit vector \mathbf{m} , by minimizing the total magnetic energy:

$$\mathcal{E} = \mathcal{E}_Z + \mathcal{E}_{ex} + \mathcal{E}_{mc} + \mathcal{E}_d + \mathcal{E}_{add} \quad (1.1)$$

where \mathcal{E}_Z is the Zeeman energy due to an external magnetic field or Zeeman field, whereas the terms \mathcal{E}_{ex} , \mathcal{E}_{mc} and \mathcal{E}_d account for the exchange, the magnetocrystalline anisotropy and the dipolar energy contributions, respectively. Last but not least, \mathcal{E}_{add} includes additional terms that will be uncovered later on.

Zeeman energy

Zeeman energy, also called external magnetic field energy, is the potential energy of a magnetic moment or that of a magnetic body as a whole in an external magnetic field. Its volume density is expressed as:

$$E_Z = -\mu_0 \mathbf{M} \cdot \mathbf{H}_0 \quad (1.2)$$

where $\mu_0 = 4\pi \times 10^{-7}$ H/m is the vacuum permeability.

Upon this, the total Zeeman energy can be computed by integrating over the volume of the ferromagnet \mathcal{V} :

$$\mathcal{E}_Z = -\mu_0 \int_{\mathcal{V}} \mathbf{M} \cdot \mathbf{H}_0 d\mathcal{V} \quad (1.3)$$

As shown, the Zeeman energy is minimized when the magnetization \mathbf{M} is aligned along the applied field \mathbf{H}_0 .

Exchange energy

Heisenberg symmetric exchange energy arises from a local purely quantum mechanical effect related to the indistinguishability of quantum point-like particles as electrons and it is at the basis of ferromagnetism, which is essentially originated from a phenomenon electrical in nature. The exchange energy can be interpreted as a quantum correction to the classical Coulomb's repulsion and it is often called Pauli's repulsion, with regard to the Pauli's exclusion principle that applies to identical fermions. Practically, it is energetically favourable for an atom with partially filled outer shell to have the unpaired valence electrons farther apart from each other, condition that is verified in case of parallel spin, i.e. symmetric spin states and antisymmetric spatial states. The coupling of two neighboring atoms with unpaired electrons depends instead on the way orbitals are hybridized and the number of electrons they host. The exchange energy between two neighboring atomic spins S_i and S_j can be expressed as:

$$\mathcal{E}_{ij} = -J_{ij} \mathbf{S}_i \cdot \mathbf{S}_j \quad (1.4)$$

where J_{ij} is the Heisenberg exchange constant, that is positive (respectively negative) in case of ferromagnets (respectively antiferromagnets), thus favouring a parallel (respectively anti-parallel) spin alignment.

The line between the discrete exchange and the continuous theory is established by expanding the energy in case of a 1-D chain of classical spins, under the assumption of small differential angle $\delta\theta$ between neighboring atom spins:

$$\mathcal{E}_{ij} = -JS^2 \cos(\delta\theta) \sim -JS^2 \left[1 - \frac{(\delta\theta)^2}{2} \right]$$

Summing up all over the atoms in the crystal and normalizing the total energy with lattice parameter cubed a^3 , the volumetric exchange energy density is finally expressed as:

$$E_{ex} = const + \frac{nJS^2}{2a} \left(\frac{d\theta}{dx} \right)^2 \quad (1.5)$$

where n is the number of first neighbors, called coordination number, equal to $n = 2$ in the one dimensional case.

By generalizing the previous equation, it is possible to define the exchange energy density for a 3-D system:

$$E_{ex} = A \sum_i \sum_j \left(\frac{\partial m_i}{\partial x_j} \right)^2 = A (\nabla \mathbf{m})^2 \quad (1.6)$$

where the constant term *const*, related to the symmetry and coordination number, has been neglected. In the latter expression, the exchange stiffness $A \sim nJS^2/(2a)$ appears, which is measured in J/m.

Magnetostatic energy

Magnetostatic energy, also called dipolar energy, is originated from the mutual long-range interaction involving all moments of a magnetic body, which perturb each other through the so called magnetostatic field, viewable as an internal Zeeman-like field. A distinction is usually made between the part of the dipolar field occurring inside the magnetic body, called demagnetizing field, and that outside the body, called stray field. The dipolar energy density may be written:

$$E_d = -\frac{1}{2} \mu_0 \mathbf{M} \cdot \mathbf{H}_d \quad (1.7)$$

where \mathbf{H}_d is the dipolar field and the (1/2) prefactor is introduced to count just once the reciprocal energy for each pair of elementary dipoles.

In most cases, to simplify the computational procedure of the total dipolar energy, it is possible to introduce the magnetic volume charges, by analogy with the differential formulation of Gauss' law for electrostatics ($\nabla \cdot \mathbf{E} = \rho/\epsilon_0$):

$$\nabla \cdot \mathbf{H}_d = -\nabla \cdot \mathbf{M} = \rho \quad (1.8)$$

where $\mathbf{M}(\mathbf{r})$ is the magnetization distribution in the magnetic body.

By considering that \mathbf{H}_d has zero curl (similarly to electrostatics) and that thus derives from a potential, $\mathbf{H}_d = \nabla\phi_d$, the total magnetostatic energy may be expressed as:

$$\mathcal{E}_d = -\frac{\mu_0}{2} \int_{\mathcal{V}} \mathbf{M} \cdot \mathbf{H}_d d\mathcal{V} = \left(\int_{\mathcal{V}} \rho \phi_d d\mathcal{V} + \int_{\mathcal{S}} \sigma \phi_d d\mathcal{S} \right) \quad (1.9)$$

where the concept of magnetic surface charges, $\sigma = \mathbf{M} \cdot \hat{\mathbf{n}}$, were introduced to account for abrupt change of magnetization when crossing the sample surface, $\hat{\mathbf{n}}$ being the normal vector to the surface of the magnetic body, pointing outwards.

The effect of magnetostatic energy is clearly that of reducing at minimum the surface and volume charges within the magnetic body. In case of uniformly magnetized system, the first term cancels and the magnetization tends to align in the direction minimizing surface charges, i.e. along long dimensions of the sample. Being this energy contribution substantially driven by the shape of the system, it is also called shape anisotropy: for example, in case of an ellipsoid, magnetization tends to align along the long axis, where opposite surface charges can be further apart from each other.

Under the assumption of uniform magnetization, it is possible to express analytically the average value of the dipolar field inside the system along the main or major axes i :

$$\langle \mathcal{H}_{d,i} \rangle = -N_i \mathbf{M} \quad (1.10)$$

where N_i are the demagnetizing factors or coefficients, either null or positive, i running over all three main directions and $N_x + N_y + N_z = 1$. They prove a measure of the average demagnetizing field, so called for opposing the magnetization, for the considered axis.

Accordingly, the density of demagnetizing energy may be written as:

$$E_d = -(\mu_0/2) \langle \mathbf{H}_d \rangle \cdot \mathbf{M} = m_i^2 N_i K_d \quad (1.11)$$

where m_i is the reduced magnetization along a defined direction and K_d is the so called dipolar constant, $K_d = \frac{1}{2} \mu_0 M_s^2$, given in J/m³.

Commonly, the demagnetization coefficients are employed to assess the energy difference along different directions. In case of a thin film or slab, under the assumption $L_x, L_y \gg L_z$, $N^{\parallel} = 0$ (parallel to the film plane) and $N^{\perp} = 1$ (perpendicular to the film plane). As a result, dipolar energy density can be defined as:

$$E_d = (N^{\parallel} \sin^2 \theta + N^{\perp} \cos^2 \theta) K_d \sim (N^{\parallel} - N^{\perp}) K_d \sin^2 \theta = -K_d \sin^2 \theta \quad (1.12)$$

where $m^{\parallel} = \sin \theta$, θ being the angle between the magnetization and the perpendicular axis.

Here, the relation $\cos^2 \theta = 1 - \sin^2 \theta$ was used and the resulting constant term $N^\perp K_d$ neglected as only energy differences are relevant.

Different is the case of soft magnetic materials, where the magnetization tends to remain parallel to the edges and surfaces of the system: in this way, surface charges are minimized but this tendency makes volume charges arising as the magnetization is no more uniform.

1.3.2 Phenomena due to Spin–Orbit Coupling

Spin-Orbit Coupling (SOC) is a relativistic effect defined as the interaction of orbital magnetic moment $\boldsymbol{\mu}_\ell$, associated with electron’s orbital motion around the nucleus, and intrinsic magnetic moment $\boldsymbol{\mu}_s$, originated by electron’s spin.

In the lab frame, electron has a position $+\mathbf{r}$ and a velocity $+\mathbf{v}$. In its rest frame, the electron perceives the nucleus of charge $+e$ and position $-\mathbf{r}$ moving with a velocity $-\mathbf{v}$. The electromagnetic force, or Lorentz force, acting on a particle of charge q moving with a velocity \mathbf{v} in an electric field \mathbf{E} and magnetic field \mathbf{B} is:

$$\mathbf{F} = q \mathbf{E} + q \mathbf{v} \times \mathbf{B} \quad (1.13)$$

Considering the case of zero external magnetic field, the electron experiences a time-varying electric field \mathbf{E} generated by the moving nucleus:

$$\mathbf{E}(t) = \frac{e}{r^2} \hat{\mathbf{r}}(t) = \frac{e}{r^3} \mathbf{r}(t) \quad (1.14)$$

A charged particle, immersed in a time-varying electric field, senses the latter in the form of an effective magnetic field. This is exactly the magnetic field generated by a moving charge:

$$\mathbf{B} = -\frac{1}{c^2} \mathbf{v} \times \mathbf{E} \quad (1.15)$$

Recalling the definition of linear momentum $\mathbf{p} = m\mathbf{v}$ and expressing the electric field explicitly, one obtains:

$$\mathbf{B} = \frac{e}{m_e c^2 r^3} \mathbf{r} \times \mathbf{p} = \frac{e}{m_e c^2 r^3} \boldsymbol{\ell} \quad (1.16)$$

where $\boldsymbol{\ell}$ is the orbital angular momentum.

This leads to a Zeeman-like interaction between the electron magnetic moment – that becomes a question of intrinsic magnetic moment being the electron at rest in its frame of reference – and the effective magnetic field generated by the nucleus:

$$H_{SO} = -\boldsymbol{\mu}_s \cdot \mathbf{B} = \lambda \boldsymbol{\ell} \cdot \mathbf{s} \quad (1.17)$$

Here, $\lambda = e^2/(2m_e^2 c^3 r^3)$ and $\boldsymbol{\mu}_s$ is defined as

$$\boldsymbol{\mu}_s = -\frac{e}{m_e c} \mathbf{s} \quad (1.18)$$

where the term $(1/2)$ in λ is a corrective factor whose physical explanation can be found quantum mechanically and \mathbf{s} is the intrinsic angular momentum.

An equivalent formulation for the coefficient λ can be found by expressing the electric field as the gradient of the electrostatic potential $\mathbf{E} = -\nabla(V)$ that, in the central field approximation, returns:

$$H_{SO} = -\frac{e}{2m_e^2 c^3 r} \frac{dV}{dr} \boldsymbol{\ell} \cdot \mathbf{s} \quad (1.19)$$

where the operator $\mathbf{s} = \hbar/2 \hat{\sigma}$ with $\hat{\sigma}$ Pauli's matrices.

In the new basis, where the SOC perturbed Hamiltonian is diagonal, it is requested to define a new complete set of mutually commuting operators, that are: $\boldsymbol{\ell}^2$, \mathbf{s}^2 , \mathbf{j}^2 , \mathbf{j}_z , where $\mathbf{j} = \boldsymbol{\ell} + \mathbf{s}$ is the total angular momentum operator. The net effect is that of removing the degeneration of orbitals, previously energetically equivalent, through a supplementary energy term which is directly proportional to Z^4 , with Z the atomic number. This reveals that the SOC is strong just in case of heavy elements, where the effective magnetic field generated by the nucleus is relevant. As a matter of fact, for $3d$ transition metals, like Fe, Co and Ni, the crystalline field plays a major role, generating a strong perturbation, which depends on the characteristics and symmetries of crystal lattice, that makes the SOC negligible. As a result, the magnetic moment of atoms/ions in the crystal is essentially produced by the intrinsic angular momentum and the orbital component the angular momentum is said to be quenched.

There are plenty of phenomena originated by the Spin-Orbit Coupling, that can be considered the gist of spintronics. The SOC, by coupling the electron's spin with the orbital angular momentum, which in its turn depends on the crystal lattice, generates Magnetocrystalline Anisotropy (MCA) in bulk ferromagnet which leads to preferential alignment of magnetization along certain crystallographic directions, called *easy axes*, energetically favoured with respect to *hard axes*. In other words, the variation of spin orientation induces a modification in the overlapping degree of the magnetic electron wavefunctions, thus defining easy directions, which are energetically convenient. In the framework of ferromagnetic thin-film systems, with broken inversion symmetry at the interfaces, the SOC is at the origin of an interfacial magnetic anisotropy K_s , energetically favouring Out-Of-Plane (OP) magnetization and essential for the nucleation of magnetic skyrmions.

The combined effect of inversion asymmetry (SIA) and strong SOC, e.g. introduced by interfacing the ferromagnetic thin-film with an heavy-metal layer, leads to the antisymmetric exchange interaction called Dzyaloshinskii-Moriya Interaction (DMI) [27] [28].

Magnetocrystalline anisotropy energy

Magnetocrystalline anisotropy is a special case of magnetic anisotropy and one of the sources of coercivity. The joining of crystal field effect (electron orbital – crystal lattice coupling) and the relativistic spin-orbit effect (electron orbital – electron spin coupling) causes ferromagnetic materials to have magnetocrystalline anisotropy, energetically favouring the alignment of the magnetization vector \mathbf{M} along certain crystallographic directions or planes of the solid, called *easy axes* or *planes*. These are usually related to the principal axes of the crystal lattice, in opposition to the so called *hard axes* or *planes*.

In general, the magnetocrystalline anisotropy energy density may be expressed in relation to a dimensionless function f , the basis of which could be whatever set of angular functions consistent with the symmetry of the crystal lattice, e.g. the atomic physics orbital functions $Y_{l,m}$:

$$E_{mc} = K f(\theta, \phi) \quad (1.20)$$

For the sake of simplicity, the best choice for the basis falls upon trigonometric functions, where odd terms must be ignored in compliance with time reversal symmetry ($\mathbf{M} \equiv -\mathbf{M} \Rightarrow f(\mathbf{M}) \equiv f(-\mathbf{M})$), meaning that, once fixed the angle in between the magnetization axis and the *easy axis*, the energy is the same regardless of the orientation of magnetization along that axis. For cubic crystal systems like Fe and Ni, naturally featured by three and four *easy axes*, respectively, the magnetocrystalline anisotropy energy density is expressed as:

$$E_{mc, cub} = K_{1c} s + K_{2c} p + K_{3c} p^2 + \dots \quad (1.21)$$

with $s = \alpha_1^2 \alpha_2^2 + \alpha_2^2 \alpha_3^2 + \alpha_3^2 \alpha_1^2$ and $p = \alpha_1^2 \alpha_2^2 \alpha_3^2$, α_i being the director cosines of magnetization along the three cartesian axes.

In the event of hexagonal (e.g. Co) or tetragonal symmetries, the azimuthal dependence of the energy, that is the third order term, accounts for the orientation of the magnetization projection along the polygon basal plane, where the two extreme cases, magnetization crossing either one edge or one side of that polygon, are not energetically equivalent. And that is exactly the first energy term which allows us to discriminate between the two aforementioned symmetries.

However, just the first and second order terms are not negligible, and this leads to an equivalent expression of the magnetocrystalline anisotropy energy density both for hexagonal and tetragonal systems:

$$E_{mc,hex} = K_1 \sin^2 \theta + K_2 \sin^4 \theta + \dots \quad (1.22)$$

where θ is the (polar) angle between \mathbf{M} and the high symmetry axis. Often, just the first order term is considered and the above expression simplifies:

$$E_{mc} = K_u \sin^2 \theta \quad (1.23)$$

Accordingly, the relevance of anisotropy can be assessed in terms of K_u , that is the uniaxial anisotropy constant expressed in J/m^3 or, equivalently, in field units under the definition of an anisotropy field, $H_a = 2K_u/(\mu_0 M_s)$. Magnetic materials with low (high) coercivity and remanence, the amplitude of which is partly dictated by the strength of anisotropy, are called soft (hard) magnetic materials.

At this point of the treatment, there are all the ingredients to define the characteristic length scales, that play a central role in the delineation of the minimum size below which specific phenomena can be observed, dealing with the magnetism at the nanoscale:

- anisotropy exchange length or Bloch parameter, $\Delta_u = \sqrt{A/K_u}$, direct measure of the domain wall width, resulting from the competing effect of exchange energy, which favours an infinite extension of the domain wall, so that to set up the minimum possible tilting between neighboring spins, and magnetocrystalline anisotropy energy, which would be instead minimized in case of zero domain wall extent;
- dipolar exchange length or exchange length, $\Delta_d = \sqrt{A/K_d} = \sqrt{2A/(\mu_0 M_s^2)}$ (~ 10 nm), representative of the characteristic length when dipolar and exchange energies compete (e.g. vortex core size).

Interface magnetic anisotropy

One of the major achievements of the Néel's phenomenological theory of magnetic anisotropy, developed in 1953, was the prediction of so called Néel magnetic anisotropy, arising from spin-orbit and crystalline potential, and responsible for Out-Of-Plane (OP) magnetization in ultra-thin films, in opposition to shape anisotropy which, by virtue of the demagnetizing field, favours an In-Plane (IP) magnetization [29]. Indeed, by uniquely considering dipolar and magnetocrystalline anisotropies, under the assumption of a uniformly magnetized system, it is possible to define an effective magnetic anisotropy energy density:

$$E = (K_u - K_d) \sin^2 \theta = K_{eff} \sin^2 \theta \quad (1.24)$$

where K_u is the uniaxial anisotropy constant and K_d is the dipolar constant. Magnetostatic energy induces an alignment of magnetization in directions characterizing small demagnetizing coefficient, that is in the plane for a thin-film. A usual condition for thin-films of Fe or Co is an extremely small bulk magnetocrystalline anisotropy, if compared to shape anisotropy: consequently, in absence of a strong Zeeman field perpendicular to the plane, an In-Plane (IP) magnetization will be favourable.

In the event of ultra-thin films, with a thickness lower than few nanometers, an extra term adds to the effective magnetic anisotropy, that is called interface magnetic anisotropy or surface magnetic anisotropy (for a free surface). Source of this additional contribution is the difference in environment of the surface or the interface atoms as compared to the bulk atoms in ultra-thin magnetic multilayer systems. Here, the break in the translational symmetry (SIA) due to the presence of planar interfaces and surfaces plays a major role in determining the anisotropy energy, under the physical mechanism of complex band hybridization and elastic stress due to lattice distortion [16].

The effective magnetic anisotropy, now resulting from the joint effect of the volume (K_v) and surface (K_s) contributions, where the former includes the bulk magnetocrystalline (K_u) and shape (K_d) anisotropy terms, is reformulated as follows:

$$K_{eff} = K_v + \frac{(K_{s_1} + K_{s_2})}{t} \quad (1.25)$$

with K_{s_1} and K_{s_2} , measured in J/m², accounting for the double surface or interface, and t representing the thickness of the ferromagnet.

The critical thickness t_c , defined as the thickness of the ferromagnetic layer in correspondence of which the interfacial or surface term exactly compensate for the volume contribution, is expressed as:

$$t_c = -\frac{(K_{s_1} + K_{s_2})}{K_v} \quad (1.26)$$

For a positive surface/interface contribution, below such critical thickness, K_{eff} may become positive, indicating that the interface anisotropy K_s exceeds the dipolar term K_d . This phenomenon induces the so called Perpendicular Magnetic Anisotropy (PMA), which is of great interest for technological applications as well as a prerequisite for the observation of magnetic skyrmions (Figure 1.6).

Practically, there exist three different physical scenarios:

- $t \leq t_{PM}$ ($\sim 0.2 - 0.5$ nm) : the thin-film is so slim to be non-magnetic, hence paramagnetic (PM), with the Curie temperature T_c below the room temperature T_R ;

- $t_{PM} < t < t_c$ ($\sim 1 - 2$ nm) : the thin-film is sufficiently thick to be ferromagnetic (FM) and enough thin to result in Out-Of-Plane (OP) magnetization, being the thickness t smaller than the critical thickness t_c ;
- $t > t_c$: the thin-film is sufficiently thick to be ferromagnetic (FM) but relatively too thick for the interfaces to play a significant role, leading to an enhanced bulk contribution, thus to a In-Plane (IP) magnetization.

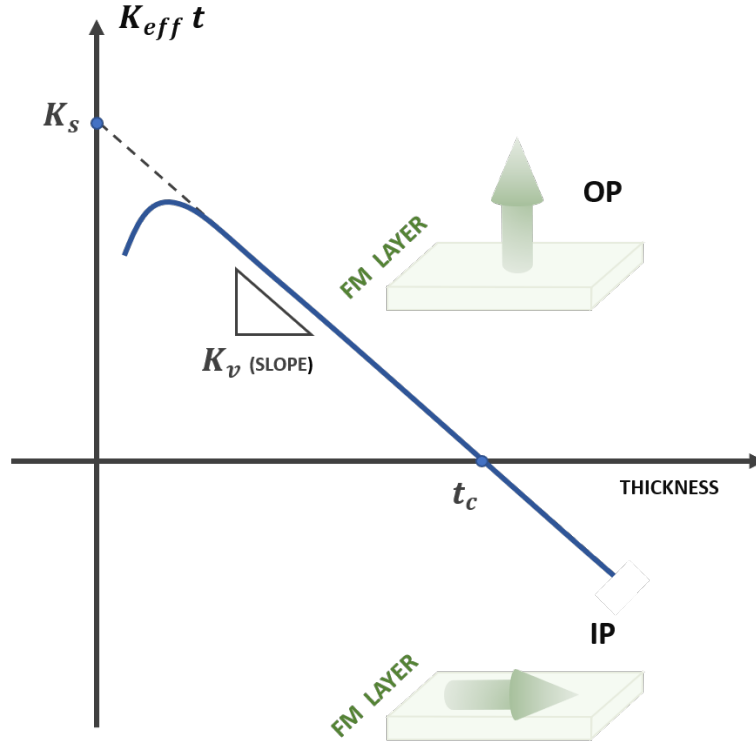


Figure 1.6: Effective magnetic anisotropy $K_{eff} \times$ FM thickness t vs. t . For positive K_{eff} values ($t < t_c$), the macrospin is Out-Of-Plane (OP); for negative K_{eff} values ($t > t_c$), the macrospin is In-Plane (IP).

It is interesting to notice how K_{eff} also incorporates the magnetoelastic anisotropy K_{mel} which exhibits the same behavior as magnetic interface anisotropy ($K_{mel} \propto 1/t$). This makes extremely hard to distinguish between these two intermingled contributions when K_{eff} is measured experimentally.

As stated before, complex band hybridization at the interfaces is one of the reasons for interface magnetic anisotropy. As a matter of fact, under the application of a voltage across a HM/FM/MOx thin-film, the electron accumulation or depletion at

the FM/MOx interface (short-time scale) and the ion migration from the MOx towards the FM/MOx interface (long-time scale), induce a modification of electronic orbital occupation, hence hybridization in the FM layer [16]. This phenomenon opens up the possibility of operating voltage gating for dynamic control of interfacial magnetic properties, e.g. to establish voltage-controlled magnetic anisotropy (VCMA). To quantify the variation of interface magnetic anisotropy energy per unit voltage per unit thickness, it is possible to define the so-called electric field efficiency:

$$\beta_{K_s} = \frac{\Delta K_s}{V} t_{ox} \quad (1.27)$$

where t_{ox} is the oxide layer thickness.

Dzyaloshinskii-Moriya Interaction

Dzyaloshinskii-Moriya Interaction (DMI) is an antisymmetric exchange interaction which opposes to the symmetric exchange contribution in the stabilization of chiral spin textures, that cannot be superimposed on their mirror images by any combination of rotations and translations. This physical mechanism permits the nucleation of solitonic magnetic objects, like Néel skyrmions. In particular, a one dimensional Néel skyrmion, obtained by drawing a transverse cross section of the two dimensional whirling magnetic texture across its diameter, is equivalent to a $2-\pi$ cycloidal progression of magnetization (Néel domain wall), with a unique sense of rotation dictated by the DMI vector. Magnetic skyrmions have been observed in systems with broken inversion symmetry (SIA) that display Dzyaloshinskii-Moriya (DM) exchange interaction, either in bulk structures like non-centrosymmetric crystals, presenting bulk-DMI, or in ultra-thin film multilayers of transition metals (FM) and materials with strong SOC (HM), exhibiting interfacial-DMI. Both Néel (hedgehog) and Bloch (spiral) skyrmions can be stabilized in the afore-mentioned systems owing to the interplay of Heisenberg exchange interaction, DMI and uniaxial perpendicular magnetic anisotropy (PMA) [30].

Quantum mechanically, the DMI energy has the following form:

$$\mathcal{E}_{DMI} = - \sum_{i < j} \mathbf{d}_{ij} \cdot (\hat{\mathbf{S}}_i \times \hat{\mathbf{S}}_j) \quad (1.28)$$

where $\hat{\mathbf{S}}_i$ and $\hat{\mathbf{S}}_j$ are atomic moment unit vectors at site i and j , respectively, and \mathbf{d}_{ij} represents the DMI vector.

The cross product governing the above equation clearly discloses how, for a given sign of the DMI vector, that is material dependent, the energy cost of the induced spin canting hinges on the sense of rotation from $\hat{\mathbf{S}}_i$ to $\hat{\mathbf{S}}_j$ around the rotational axis, represented precisely by \mathbf{d}_{ij} .

Two different models can be found in literature to depict interfacial–DMI (*i*DMI) in different magnetic systems that are, in chronological order, Fert–Levy model and Rashba model. This last recent proposition was experimentally observed for the first time in the work of Srivastava (2019) [16].

- **Fert–Levy model**

In the framework of Fert and Levy model [32], the *i*DM interaction between neighboring atomic spins *i* and *j* of a FM is described as a three-site mechanism, being indeed mediated by a third non-magnetic ion, e.g. belonging to an interfacing HM layer, with strong Spin-Orbit Coupling (SOT), as illustrated in Figure 1.7 a).

In this picture, the *i*DMI vector reads:

$$\mathbf{d}_{ij} = d_{ij} (\hat{\mathbf{r}}_{ij} \times \hat{\mathbf{n}}) \quad (1.29)$$

where $\hat{\mathbf{n}}$ is the normal to the ferromagnetic surface, and $\hat{\mathbf{r}}_{ij}$ is the unit vector connecting the two atomic sites.

The favoured rotation direction is thus driven by the sign of d_{ij} that, if positive, leads to a left-handed (anticlockwise) rotation while, if negative, to a right-handed (clockwise) rotation. As a result, by playing with interface combinations, it is possible to make the *i*DMI either vanishing or being enhanced. To bring some examples, being $d_{ij} > 0$ (respectively $d_{ij} < 0$) for Co on Pt (respectively Pt on Co), the spin canting is nullified for an ideal Pt/Co/Pt multilayered film and for perfectly symmetric stack in general; instead, in presence of a Ir/Co/Pt heterostructure, the overall *i*DMI is amplified because, as for Pt on Co, $d_{ij} < 0$ and the two contributions add up instead of cancelling out.

Park et al. (2016) [31] reported experimental evidences regarding the correlation between the *i*DMI strength and the work function of the non-magnetic layers interfaced to the magnetic layer. This may be due to the presence of a built-in electric field related to the work function difference at the interfaces, which induces a spin-orbit scattering.

- **Rashba model**

The Rashba model explains the *i*DMI mechanism in absence of a large SOC material, as is the case for ferromagnetic/insulator interface, e.g. Fe/MgO or Co/AlO_x, condition in which the Fert–Levy picture results incomplete [33]. In ultra-thin film systems, itinerant electrons of a 3*d* transition metal experience a momentum dependent effective magnetic field, which induces spin torque.

The Rashba effective magnetic field is the result of an interface electric field, depicted in Figure 1.7 b), arising due to broken inversion symmetry (SIA) and included in the SOC Hamiltonian, which takes the form:

$$H_R = \alpha_R \sigma \cdot (\mathbf{k} \times \hat{\mathbf{n}}) \quad (1.30)$$

where the Rashba parameter α_R , dependent on the interface electric field, reads

$$\alpha_R = -\frac{\hbar^2 E^2}{2m^2 c^2} \quad (1.31)$$

\mathbf{k} being the electron momentum and $\hat{\mathbf{n}}$ the outward normal to the FM film.

Accordingly, the Rashba effective magnetic field, removing the spin degeneracy of the interface energy bands, is expressed as:

$$\mathbf{B}_R \propto \alpha_R (\mathbf{k} \times \hat{\mathbf{n}}) \quad (1.32)$$

Particularly, the direction of the Rashba field determines the chirality of the magnetization canting, resulting from the exchange interaction between the local magnetic moments and the itinerant electron spins, precessing around the same B_R .

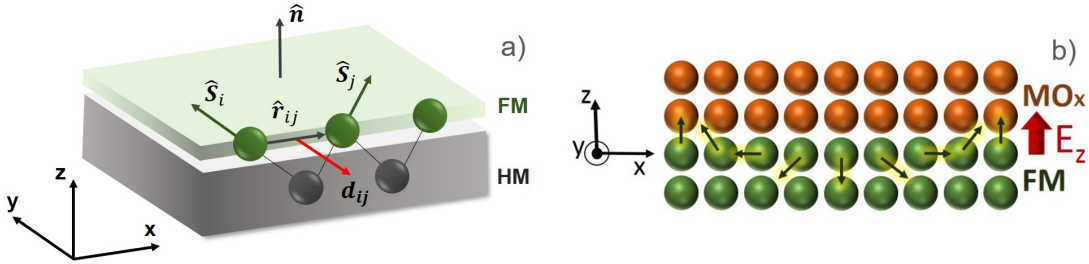


Figure 1.7: Illustration of a) Fert-Levy DMI and b) Rashba DMI [16].

By handling the i DMI in the continuum approximation, it is possible to quantify the relative strength of Fert–Levy and Rashba DMI contributions, under the definition of so called micromagnetic DMI constants, measured in J/m^2 and expressed respectively as:

$$D_{FL} \sim \frac{d}{a t} \quad (1.33)$$

$$D_R = \frac{4 \alpha_R m_e A}{\hbar^2} \quad (1.34)$$

with d the Fert–Levy DMI vector amplitude, a the lattice parameter of the FM, t the magnetic film thickness and A the exchange constant.

Being such interactions originated from the interface, the DMI constant D , beside being dependent on the thickness of the adjacent HM layer, exhibits an inverse proportionality dependence on the FM layer thickness t :

$$D = D_s/t \quad (1.35)$$

where D_s is called interface DMI constant.

It should be highlighted how the proportionality between the Rashba parameter and the interface electric field makes it possible the voltage tuning of interfacial–DMI, very interesting for dynamically controlling magnetic skyrmions [16]. In this context, it is useful to introduce the electric field efficiency, defined as the change in i DMI energy per unit voltage per unit thickness:

$$\beta_{DMI} = \frac{\Delta D}{V} t_{ox} \quad (1.36)$$

being V the applied voltage and t_{ox} the oxide layer thickness.

1.3.3 Landau–Lifshitz–Gilbert–Slonczewski equation

Purpose of dynamic micromagnetics is that of predicting the transient behavior of the magnetic system over short-time scales between two regime conditions, i.e. the time evolution of the magnetic configuration to reach a local energy minimum. This is accomplished by solving the Landau–Lifshitz–Gilbert–Slonczewski (LLGS) equation [34], derived by Slonczewski in 1996, a differential equation which predicts the rotation of the magnetization in response to torques. It represents an expansion of the standard Landau–Lifshitz–Gilbert (LLG) equation, to account for the current induced magnetization dynamics, beyond the precession and damping terms appearing in the latter, as shown in Figure 1.8.

The Landau–Lifshitz–Gilbert (LLG) equation, proposed by Gilbert in 1954 [35], was developed by formulating the damping term, responsible for energy loss, in analogy to the internal frictional force found in mechanics, i.e. viscosity, opposing the velocity vector. This equation is mathematically equivalent to the Landau–Lifshitz (LL) equation, developed in 1935 by Landau and Lifshitz [36], and historically representing the first formulation accounting for damping mechanisms, treated in a phenomenological manner. By introducing the gyromagnetic ratio $\gamma = ge/(2m_e)$, with g Landé factor ($g = 1$ for orbital magnetic moments, $g \sim 2$ for spin magnetic moments), and the dimensionless damping factor α , the LLG equation reads:

$$\dot{\mathbf{m}} = -|\gamma_0| \mathbf{m} \times \mathbf{H}_{eff} + \alpha \mathbf{m} \times \dot{\mathbf{m}} \quad (1.37)$$

where $\gamma_0 = \mu_0 \gamma$, being $\mu_0 = 4\pi \times 10^{-7}$ H/m the vacuum permeability.

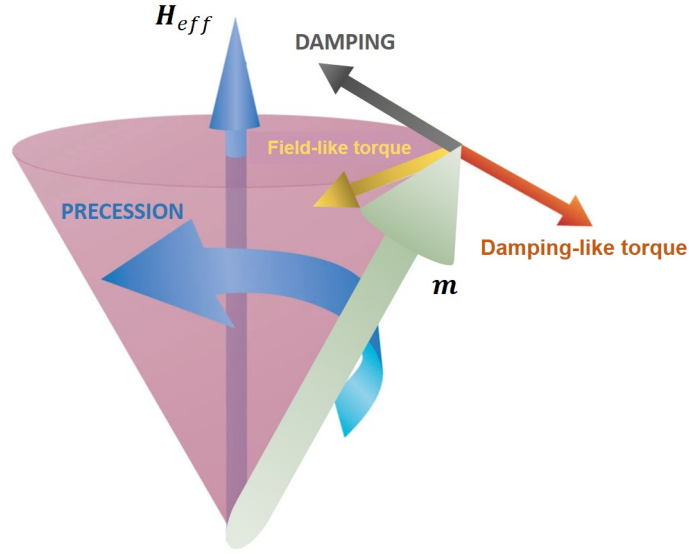


Figure 1.8: Illustration of the LLGS dynamics.

The equation 1.37 is composed by two different terms: the first, describing the precessional motion of the spin around the effective magnetic field, is responsible for the variation of rotation of directional axis and it is energy conservative; the second, providing a damping of the precession, is the influence that reduces oscillations, allowing the magnetization to be eventually aligned with the effective magnetic field.

The effective magnetic field \mathbf{H}_{eff} is construed as a conglomeration of competing terms, which concur to establish the magnetic portray of the material. Indeed, as illustrated before, the equilibrium distribution of magnetization in a piece of material is the result of the balance among coexisting energy terms, each one attributable to an equivalent magnetic field, either external (Zeeman) or internal (others), which attempts to align the magnetization along its own direction. For each internal energy contribution, related to the magnetization environment, the effective magnetic field can be computed according to the following equation:

$$\mu_0 \mathbf{H}_{eff} = -\frac{\partial E}{\partial \mathbf{M}} \quad (1.38)$$

The computation of the magnetization dynamics is accomplished by using micromagnetics simulator tools which integrate numerical methods for the resolution of the LLG(S) equation. At each simulation step t_n , the total effective magnetic field \mathbf{H}_{eff}^n is computed according to equation 1.38 starting from E^n , representing the total energy density characterizing the latest reduced magnetization vector \mathbf{m}^n .

This supplemented with a random effective magnetic field term which scales with temperature to account for thermal energy. The LLG differential equation is then numerically solved to extract the reduced magnetization vector at the adapted time step t_{n+1} , i.e. \mathbf{m}^{n+1} , as a function of which the updated total energy density E^{n+1} will be determined to get the reconditioned effective magnetic field \mathbf{H}_{eff}^{n+1} , in a recursive manner. The self-consistent loop can be terminated when the magnetization torque, matching the time derivative of the reduced magnetization vector $\dot{\mathbf{m}}$, is below a user-defined tolerance value, or after a certain number of steps (in which case, one checks the total energy convergence to a constant value) [37]. This iterative method can be summarized as here below (Figure 1.9):

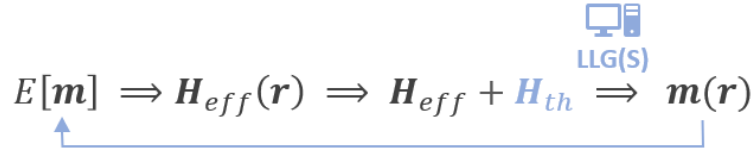


Figure 1.9: Computation of the magnetization dynamics.

In MuMax3, the micromagnetic solver used in the course of this thesis work, both the LLG equation and the Slonczewski spin momentum torque term are transformed into the Landau–Lifshitz (LL) formalism [37]:

$$\dot{\mathbf{m}} = -\frac{|\gamma_0|}{1 + \alpha^2} \left(\mathbf{m} \times \mathbf{H}_{eff} + \alpha \mathbf{m} \times (\mathbf{m} \times \mathbf{H}_{eff}) \right) + \boldsymbol{\tau}_{SL} \quad (1.39)$$

$$\boldsymbol{\tau}_{SL} = \beta \frac{\epsilon - \alpha\epsilon'}{1 + \alpha^2} \left(\mathbf{m} \times (\mathbf{m}_p \times \mathbf{m}) \right) - \beta \frac{\epsilon' - \alpha\epsilon}{1 + \alpha^2} \left(\mathbf{m} \times \mathbf{m}_p \right) \quad (1.40)$$

$$\beta = \frac{J_z \hbar}{M_s m_e d} \quad (1.41)$$

$$\epsilon = \frac{P(\mathbf{r}, t) \Lambda^2}{(\Lambda^2 + 1) + (\Lambda^2 - 1)(\mathbf{m} \cdot \mathbf{m}_p)} \quad (1.42)$$

where J_z is density of charge current flowing along the transverse axis of the nanopillar, M_s is the saturation magnetization, d is the free layer thickness, \mathbf{m}_p is the fixed layer magnetization, $P(\mathbf{r}, t)$ is the spin polarization, Λ is the Slonczewski parameter, characterizing the spacer layer, ϵ and ϵ' are the primary and secondary spin-torque parameters, respectively.

The equation 1.39 is composed of two different contributions: the first is the LL torque due to the effective magnetic field, while the second is the Slonczewski term, due to the application of a current.

Concerning the implementation of Sloncewski torque in equation 1.40, this is applicable to the case of transport in a nanopillar or, more generally, in a STT-MRAM. It is composed by two different terms that, in order of appearance, are called damping-like (DL) torque and field-like (FL) torque, in analogy with the damping and precession terms of LL equation, respectively.

In case of transport in a track, the magnetic state of a ferromagnet can be, as before, perturbed by an electric current, which exerts a Spin Transfer Torque (STT) on non-collinear magnetization. This phenomenon is again modeled by the Sloncewski term τ_{SL} , which is now expressed as [38]:

$$\tau_{SL} = -(\mathbf{u} \cdot \nabla) \mathbf{m} + \beta' \mathbf{m} \left((\mathbf{u} \cdot \nabla) \mathbf{m} \right) \quad (1.43)$$

where \mathbf{u} is the electron velocity vector, with an amplitude $u = g \mu_B m_p J_c / (2 e M_s)$, being J_c the current density flowing in the ferromagnetic layer, and β' is a dimensionless parameter.

In this equation, it is possible to discriminate between two different contributions: the former, often called adiabatic torque, acts in the plane of the incoming and outgoing electron spin direction, whereas the latter, known as non-adiabatic torque, is oriented perpendicular to that plane [17]. The non-adiabatic mode occurs in systems where the spacial magnetization variation is so fast that the transport electrons are unable to locally adapt their intrinsic angular moment to the magnetization texture they traverse [39].

In order to implement the Spin-Orbit Torque (SOT) switching using MuMax3, it is possible to impose in Equation 1.40 $\Lambda = 1$ and $\epsilon' = 0$ that, consistently with the convention of the study by Dai M. & Hu J. (2020) [18], returns:

$$\tau_{SL} = \frac{\beta \theta_{SH}}{2(1 + \alpha^2)} \left(\mathbf{m} \times (\boldsymbol{\sigma} \times \mathbf{m}) - \alpha (\boldsymbol{\sigma} \times \mathbf{m}) \right) \quad (1.44)$$

where θ_{SH} is the Spin Hall Angle in the underlying heavy-metal and $\boldsymbol{\sigma}$ the interface spin polarization.

Now, by recalling the definition of the Bohr magneton $\mu_B = e \hbar / (2 m_e)$, it appears quite evident the direct correspondence between the expression of the Spin Transfer Torque τ_{SL} and that of the Spin-Orbit Torque τ_{SOT} , that reads:

$$\tau_{SOT} = -\frac{\gamma}{1 + \alpha^2} \left(\mathbf{m} \times \mathbf{H}^{SOT} - \alpha \mathbf{H}^{SOT} \right) \quad (1.45)$$

being the effective field $\mathbf{H}^{SOT} = H_0 (\mathbf{m} \times \boldsymbol{\sigma})$, the prefactor $H_0 = \mu_B J_c \theta_{SH} / (\gamma e d M_s)$.

Indeed, by collecting the common factor H_0 and making it explicit, one obtains:

$$\begin{aligned}\tau_{SOT} &= \frac{\hbar\theta_{SH}J_c}{2(1+\alpha^2)m_e d M_s} \left(\mathbf{m} \times (\boldsymbol{\sigma} \times \mathbf{m}) - \alpha(\boldsymbol{\sigma} \times \mathbf{m}) \right) \\ &= \frac{\beta\theta_{SH}}{2(1+\alpha^2)} \left(\mathbf{m} \times (\boldsymbol{\sigma} \times \mathbf{m}) - \alpha(\boldsymbol{\sigma} \times \mathbf{m}) \right)\end{aligned}\quad (1.46)$$

As in case of STT transport in nanopillars, Equation 1.45 is comprised of two distinguished terms, where the former is name damping-like (DL) torque, modeling the Spin Hall effect (SHE), while the latter field-like (FL) torque, related to the Rashba-Eldestein effect (REE). Notice how the flow along the z axis is now determined by the spin current density $J_s = J_c \theta_{SH}$ (SOT in a track), equivalent to the spin polarized electric current density $J_z P$ of equation 1.40 (SOT in a nanopillar).

1.4 Micromagnetic solver

MuMax3 [37] is an open source GPU-accelerated micromagnetic simulation software developed at Dynamics of Functional Nano Materials (DyNaMat) group of the department of Solid State Sciences at Ghent University. The Program Developer is Arne Vansteenkiste. MuMax3 offers the possibility to implement extensive simulations on relatively cheap hardware and to collect results very shortly, by reason of high performance and low memory requirements.

The micromagnetic theory is a continuous model: in order to solve the Landau–Lifshitz–Gilbert (LLG) equation numerically, the system has to be discretized. To this purpose, MuMax3, mainly written in Golang, makes use of simulation domain finite difference (FD) discretization through a 2-D or 3-D single regular rectangular grid, consisting of equally sized orthorombic cells. The unit magnetization vector is supposed to be uniform in each unit cell, i.e. each cell is featured by a vector representing the associated magnetization amplitude and orientation. To be more precise, volumetric quantities, e.g. the magnetization and the effective magnetic field, are associated to the center of each cell, whereas coupling quantities, like the exchange strength, are depicted on the faces between the cells.

The choice of the cell size is quite delicate; indeed, to ensure a smooth variation of the magnetization between neighboring cells, the minimum linear dimension ℓ_{cell} has to be set such that to be smaller than the $\min(\Delta_u, \Delta_d)$, where Δ_u is the Bloch length and Δ_d the exchange length, the former measuring the typical width over which magnetization may rotate by 180° in a magnetic sample, the latter the relative strength of exchange and self-magnetostatic energies.

This condition is actually necessary but not sufficient: in chiral ferromagnets, the magnetization might vary on a length scale much smaller than Δ_d . Hence, one has also to verify that the maximum angle between two neighboring magnetization vectors in the simulation domain is smaller than $\theta_{max} \sim 0.35$ rad, otherwise the mesh nodes must be heightened in number. Nevertheless, one must also consider the trade-off that exists between the level of accuracy and the computation time.

Another point that has to be highlighted is related to the number of cells N_{cell} : the computation of the magnetostatic field is performed by resorting to the **CUFFT**, the NVIDIA CUDA Fast Fourier Transform library, the algorithm of which is highly optimized only if the set number of cells is 7-smooth (prime factors at most 7) or, even better, powers of 2. The cut-off range of the dipolar interaction in a given direction can be directly determined under the application of Periodic Boundary Conditions (PBC), causing the magnetization distribution in the simulation domain to evolve as an effect of the magnetostatic field of repeated magnetization images.

To save memory, MuMax3 allocates each cell into a region of index i , with i ranging between 0 and 256. Different region indices represent different materials, so that to create systems with non uniform material parameters, that can be also time dependent.

Finally, MuMax3 offers the possibility of constructing and running the simulations in an interactive mode, from within the web GUI.

R-K Solvers

In order to compute the approximate solution of Landau–Lifshitz–Gilbert (LLG) equation, MuMax3 can implement multiple explicit Runge–Kutta methods, a class of recursive methods, used in temporal discretization to numerically integrate ordinary differential equations. In general, the family of explicit Runge–Kutta methods is mathematically expressed as [40]:

$$y_{n+1} = y_n + h \sum_{i=1}^s b_i k_i \quad (1.47)$$

where

$$\begin{aligned} k_1 &= f(t_n, y_n) \\ k_2 &= f(t_n + c_2 h, y_n + h(a_{21} k_1)) \\ k_3 &= f(t_n + c_3 h, y_n + h(a_{31} k_1 + a_{32} k_2)) \\ &\vdots \\ k_s &= f(t_n + c_s h, y_n + h(a_{s1} k_1 + a_{s2} k_2 + \dots + a_{s,s-1} k_{s-1})) \end{aligned}$$

A given method is specified by fixing the value s , i.e. the number of steps, and the coefficients a_{ij} ($1 \leq j < i \leq s$), b_i ($i = 1, 2, \dots, s$) and c_i ($i = 2, 3, \dots, s$), where the matrix of coefficient a_{ij} is named *Runge–Kutta matrix*. b_i and c_i are instead labeled *weights* and *nodes*. It is possible to group the coefficients in a compact notation, called *Butcher tableau*:

$$\begin{array}{c|cccccc}
 0 & & & & & & \\
 c_2 & a_{21} & & & & & \\
 c_3 & a_{31} & a_{32} & & & & \\
 \vdots & \dots & & \ddots & & & \\
 c_s & a_{s1} & a_{s2} & \dots & a_{s,s-1} & & \\
 \hline
 & b_1 & b_2 & \dots & b_{s-1} & b_s &
 \end{array}$$

where $\sum_{j=1}^{i-1} a_{ij} = c_i$ for $i = 2, \dots, s$.

Starting from the magnetization at time t_n in a given cell of the simulation domain, the methods extract the magnetization at time step t_{n+1} , by adding to the former the time interval h , which is multiplied by a weighted sum (with weighting factors b_i) of all the slopes k_i estimated at different points of time and space discretized domains, based on previous extrapolation of other slopes, that are specific to the employed method.

Most important First-Same-As-Last (FSAL) solvers implemented in MuMax3 are:

- the third order convergence Bogacki-Shampine solver, with embedded second order method, used as default when attempting to relax the magnetization to its ground state using the function `relax()`, disabling the precession term in the LLG equation;
- the fourth order Dormand-Prince solver, with embedded third order method, the default for dynamical simulations, which can be run using command `run()`.

The aforementioned methods have the advantage of using adaptive time stepping, which makes it possible to achieve the relative best solution with the minimum computational cost: the time step dimension is changed during the computation without the need of setting a fixed size for the whole simulation. Hence, fixed step-size approach is not the most appropriate if the solution exhibits high variability over small subsets of the integration interval and little variability over larger ones, leading to unneeded computation for slow variations of the solution. At each computational step t_n , the truncation error e is estimated by:

$$e = m_{HO}^n - m_{LO}^n \tag{1.48}$$

where m_{HO}^n and m_{LO}^n are the magnetization values returned by the higher-order and embedded lower-order methods, respectively [41].

Afterwards, the time step size Δt_n is adapted such that the local error is as close as possible to the tolerance tol , equal to 1×10^{-5} as default in MuMax3: this procedure makes the local error to be uniformly distributed at each time step t_n so that to maximize the simulator performance still matching the wanted accuracy. In other words, if $e < tol$, Δt_n is increased; if $e > tol$, Δt_n is decreased.

It might be erroneously thought that larger order solvers are always capable of maximizing the efficiency because of the bigger time-step size required to gain the same accuracy. Actually, this is not the case, because the simulation time depends on both the time-step size and the number of torque evaluation performed at each time step, which increases with the order of the chosen R-K method.

MuMax3 is designed to operate in Single-Precision Floating Point Format (32 bit), which allows to run simulations in gaming GPU, much more budget friendly than professional GPU. As a result, by shrinking the time-step size below a certain threshold value, the truncation error does not decrease anymore.

1.5 Magnetic skyrmions

1.5.1 Characteristic quantities and topology

Magnetic skyrmions are chiral spin arrangements viewable as topological non-trivial whirling spin textures with particle-like properties, that have been predicted and observed in the event of broken inversion symmetry (SIA). The effect of the non-trivial topology, at least in presence of an enough large sample, is that of making the skyrmion topologically protected, thus contributing to its stability, and very resistant to pinning by defect during the current induced motion. Nevertheless, consequently to a Magnus-like force, current drifted skyrmions deviate from the direction of electron flow and may be annihilated upon contacting the racetrack edge. The underlying cause for the topological protection to become ineffective is the continuous variation of the topological number, that is no more an integer value (e.g. skyrmion to meron conversion) [42].

From a topological viewpoint, it is possible to characterize spin textures by means of a number called topological charge:

$$Q = \frac{1}{4\pi} \iint dx dy (\partial_x \mathbf{m} \times \partial_y \mathbf{m}) \cdot \mathbf{m} \quad (1.49)$$

It describes how many times the unit magnetic moments of a spin texture wrap around a unit sphere.

In case of a magnetic skyrmion, featured by a non-trivial spin texture, the topological charge is a non-zero, integer invariant, also called skyrmion number. As defined in Section 1.2, the polarity p outlines the magnetization orientation at the core of the skyrmion, that can be either parallel ($p = +1$) or antiparallel ($p = -1$) to the z axis, that is set to be oriented along the outward normal of the sample plane. This quantity p exhibits a strict correlation with the skyrmion number Q . Indeed, for these two latter cases, the Equation 1.49, opportunely reformulated in polar coordinates, takes the form:

$$Q = p \cdot W \quad (1.50)$$

$$W = \frac{1}{2\pi} [\Phi(\varphi)]_0^{2\pi} \quad (1.51)$$

where W is the winding number and $\Phi(\varphi)$ is defined in Figure 1.10 b).

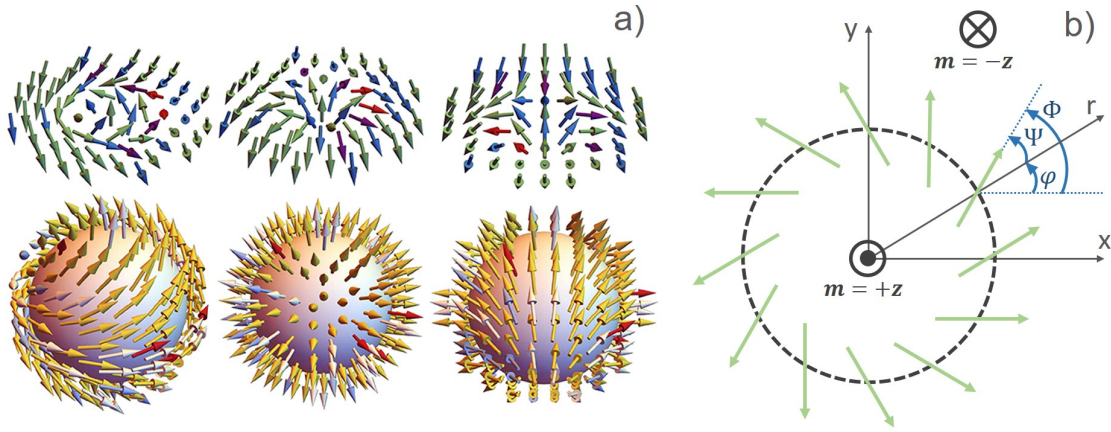


Figure 1.10: a) Illustration of magnetic skyrmions [43]. Bloch (left) and Néel (middle) skyrmions with topological charge $Q = +1$ and polarity $p = +1$. Anti-skyrmion (right) with topological charge $Q = -1$ and polarity $p = +1$. The top row depicts the 2D magnetic configuration of these spin textures, while the bottom row the projection of the magnetic textures on the unit sphere. b) Schematics of a magnetic skyrmion with polarity $p = +1$, winding number $W = +1$ and helicity $0 < \Psi < \pi/2$; definition of polar coordinates (r, φ) and spherical coordinates $(1, \Phi, \theta)$ for magnetization \mathbf{m} . The green arrows depict the domain wall orientation of magnetization where purely In-Plane (IP).

Magnetic spin textures with $W = \pm 1$ are called skyrmion and antiskyrmion, respectively. Accordingly the topological charge is equal to $Q = +p$ for the skyrmion and to $Q = -p$ for the antiskyrmion [43].

It is interesting to notice how the spin orientation at the skyrmion center, aligned with the z axis, is always antiparallel to the background magnetization of the ferromagnetic material hosting the topological quasi-particle, which is indeed endowed with Perpendicular Magnetic Anisotropy (PMA), resulting in an Out-Of-Plane (OP) easy direction of magnetization.

Bloch and Néel skyrmions, both characterized by $Q = +p$, can be distinguished only by the value of the helicity number Ψ , which is uniquely determined by the type of DMI, i.e. of bulk or interfacial origin. Helicity can be defined as the angle of global rotation around the z axis, as illustrated in Figure 1.10 b). A Néel skyrmion can have Ψ equal to either 0 or π , while for a Bloch skyrmion it can be either $\pi/2$ or $3\pi/2$ [43]. Figure 1.10 a) provides a picture of the afore-mentioned spin textures.

Chiral domain walls, and thus magnetic skyrmions, result from a competing effect involving Heisenberg symmetric exchange and Dzyaloshinskii-Moriya (DM) anti-symmetric exchange interactions, energetically favouring collinear and non-collinear spin arrangements, respectively.

Magnetic skyrmions should not be confused with magnetic bubbles, that are actually “cylindrical magnetic domains whose magnetization is reversed to that in the remainder of the thin magnetic layer in which they are present” [44]. However, as in the case of the magnetic skyrmions, “these simple domain configuration will only occur if the magnetic material has a uniaxial anisotropy with the easy axis of magnetization perpendicular to the surface” [44]. Magnetic bubbles can be either achiral, being enclosed by a non-chiral domain wall, or chiral. In this latter case, they have the same topology as skyrmions and are hence referred to as skyrmionic bubbles. Differently from magnetic skyrmions, stabilized by DMI and the size of which is mainly insensitive to the effect of a magnetic field, magnetic bubbles are stabilized by dipolar energy, making them extremely responsive to the Zeeman field [45].

1.5.2 Skyrmion motion under current

The control and reliability of the current induced motion of skyrmions is an essential prerequisite for potential involvement of such topological solitons in future solid state devices, in such a way to overcome problems related to the domain wall pinning by defects and high driving current density. The current driven skyrmion dynamics is the outcome of the spin torque acting on the magnetic texture, resulting from two well distinguished physical mechanisms that are: the Current In-Plane Spin Transfer Torque (CIP-STT), for an electric current directly injected and spin polarized by the ferromagnet (FM), and Spin-Orbit Torque (CIP-SOT), in case of an electric current flowing in the adjacent heavy metal (HM) layer in presence

of structural inversion asymmetry (SIA). The latter phenomenon, superior both in terms of induced skyrmion velocity and power dissipation [1], results from the torque induced by the spin accumulation at the FM/HM interface owing to either the transverse spin current originated from the Spin Hall Effect (SHE), that is a bulk effect, or from the 2-D charge-to-spin conversion caused by the Rashba-Edelstein effect (REE), ascribed to the spin-momentum locking of the spin-polarized surface states in presence of SIA (Figure 1.11).

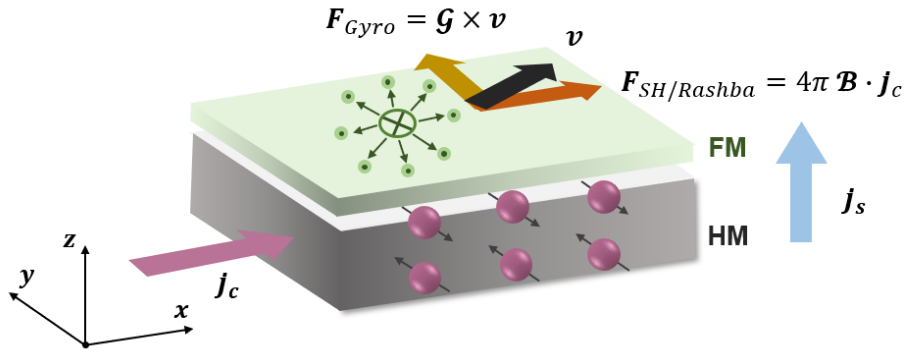


Figure 1.11: Schematics of skyrmion motion under applied current (SOT).

The Thiele differential equation [46] analytically describes the steady-state motion of magnetic skyrmions. For the CIP-SOT case, this equation incorporates, along with a dissipative term, the topological Magnus-like force, characterizing the anomalous deviation of the skyrmion trajectory from the longitudinal electrical flux:

$$4\pi \mathcal{B} \cdot \mathbf{j}_c + \mathcal{G} \times \mathbf{v} - \alpha \mathcal{D} \cdot \mathbf{v} = 0 \quad (1.52)$$

where the tensor \mathcal{B} is the spin torque efficiency of the SHE, \mathbf{j}_c is the current density flowing in the HM, with $j_c = j_s/\theta_{SH}$, j_s being the spin current density and θ_{SH} the Spin Hall Angle in the heavy-metal; \mathbf{v} is the skyrmion drift velocity, $\mathcal{G} = (0, 0, -4\pi \frac{M_s t}{\gamma} p)$ is the gyromagnetic coupling vector with γ gyromagnetic ratio; α is the Gilbert damping coefficient and \mathcal{D} the dissipative tensor.

The first term describes the longitudinal motion of the skyrmion due to SOT, consistent with the direction of the electric current. Responsible for this is the damping-like torque, representative of a magnetization dependent effective magnetic field.

The latter allows us to predict which will be, time by time, the evolution of the magnetization in each point of the spin texture, that adapts to the afore-mentioned Zeeman stimulus, as well as to visualize the longitudinal skyrmion motion. The equivalent damping-like magnetic field reads:

$$\mathbf{H}_{DL} = H_{DL} \left(\mathbf{m} \times (\mathbf{j}_c \times \mathbf{z}) \right) \quad (1.53)$$

where the term H_{DL} depends on the SHA θ_{SH} , which is material dependent and can be either positive or negative depending on the HM. It determines, together with the skyrmion chirality, dictated by the i DMI sign, the net displacement of the skyrmion along or against the current direction.

The second term, clearly oriented transverse to the skyrmion drift motion imposed by the SHE, is the gyrotropic force, representing an equivalent of the hydrodynamics Magnus force. It describes the so called Skyrmion Hall Effect (SkHE), similarly to the Hall Effect for electric charges. Indeed, the deflection direction is dictated by the sign of the skyrmion number and it may cause the skyrmion, no more topologically protected, to be annihilated when crashing into the track border [16].

The third term accounts instead for dissipation, acting as viscous force in a liquid. For a skyrmion radius R much larger than the domain wall width Δ , the dissipative tensor diagonal elements reduce to $D \approx \frac{M_{st}}{\gamma} 2\pi \frac{R}{\Delta}$. This makes it particularly easy to evaluate the Skyrmion Hall Angle Θ_{SkH} , defined as the angle between the electric current density injected the HM (\mathbf{j}_c) and the skyrmion velocity (\mathbf{v}):

$$\Theta_{SkH} = \frac{G}{\alpha D} \sim -\frac{2\Delta}{\alpha R} \quad (1.54)$$

1.6 Overview and objectives of the thesis

Schematics in Figure 1.12 helps to shorthand ideas about the logic flow at the basis of **micromagnetic simulations**, representing the key instrument employed in the course of this thesis, to investigate and characterize the physics underneath magnetic skyrmions and, more generally, non-trivial spin textures.

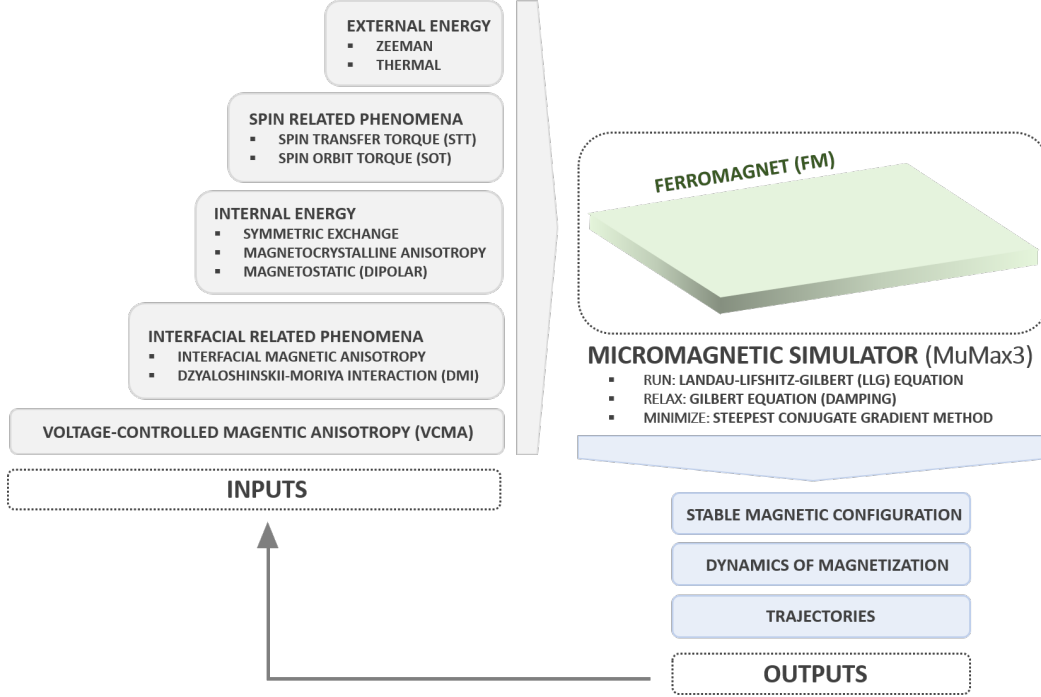


Figure 1.12: Schematics of micromagnetic simulator logic flow.

1. In particular, the first purpose of this thesis work is to perform a numerical characterization of skyrmionic bubbles static properties, for Pt/Co/MgO-based systems exhibiting perpendicular magnetic anisotropy (PMA). The static analysis is aimed to explore the influence of a **Zeeman field**, the impact of the **sample geometry** and the effect of **Periodic Boundary Conditions** on the effective size and shape of the skyrmionic bubble. This is supplemented with the computation of a **phase diagram**, designed to reveal the combinations of i DMI and uniaxial anisotropy coefficients that make it possible to stabilize the chiral magnetic bubble in zero magnetic field conditions, with and without PBC. These phase diagrams will be used as a guide to explore the skyrmion stability under a gate voltage.

As both i DMI and interface anisotropy are tuneable under voltage gating with a given efficiency, such phase diagrams may help in predicting the required electric field efficiencies for dynamic control of magnetic skyrmions, resulting from the voltage control of interfacial magnetic properties. The extraction of the magnetic hysteresis closes the static portraiture of the skyrmionic bubble.

2. The second main objective is to explore **peculiar stable states** for this magnetic stack starting from a demagnetized state. Particularly, they are found to be the **skyrmion bubble lattice** (1) and the **multidomain state** (2). Notably, it will be shown that, when the magnetization is randomly initialized to mimic a fully disordered state, the system can land either on the energy minimum (1) or (2), depending on the applied magnetic field. In particular, the skyrmion bubble lattice is stabilised by relaxing the initial random state at $\mu_0 H_{app} = -50$ mT and it preserves its stability by stepping the field up to $\mu_0 H_{app} = 0$ mT. As far as the multidomain state is concerned, this is instead stabilised in conditions of no applied magnetic field. Accordingly, for $\mu_0 H_{app} = 0$ mT, both the magnetic distributions are potentially achievable, depending on the magnetic history of the sample.
3. In the frame of the aforementioned multidomain state, domain walls and non-trivial spin textures – such as skyrmionic bubbles, **domain wall skyrmions** and **double skyrmions** – have been observed to survive simultaneously. More details about the latter two topological solitons will be provided in Section 2.3. The multidomain state will be proved to be stable against non-zero temperature and resilient to granularity, for crystallites of varying dimensions. The new topological excitation occurring in the unveiled multidomain state, here called double skyrmion, consists of a skyrmionic bubble with a domain wall skyrmion, i.e. $2 - \pi$ in-plane rotation of magnetization inside the otherwise Néel homochiral domain wall. Actually, the core issue of this thesis work is exactly constructed upon this distinct novel non-trivial spin texture, with the aim of carrying out a full characterization of its static and dynamic behavior. Specifically, the double skyrmion will be shown to be extremely responsive to an external magnetic field and capable of withstanding both reduction and sign reversal of the i DMI coefficient. The double skyrmion characteristic curves, highlighting the evolution of the total energy and the effective diameter versus $\mu_0 H_{app}$ and D , will be compared to those featuring the conventional skyrmionic bubble. The static analysis is complemented with the inspection of the STT and SOT driven dynamics for different geometries and amplitudes of the injected current. In particular, for the SOT induced motion, it will be proved the existence of different current regimes, offering the possibility of either driving the topological charge along the track or annihilating it, opening the path to conceive logic devices. Also, a potential solution to nucleate these double skyrmions and further manipulate them will be presented.

Chapter 2

Micromagnetic simulations

All the micromagnetic simulations conducted during this thesis experience refer to multilayered thin-film systems of type Pt/Co(0.9 nm)/MgO, with associated simulation parameters listed in Table 2.1.

Film lateral size: L (nm)	500
Film thickness: t (nm)	0.9
Saturation magnetization: M_s (kA/m)	1420
Exchange stiffness: A (pJ/m)	16
Uniaxial anisotropy constant: K_u (MJ/m ³)	1.36
DMI constant: D (mJ/m ²)	1.27
Damping factor: α	0.37
Exchange length: Δ_d (nm)	3.43
Bloch length: Δ_u (nm)	3.55

Table 2.1: Pt/Co/MgO simulation parameters [47].

This sample has been already fully characterized in the past, where the nanometric thickness of the trilayer ultra-thin film represents an important prerequisite for the development of efficient skyrmion-based devices. In more detail, Boule et al. (2016) [5] succeeded in demonstrating experimentally for the first time stable magnetic skyrmions in sputtered ultra-thin Pt/Co(0.9 nm)/MgO nanostructures at room temperature and zero external magnetic field, as well as the large interfacial-DMI of such systems. Before this demonstration of skyrmions in sputtered ultra-thin films, chiral skyrmionic structures had been experimentally observed only in bulk specimens and in epitaxial ultra-thin films, in presence of an external magnetic

field or in low temperature regime. Afterwards, Juge et al. (2019) [6] reported the fast steady-state current driven motion of Néel skyrmions at room temperature, with effective diameter in the range of 100 nm for the same magnetic stack. In particular, they proved the possibility to establish a spin driven dynamics of the magnetic skyrmions under Spin–Orbit Torque (SOT), with a drive-dependent Skyrmion Hall Effect (SkHE) due to pinning and a speed up to 100 m/s (Figure 2.1).

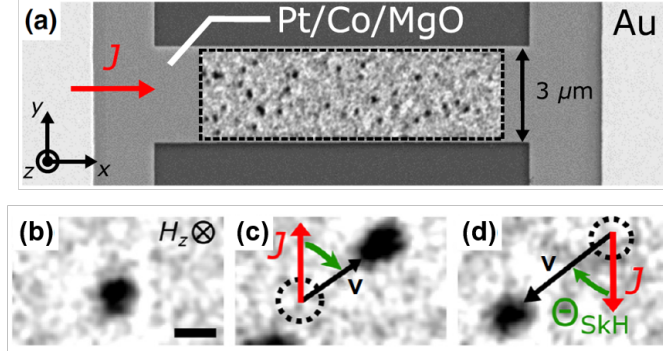


Figure 2.1: a) X-ray Magnetic Circular Dichroism coupled to Photoemission Electron Microscopy (XMCD-PEEM) image (black dashed rectangle) showing isolated skyrmions in the track, superimposed on a Scanning Electron Microscopy (SEM) image of the device. b) – d) A sequence of XMCD-PEEM images showing a skyrmion after two consecutive 8 ns current pulses with opposite polarities (the scale bar is 200 nm). From Juge et al. (2019) [6].

As stated in the previous chapter, the energy landscape of a magnetic sample can be viewed as composed of several local energy minima, representing equilibrium or stable magnetization configurations, that are separated by energy barriers. In a real sample, the transition between two stable states can be accomplished either by thermal effects and precessional switching or by modulating the height of the energy barrier under the action of an external torque acting on the magnetization, operated by an external magnetic field or an electric current. At simulation level, distinct stable states lying on the energy landscape can be reached by relaxing different initial magnetization patterns, provided as inputs to the simulator. For the studied material, in the range of negative magnetic field values, the fundamental magnetization state, stabilized by symmetric exchange energy, was observed to be the single domain state (Figure 2.16). In contrast, in zero magnetic field conditions, the effect of dipolar is to favor the presence of magnetic domains to reduce the stray field radiated out of the sample. The ground magnetization state is thus represented by the magnetic skyrmionic bubble.

During the thesis work, the attention was focused on four distinguished peculiar stable states, that are: the magnetic skyrmionic bubble, the skyrmion bubble lattice, the multidomain state and the more exotic double skyrmion, that has never been reported to be stable before. Main results collected for the just mentioned magnetic configurations will be detailed in the following sections.

2.1 The magnetic skyrmionic bubble

Magnetic skyrmions and skyrmionic bubbles, both observed in magnetic thin-film with Out-Of-Plane (OP) *easy axis*, are topological spin structures, distinguishable for the characteristic size and the energy source accounting for their stabilization, in spite of sharing the same topology ($Q = +1$). Indeed, the magnetic skyrmion, mainly stabilized by Dzyaloshinskii-Moriya Interaction (DMI), is ideally represented through a singular point perpendicularly magnetized at its core center, encircled by a ring-shaped Néel domain wall. In real samples, this topological soliton corresponds to a circular spin texture with a radius of the order of few Δ_u (Bloch length) or less, only weakly responsive to an applied magnetic field. In contrast, the magnetic skyrmionic bubble is representative of an intermediate size soliton, with a characteristic radius ranging from few tens to few thousands of nanometers. It is stabilized mainly by dipolar interaction, is thus extremely sensitive to external magnetic fields, and presents a longer lifetime at room temperature than skyrmions [45], [48].

In the present work, micromagnetic simulations were employed to investigate the effect of an applied magnetic field, the impact of the sample geometry and the influence of Periodic Boundary Conditions (PBC) onto a magnetic skyrmionic bubble.

Initial state

The static analysis of the magnetic bubble was carried out by setting $N_{cells} = 256 \times 256$, value that returns $\ell_{cell} \sim 1.95 \text{ nm} < \min(\Delta_d, \Delta_u) = 3.43 \text{ nm}$. In order to relax the system into the skyrmion bubble state, it was chosen as input for the simulator a uniform magnetization state $m = (0, 0, +1)$, redressed by an oppositely magnetized central circular spot of size 100 nm. The abrupt, step-like alteration of magnetization occurring at the frontier between the two magnetic domains, that are 180° apart, is extremely costly in terms of symmetric exchange energy which, in case of a ferromagnetic material, pushes for to make the neighboring spins oriented parallel to each others. Consequently, a left-handed (LH) circular Néel domain wall is formed due to positive sign of DMI coefficient, that leads to a characteristic smooth rotation of the magnetization around the domain wall longitudinal axis.

Under the local assumption of planar domain wall, the Néel domain wall energy density, including contributions from exchange, anisotropy and DMI, can be expressed as:

$$\sigma_w = 4\sqrt{AK_{eff}} - \pi|D| \quad (2.1)$$

where A_{ex} is the exchange stiffness (J/m), $K_{eff} = K_u - 1/2\mu_0 M_s^2$ is the effective anisotropy (J/m³) and D is the effective DMI constant (J/m²). Here, the DMI has the effect of making the Néel DW more energetically favourable with respect to the Bloch DW, the energy of which is provided just by the first term of Equation 2.1 – even if volume charges usually prevent the formation of Néel DW in PMA films. What is also important to highlight is the fact that the characteristic equilibrium radius of the skyrmionic bubble does not depend on the size of the initial round spot, but it is just dictated by the magnetic parameters and the effective magnetic field the thin-film experiences. An overall view of the obtained results is provided in Figure 2.2.

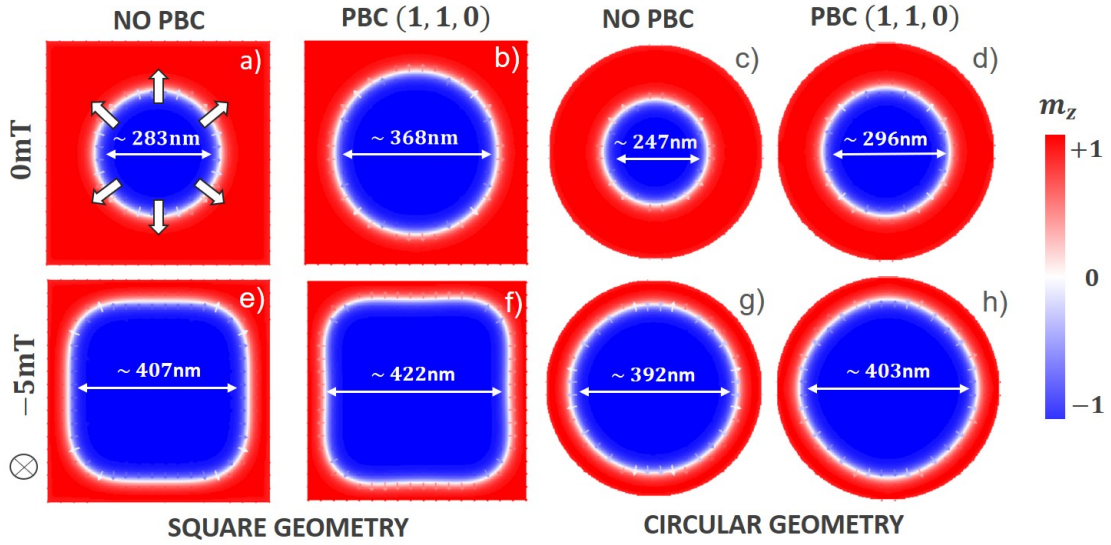


Figure 2.2: Schematics depicting the impact of magnetic field, sample geometry and Periodic Boundary Conditions (PBC) onto a magnetic skyrmionic bubble. In the first line the skyrmionic bubble stabilized with no external magnetic field for a), b) square geometry and c), d) circular geometry, with and without PBC. In the second line the skyrmionic bubble stabilized in presence of $\mu_0 H_{app} = -5$ mT for e), f) square geometry and g), h) circular geometry, with and without PBC. The bold arrows in a) illustrate the purely In-Plane (IP) magnetization vectors. The white arrows in the inner domains indicate the skyrmionic bubble diameter. The color scale is associated to the Out-Of-Plane (OP) magnetization.

Zeeman field

As illustrated in Figure 2.2, when a negative magnetic field collinear with the z axis is applied, the inner magnetic domain enlarges at the expense of the outer one, so that to minimize the Zeeman energy or, equivalently, as an effect of the torque induced by the Zeeman field onto the magnetization. Thus, in accordance with literature, it is possible to tune the size of the skyrmion bubble by modulating the strength of the magnetic field. The diameter of the skyrmionic bubble is extracted by computing the difference, in absolute value, of the two x coordinates at which the z component m_z of the unit magnetic vector is zero (fully IP magnetization), as reported in Figure 2.3 a). In the same figure, it is possible to observe how at the sample edges, i.e. for $x = 0$ and $x = L$, m_z is slightly smaller than the unit, because of the tilting of the magnetization vectors to reduce surface charges.

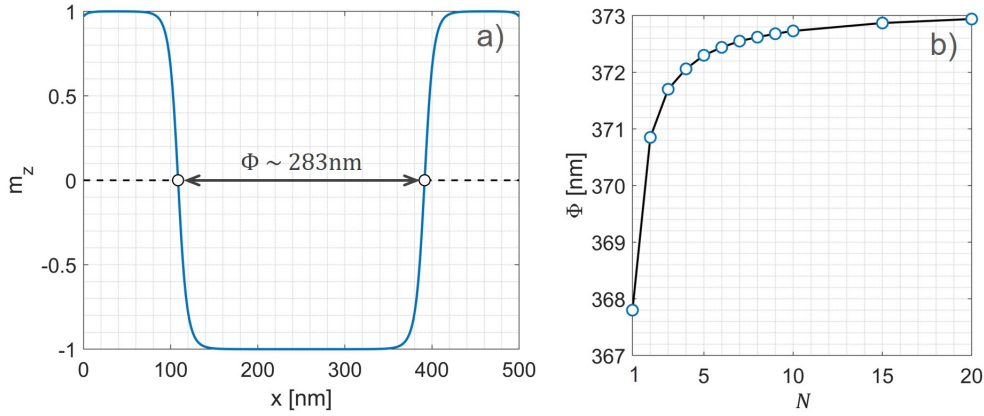


Figure 2.3: a) Extraction of magnetic bubble diameter Φ for no PBC case.

b) Magnetic bubble diameter Φ vs. PBC $(N, N, 0)$ for $N = 1, 2, \dots, 20$.

Both graphs refer to the condition $\mu_0 H_{app} = 0$ mT.

Periodic Boundary Conditions

A second observed characteristic behavior is the enlargement of the magnetic bubble in response to imposed PBC (N_x, N_y, N_z) , which introduces a periodic repetition of the simulation domain, with the dipolar field taken from the N_i next neighboring samples along x , y and z directions. In the present case, the periodicity is just set to be in the plane, i.e. $N_x, N_y \neq 0$ and $N_z = 0$. The strength of the dipolar field decreases as the distance from the magnetic source increases. This can be easily visualized by considering the mutual energy of two pinpoint magnetic dipoles μ_1 and μ_2 , both aligned along z axis and separated by a distance r :

$$\mathcal{E}_{12} = \frac{\mu_0 \mu_1 \mu_2}{4\pi r^3} (1 - 3 \cos^2 \theta) \quad (2.2)$$

where $\mu_0 = 4\pi \times 10^{-7}$ H/m is the vacuum permeability and θ is the angle between $\boldsymbol{\mu}_1$ (collinear to z) and the vector \mathbf{r} separating the two dipoles. Thus, it is energetically preferred for two magnetic moments placed side by side to align antiparallel, so that to close the stray field flux lines and reduce the surface charges (Figure 2.4).

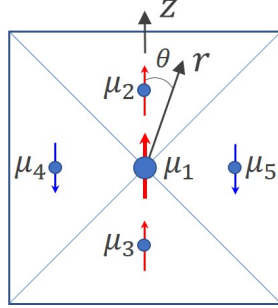


Figure 2.4: Simply view on dipolar interaction.

Accordingly, one could mistakenly expect a shrinkage of the magnetic bubble, as a result of identical copies now placed all around, that present the same core polarization. However, when PBC are set, also the magnetic background, that is the external magnetic domain in the immediate surrounding of the magnetic bubble, is expanded, which exerts a major effect as a result of the closer distance with respect to the nearest neighboring bubble replicas.

When the value of $N_x = N_y = N$ is enlarged, the magnetic bubble width exhibits a step increase up to $N = 3$, followed by a saturation tendency of the diameter $\Phi(N)$ function for larger N values, as Figure 2.3 b) shows. This behavior can be ascribed to two different effects: first, the repulsion from the edges, which confine the magnetic material; second, the even weaker influence of the stray field as the distance of the simulation window replicas increases. This latter analysis was performed considering square geometry, but the same qualitative behavior is expected and observed for circular geometry, as illustrated in Figure 2.2 c), d) and g), h).

Sample geometry

The shape of the sample also plays a big role: practically, while expanding, the skyrmionic bubble starts to interact with the sample edges and adapts to the geometrical contour of the sample, being the circular skyrmionic bubble converted into a square-like structure for a negative magnetic field applied in a square simulation window. This can be interpreted as the effect of the repulsion exerted by the edges of the sample which, if contacted, would lead to the bubble annihilation, turn into a uniform magnetization vector state.

Phase diagram

To supplement the static analysis, phase diagrams were extracted, so to inspect the regimes of skyrmionic bubble existence for different combinations of i DMI and uniaxial anisotropy constants. The goal of this study is to mimic the effect of a gate voltage tuning of both interfacial anisotropy and i DMI, with different efficiencies depending on material parameters. The analysis was first carried out in absence of PBC. The related phase diagram is depicted in Figure 2.5. Here, for the three top lines ($\Delta K_u = +5\%$, $0\% - 5\%$), the effective magnetic anisotropy constant is positive ($K_{eff} = K_u - 1/2 \mu_0 M_s^2 \sim 161 \text{ kJ/m}^3$, 93 kJ/m^3 , 25 kJ/m^3) and the magnetization is expected to be Out-Of-Plane (OP). However, a K_{u_0} variation of -10% in the bottom line is enough strong to result in a sign change of the effective magnetic anisotropy constant ($K_{eff} \sim -43 \text{ kJ/m}^3$), i.e. the Out-Of-Plane (OP) magnetic anisotropy is converted into an In-Plane (IP) magnetic anisotropy. By moving along an horizontal line in Figure 2.5, characterized by a fixed value of K_u , thus by an IP or OP effective magnetic anisotropy, it is possible to observe how the i DMI strength affects the magnetization distribution, where D determines the absolute value and even the sign of the domain wall energy σ_w .

There is basically one major physical effect, analytically modeled by Equation 2.1, that one has to be bear in mind to well interpret the magnetic behavior revealed by the phase diagram: by increasing the i DMI constant D (respectively uniaxial anisotropy constant K_u), the energy cost for the nucleation of Néel domain walls diminishes (respectively raises). This concept can be easily visualized in case of $K_u = K_{u_0}$ (0% of variation), which imposes OP magnetization.

- For positive D_0 variations (i DMI reinforcement), the system switches from the skyrmionic bubble regime to the spin spiral state (negative σ_w) where, for a given cross sectional line trajectory, the magnetization vector undergoes a continual cycloidal rotation around the i DMI vector. This phenomenon occurs because the domain wall energy becomes negative thus creating many domain walls stabilizes the system.
- For negative D_0 variation (i DMI reduction), the length of the Néel domain wall enclosing the topological soliton is first reduced, through the gradual conversion of the skyrmionic bubble into a magnetic skyrmion, eventually vanishing into a uniform magnetization state. This is due to an increase of the domain wall energy cost.

The same trend is re-proposed for a K_{u_0} variation of -5% , with the only difference of reducing the minimum D value needed to promote the spin spiral state.

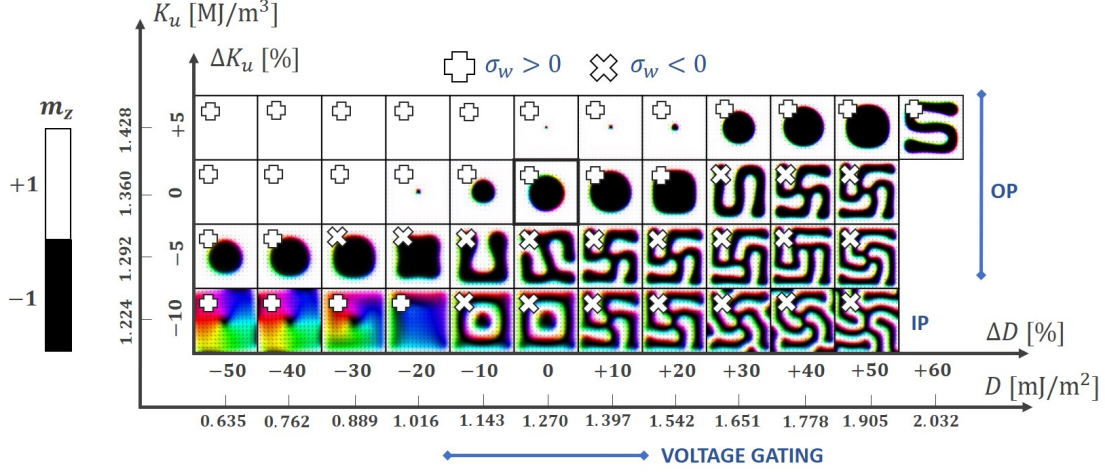


Figure 2.5: Phase Diagram computed for PBC $(0, 0, 0)$ and $\mu_0 H_{app} = 0$ mT. On x axis D and its percentage of variation ΔD , on y axis K_u and its percentage of variation ΔK_u , with $D_0 = 1.27$ mJ/m² and $K_{u0} = 1.36$ MJ/m³. Colors correspond to In-Plane (IP) magnetized regions (the absolute color scale is meaningless). The color gradient indicates a rotation of IP magnetization.

By further reducing K_u , with a total variation of -10%, as stated before, the effective magnetic anisotropy becomes negative. Upon this, two main effects can be observed.

- First, for a fixed D value, large enough to have the spin spiral state stabilized ($\sigma_w < 0$), the transverse width of the Néel domain wall is expanded if compared to the foregoing line, because $K_{eff} < 0$ favours the IP magnetization. To provide a practical example, it is possible to compute the percentage of IP component of magnetization in the sample at $\Delta D = +20\%$, which is equal to $m_{IP} = 49\%$ (respectively 63%) m_{TOT} for $\Delta K_u = -5\%$ (respectively -10%).
- Second, below a critical i DMI constant value, found to be $D_c \sim 0.9 D_0$, the sample becomes first fully IP magnetized and then, for reduced i DMI, magnetic vortices are stabilized. The transition point between spin spiral to IP magnetization state is verified in correspondence of a sign change of the domain wall energy σ_w , reported in Equation 2.1, which, for $D < D_c$, becomes positive. This causes the Out-Of-Plane (OP) magnetization to be converted into an In-Plane (IP) magnetization, promoted by the negative K_{eff} sign. The occurrence of magnetic vortices is verified for all the combinations of D and K_u values, within the explored range (not wholly shown) $\Delta K_u \in [-50, -20]\%$.

A +5% increase of K_{u0} prevents the skyrmionic bubble nucleation even for a D_0 reduction of 10%; a K_{u0} increment of 10% instead restricts the magnetization configuration to the single domain state ($m_z = +1$) (not shown).

In the cases when the spin spiral or the single domain states are obtained at zero magnetic field, there exist minimum absolute OP Zeeman field values that have to be applied in order to carry the sample in the magnetic skyrmionic bubble regime. In particular, in presence of spin spiral state, the Zeeman field needs to be positive, i.e. oriented along $+z$, in such a way to constrict the spiraling (black) magnetic domain(s), directed along $-z$, into a unique reshaped circular (black) magnetic domain. On the opposite, for a uniform (white) magnetization state, with magnetization oriented along $+z$, an oppositely polarized Zeeman field is required, so that to restore the (black) magnetic domain, oriented along $-z$, which constitutes the magnetic skyrmionic bubble.

The analysis was then carried out in presence of PBC (10, 10, 0) (not shown), where $N = 10$ leads to magnetic bubble size saturation regime, as illustrated in Figure 2.3. The application of Periodic Boundary Conditions has the effect of enlarging the (black) magnetic domain polarized along $-z$ (not shown). This fact has two main consequences. First, the skyrmionic bubble area is increased, because the magnetostatic field favouring its core is amplified; second, the i DMI value needed for the inner magnetic domain to deviate from the simple circular or square geometry is reduced. Also, in presence of PBC, magnetic vortices are never observed. This may be understood as vortices appear in order to decrease the surface charges on the edges of the sample: in presence of PBC, the sample has no edges, thus uniform IP magnetization is more stable.

By repeating the micromagnetic simulations for $K_u = K_{u_0}$ with an extremely refined mesh ($N_{cells} = 1024 \times 1024$), the magnetic skyrmion is stabilized down to $\Delta D = -40\%$. This proves how there is a shift of the minimum i DMI strength for which the magnetic skyrmion is stable, depending on the number of cells. This is because tinier topological solitons could be numerically supported as a consequence of the ℓ_{cell} reduction. A similar effect is obtained in the case of double skyrmion, that will be discussed in Section 2.3.

To establish a link between numerical results and experimental work, it is important to underline how, in the context of voltage tuning of i DMI and interfacial magnetic anisotropy, the electric field at the ferromagnet/oxide interface, established by the applied voltage, should not be higher than $E_b = 1 \text{ V/nm}$, to prevent the dielectric breakdown of the oxide. Taking as reference value for the electric field efficiency on both i DMI and PMA $\beta = 200 \text{ fJ/(Vm)}$ [16], from Equations 1.36 and 1.27, it is possible to estimate the maximum allowed variations of D and K_s (in absolute value), by imposing $E = E_b$. In particular, the computation returns $|\Delta D|_{max} = |\Delta K_s|_{max} = 0.2 \text{ mJ/m}^2$, which corresponds to a percentage of variation $|\Delta D|_{max} = +15\%$ for the i DMI constant and $|\Delta K_u|_{max} = +16\%$ for the uniaxial anisotropy constant.

We see in Figure 2.5 that, starting from D_0 and K_{u_0} as an initial state, one could reach string modification of the skyrmionic bubble size if D is modulated and stronger changes of magnetic texture if K_u is varied. If one wants to modify a skyrmionic bubble by a gate voltage, its annihilation would be very easy by a change of PMA, while i DMI mainly provides a change of diameter. Depending on the required application, one would thus have to independently optimize and tune the initial value of D and K_u and their sensitivities to gate voltage.

Hysteresis loop

To complete the static analysis, the m_z hysteresis loop was drawn out, to understand how the skyrmionic bubble behaves under an applied magnetic field. Practically, this task was accomplished both with the use of `run()` command, by choosing $N_{cells} = 256 \times 256$, and of `minimize()` command, either by setting $N_{cells} = 256 \times 256$ or $N_{cells} = 1024 \times 1024$. While the `run()` command is employed to solve the LLG equation, the command `minimize()` uses the *Steepest Conjugate Gradient Method* to attempt the minimization of the total energy and it should be employed whenever a given magnetization configuration is relatively close to the equilibrium state. A small tilting of $\theta = 1^\circ$ was introduced in the otherwise OP magnetic field vector to avoid possible artefacts generated by the symmetry. From now on, the adjective *up* will be indicative of magnetization oriented along $+z$; the opposite for *down*.

The micromagnetic simulation was initiated by a *down* circle surrounded by *up* magnetization. The magnetic field was then stepped up and down starting from $\mu_0 H_{app} = 0$ mT, to identify the critical positive and negative magnetic field values which cause the conversion of the skyrmionic bubble into an *up* and *down* uniform magnetization states, respectively. After the skyrmionic bubble annihilation above (respectively below) the critical positive (respectively negative) magnetic field value, when the latter is decreased (respectively increased) again, the system is numerically restricted to endure in the uniform magnetization state, because of the energy barrier to be overcome for the re-nucleation of the topological soliton, and the fact that there are no fluctuations in these simulations to overcome it. A second observation regards the two branches of hysteresis curve, descending and ascending, found by starting the simulation from positive and negative magnetic field values, below and above the critical values, respectively. Particularly, these two branches appeared to be degenerate and coincident with the falling branch of the complete magnetization curve, that is the one intercepting the y axis at $H = -H_c$, with H_c coercivity field. Physically, this is equivalent to state the amount of work provided to the system upon the loop, given by the area circumscribed by the the same loop, is zero.

The same behavior is observed by reversing the initial magnetization state, but in this case the rising branch of the full magnetization curve is traced, which cuts the y axis at $H = +H_c$, because of the nucleation of a skyrmion bubble with positive core polarization. Thus, for a given initial state, stepping up or down the Zeeman field is a reversible process, unless the skyrmion is annihilated.

Therefore, the extraction of the full hysteresis curve from the *down* (respectively *up*) circular spot centering an *up* (respectively *down*) square window is actually prevented, because the initial magnetization state breaks the symmetry, favouring the relaxation of the magnetic system into a skyrmionic bubble with negative (respectively positive) core polarization. The extrapolation of the centro-symmetric hysteresis loop, shown in Figure 2.6, is accomplished by merging the branches got with the *down* spot with the ones derived from the complementary initial magnetization state.

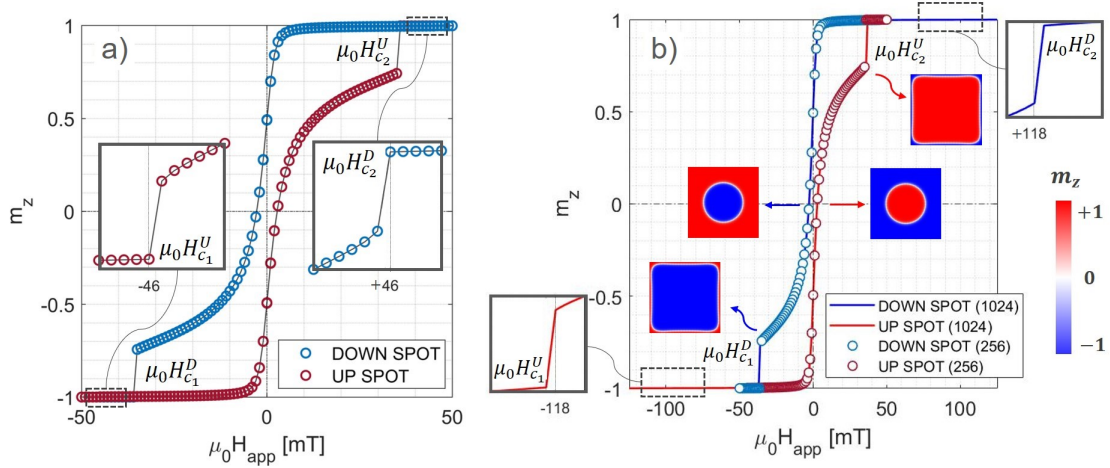


Figure 2.6: Hysteresis curves for Out-Of-Plane (OP) Zeeman field with a) 256×256 and b) 1024×1024 cells, compared to case a). $\mu_0 H_{c_{1,2}}^U$ and $\mu_0 H_{c_{1,2}}^D$ indicate the negative (1) and positive (2) critical magnetic field values for $p = +1$ and $p = -1$ polarities, respectively.

The curves obtained for 256×256 and 1024×1024 cells perfectly retrace each others with the only exception, in the latter case, of increased absolute magnetic field amplitude needed for the skyrmionic bubble to be annihilated. Indeed, in the former case ($N_{cells} = 256 \times 256$), the critical magnetic field values for the the $p = -1$ ($p = +1$) magnetic bubbles – with p core polarity – identified with a step of $\mu_0 H_{step} = +1$ mT, are: $\mu_0 H_{c_1} = -36$ mT (-46 mT) and $\mu_0 H_{c_2} = +46$ mT ($+36$ mT). Instead, concerning the latter case ($N_{cells} = 1024 \times 1024$), owing to the drastic reduction of the unit cell extent, the following values are found: $\mu_0 H_{c_1} = -37$ mT (-118 mT) and $\mu_0 H_{c_2} = +118$ mT ($+37$ mT).

The annihilation field when expanding the skyrmion is similar in both cases. However, the annihilation fields when the skyrmion shrinks show a remarkable divergence. This is because a finer mesh makes it possible to keep a non-homogeneous magnetization over smaller sizes. Figure 2.7 illustrates the size variation in the Zeeman field range ensuring the stabilization of the skyrmionic bubble, for $p = +1$ and $p = -1$ core polarities and $N_{cells} = 1024 \times 1024$.

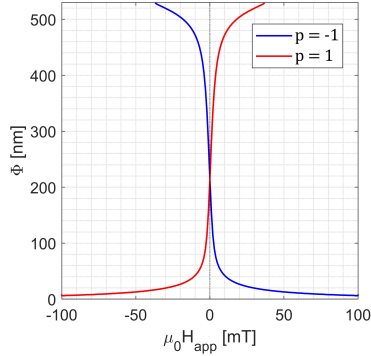


Figure 2.7: Effective diameter for $p = -1$ and $p = +1$ polarities in the magnetic field range of skyrmionic bubble regime ($N_{cells} = 1024 \times 1024$).

In order to validate the results obtained through the command `minimize()`, the hysteresis loop was computed by the use of command `run()` (not shown), limiting to the specific case of *down* circular spot as initial state and $N_{cells} = 256 \times 256$ to abate the simulation time. The result manifests an ultimate superimposition with the curve got by `minimize()`, where the latter command has to be definitively preferred to draw magnetization loop in case of skyrmionic bubble, because of the extremely higher computational efficiency and, at the same time, reliability of the outcomes.

2.2 The skyrmion bubble lattice

Magnetic skyrmions were recently observed in ultra-thin multilayers with Perpendicular Magnetic Anisotropy (PMA). Here, the strong Spin–Orbit Coupling (SOC) and the antisymmetric interfaces (SIA) set up interfacial Dzyaloshinskii–Moriya interaction (*i*DMI), that stabilises Néel magnetic skyrmions with specific chirality. As explained in Chapter 1, Spin–Orbit Torque (SOT) is a novel current induced mechanism employed to write skyrmions and drive their motion in skyrmion-based devices. However, despite SOT being extremely efficient in controlling the skyrmion motion in the case of Néel domain walls, the electric current based nucleation schemes are generally highly power consuming and lead to a crosstalking between writing (nucleating) and driving (moving) operations.

A remarkable headway in fulfilling the requirements of fast, efficient, controllable and local skyrmion creation is represented by the ultra-fast all-optical manipulation of magnetic textures, which also enables a decoupling of the writing and driving operations. Recently, Je et al. (2018) demonstrated the ultra-fast laser heating-induced generation of skyrmion bubble lattice in Ta/FeCoB/TaOx trilayer thin-film [7]. In the following, micromagnetic simulation outcomes obtained for Pt/Co/MgO will be presented.

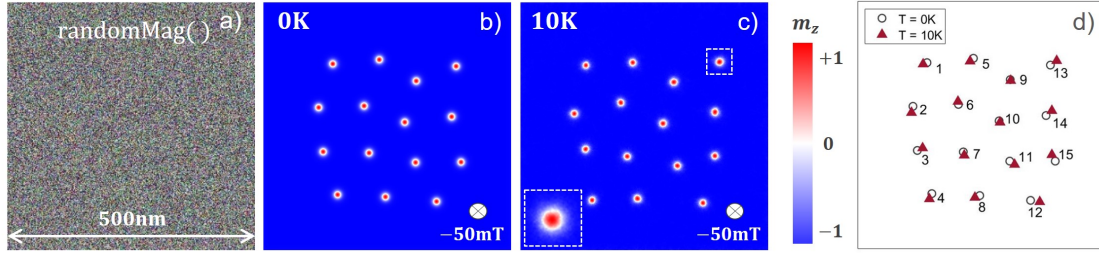


Figure 2.8: a) Initial random magnetization state. b) Skyrmion bubble lattice stabilised at $T = 0$ K for $\mu_0 H_{app} = -50$ mT and no PBC. The color scale is associated to the Out-Of-Plane (OP) magnetization. c) Equilibrium magnetization distribution at $T = 10$ K for $\mu_0 H_{app} = -50$ mT and no PBC, with magnetization in b) taken as initial state. d) Skyrmion bubble label convention. Circular and triangular markers indicate the bubble cores, without and with thermal fluctuation, respectively.

The aftermath of thermal demagnetization is mimicked by prescribing an initial random magnetization state to the simulator, shown in Figure 2.8 a), which would be experimentally obtained if the sample was subjected to a laser pulse. The number of cells is set to $N_{cells} = 512 \times 512$. Under the application of a perpendicular external magnetic field $\mu_0 H_{app} = -50$ mT, after a transient phase, the system reaches a local minimum corresponding to the magnetic skyrmion bubble lattice of Figure 2.8 b), characterized by nearly hexagonal symmetry, in perfect agreement with results of Je et al. (2018) [7]. The skyrmion bubble lattice is made up of fifteen mutually interacting Néel magnetic skyrmions, each one with a topological charge $Q = +1$. The total topological charge is thus equal to $Q = +15$. The magnetization distribution is shown to be robust against thermal fluctuations, as Figure 2.8 c) reveals. In particular, the micromagnetic simulation at non-zero temperature, set to $T = 10$ K, is performed by imposing the stabilised skyrmion bubble lattice of Figure 2.8 b) as initial state. The thermal action just induces a blurring of the domain walls, consequence of the random magnetization fluctuation, combined with a random shift of the magnetic bubble cores. Accordingly, the total topological charge is preserved.

Figure 2.8 d) illustrates the bubble core sites with and without thermal effects and provides the label convention used for modelling the fifteen skyrmions. The induced thermal perturbation also causes a slight overall increase of the skyrmion size: the average diameter, equal to $\Phi_{av} = 12.29$ nm for the unperturbed case, is indeed increased by around 1.6% at $T = 10$ K. The estimated average diameters have an uncertainty of $\epsilon = L/N_{cells,i} = 0.98$ nm. It is only right to highlight how the thermal effect is treated phenomenologically; the input temperature T is just an effective temperature, while the actual thermal field depends also on the saturation magnetization M_s , the numerical mesh, and the damping factor α . Also, one should remember that the LLG equation is valid just close to zero temperature. For all these reasons, considering the overdamping and the presence of interfaces in the sample under analysis, in the context of micromagnetic simulations, the imposed value $T = 10$ K is adequate to model the effect of a thermal field close to room temperature.

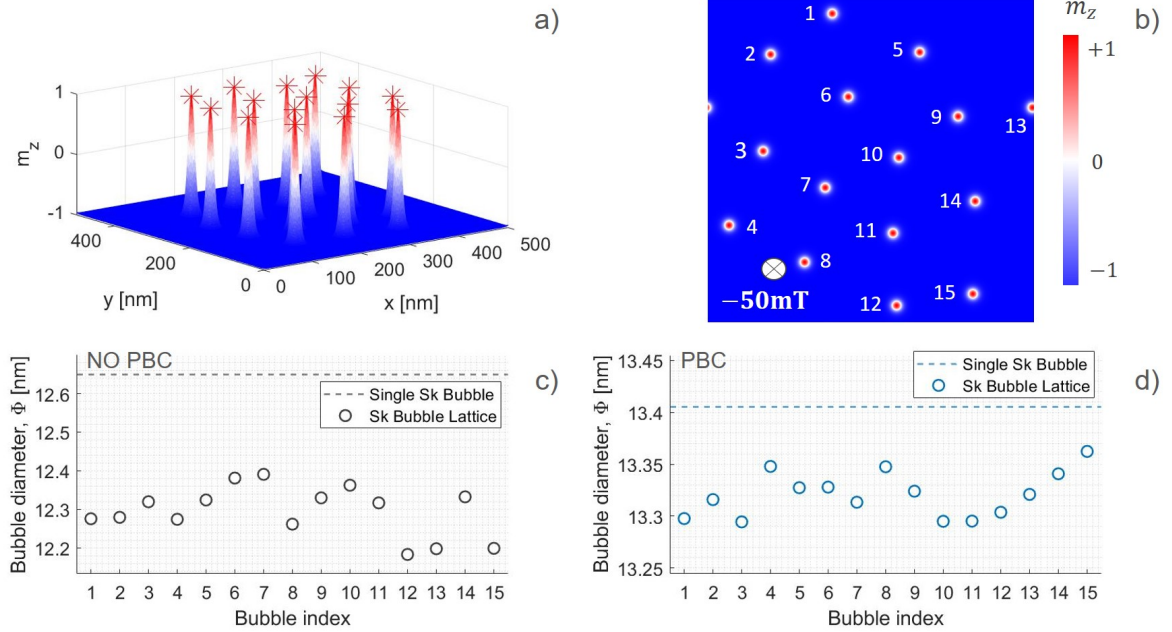


Figure 2.9: a) m_z 3-D plot for the skyrmion bubble lattice at $T = 0$ K and no PBC. b) Skyrmion bubble lattice m_z map stabilised at $T = 0$ K for $\mu_0 H_{app} = -50$ mT and PBC (10, 10, 0). The numbers indicate the label convention. The color scale is associated to the Out-Of-Plane (OP) magnetization. c) Bubble diameter distribution for $T = 0$ K and no PBC compared to the single bubble case ($\Phi = 12.65$ nm). d) Bubble diameter distribution for $T = 0$ K and PBC (10, 10, 0) compared to the single bubble case ($\Phi = 13.41$ nm).

The spatial ordering of the fifteen Néel skyrmions directly results from the long-range dipolar interaction. Indeed, the topological solitons repel each other when associated to the same core polarization p , under the effect of the stray field. The mutual interaction is also evidenced by the reduced average diameter (by around 2.8%) of the magnetic skyrmion bubble belonging to the hexagonal lattice, when compared to the case of having just one at the center of the simulation window ($\Phi = 12.65$ nm), which benefits from an extended magnetic background (Figure 2.7). This latter concept is illustrated in Figures 2.9 c).

Figures 2.9 b) and d) image the effect of sample edge removal: when PBC (10, 10, 0) are imposed, as for the single skyrmionic bubble diameter (increased by around 6.0%) all the topological solitons increase their size (by 8.4% on average). Also, in presence of PBC, owing to the deletion of the repulsive force exerted by the edges, the skyrmionic bubbles spread all over the simulation window, stepping away from each other.

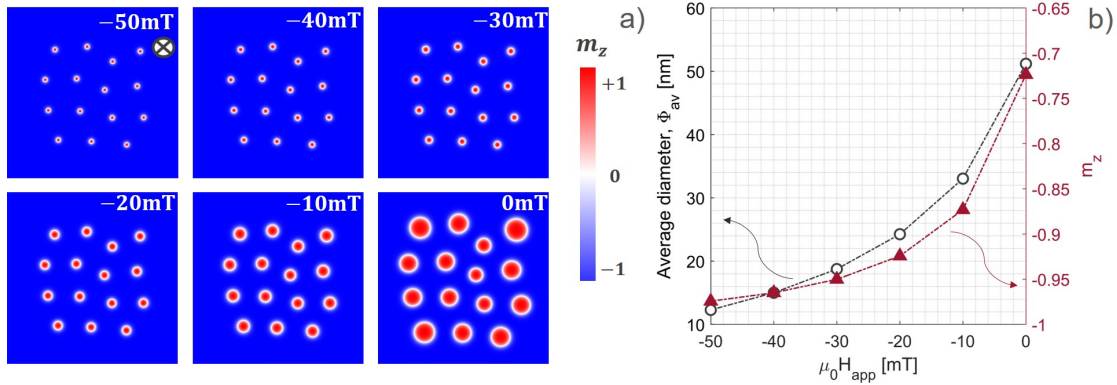


Figure 2.10: a) Evolution of the skyrmion bubble lattice Out-Of-Plane (OP) magnetization m_z with the external magnetic field $\mu_0 H_{app}$, ranging from -50 mT to 0 mT in steps of $+10$ mT. The related data are extracted using the command `relax()` for $T = 0$ K and no PBC. The color scale is associated to the OP magnetization. b) (Corresponding) magnetic bubble average diameter Φ (black curve) and OP magnetization m_z (red curve) as a function of the OP external magnetic field $\mu_0 H_{app}$ for $T = 0$ K and no PBC.

Starting from the stabilised skyrmion bubble lattice at $\mu_0 H_{app} = -50$ mT, by stepping up the Out-Of-Plane (OP) Zeeman field till $\mu_0 H_{app} = 0$ mT, with $\mu_0 H_{step} = +10$ mT, it is possible to observe the expansion of the average skyrmion bubble size, depicted in Figure 2.10 a). Reasonably, this is accompanied by a growth of the total magnetization z component m_z , which becomes even less negative, due to the contribution of the increasingly large bubble magnetic domains, as Figure 2.10 b) shows.

Interestingly, in zero magnetic field conditions, the inner skyrmionic bubbles result evidently squeezed when compared to the outer ones, as a direct consequence of the strengthened demagnetizing field lines ejected from the surrounding bubble magnetic domains.

The objective of the next section, starting from the same thermally demagnetized state, is to illustrate the possibility for the magnetic stack to approach an unusual distinctive stable state, which until now has not had any correspondence in literature. In particular, it will be shown that such stable state, hereinafter called magnetic multidomain state, accomodates a newly disclosed topological excitation, here labeled double skyrmion, which will be thoroughly characterized.

2.3 The magnetic double skyrmion

2.3.1 Introduction and state of the art

The DMI interaction allows the stabilization of a wide range of topological magnetic quasi-particles, which are protected from collapsing into the background magnetization state, including skyrmions, anti-skyrmions, skyrmioniums, merons or, more in general, skyrmion bags [3]. Among them, a new kind of 1-D topologically protected excitation, namely the domain wall skyrmion (*DWSk*), has latterly entered the game of spintronics, being the subject of manifold recent publications found in literature. The domain wall skyrmion, as the name suggests, represents a $2 - \pi$ rotation of the In-Plane (IP) magnetization components within a Néel domain wall [49], stabilised mainly by dipolar energy, as shown in Figure 2.11 d). As a matter of fact, the local twist of magnetization, even though extremely confined, may be regarded as a one-dimensional $2 - \pi$ domain wall, which aids looping the magnetic field flux lines. Both such circumscribed 1-D skyrmion and 2-D skyrmions can be minimally defined as having an integer topological charge, that can be equal to $Q = \pm 1$.

Something that should be mentioned is that the direction of magnetization rotation for 1-D skyrmion, in contrast to 2-D skyrmion, is not dictated by *i*DMI. Furthermore, the core of the 1-D skyrmion has a magnetization orientation which opposes the chirality imposed by the *i*DMI sign. *DWSk* is comparable to $2 - \pi$ Vertical Bloch Line (VBL) coming about in Bloch instead of Néel domain walls and having an integer topological charge of $Q = \pm 1$ [50]. Schematics of $1 - \pi$ and $n - \pi$ VBL, homochiral Néel DW and *DWSk* are provided in Figures 2.11 a) and b). Domain wall skyrmions may pave the way for the realization of novel efficient spintronics [51]. Indeed, they have the great advantage of being restricted to move within the magnetic domain wall, which serves as a track, being therefore insensitive to edge pinning.

For the very same reason, they are prevented to drift in undesired directions as with 2-D skyrmions (via SkHE) [50].

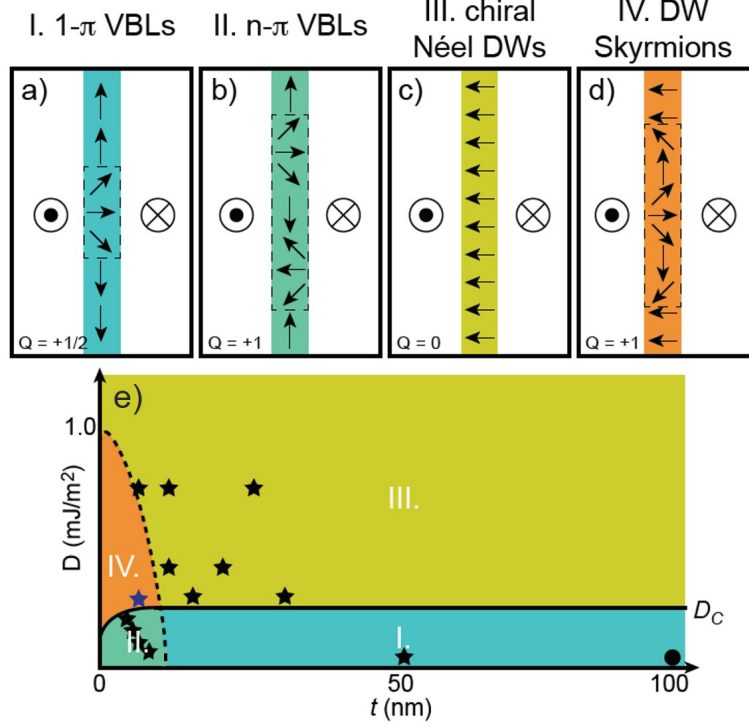


Figure 2.11: Schematics depicting the internal magnetization of a) $1 - \pi$ Vertical Bloch Line, b) $n - \pi$ Vertical Bloch Line, c) chiral Néel domain wall, and d) domain wall skyrmion. e) Predicted phase diagram depicting conditions where the aforementioned magnetic textures can be expected to be observed with respect to DMI strength and film thickness in Pt/Co/Ni/Ir samples [50].

Theories without a Skyrme term can provide fixed size skyrmions located on a domain wall. Jennings and Sutcliffe (2013) [52] numerically investigated for the first time the $DWSk$ dynamics in a relativistic $(2 + 1)$ -dimensional (planar) theory, to prove both the skyrmion stability and the multi-skyrmion scattering. In the specific case of chiral magnets, the Skyrme term is replaced by Dzyaloshinskii-Moriya Interaction (DMI), accounting for the nucleation of Néel magnetic skyrmions. Instead, in the present case, a static single skyrmion was numerically constructed on a domain wall in $(2 + 1)$ -dimensions by including in the total energy an additional in-plane anisotropy contribution and by imposing suitable boundary conditions to the function $\theta(y)$. Here, θ represents the angle between the generic unit vector \mathbf{m} and the z axis, outward normal to the simulation plane, while y is the transverse axis. Figure 2.12 highlights the in-plane winding structure discrepancies, arising when a standard Sk and a $DWSk$ are compared.

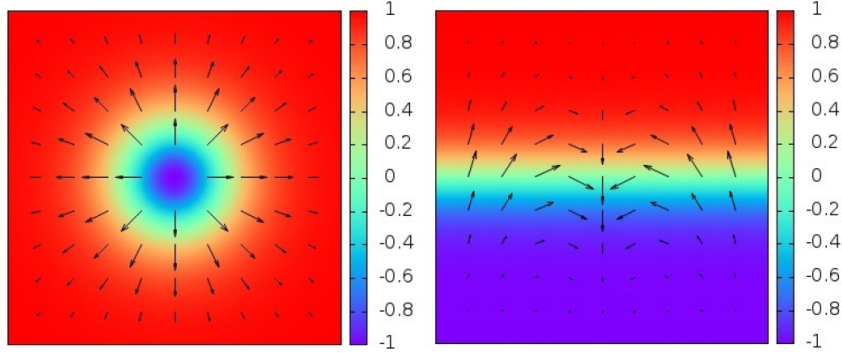


Figure 2.12: xy plane winding structure for conventional skyrmion (left) and domain wall skyrmion (right). The colour represents the value of m_3 and the arrow indicates the amplitude and direction of the two-component vector (m_1, m_2) [52].

In particular, the colour indicates the amplitude of m_3 , while the arrows represent the magnetization vector projected in the xy plane. The origin of the plane is placed at the center of the simulation window. Focusing on the $DWSk$ (right), by aligning along y lines, m_3 exhibits a monotonic increase from -1 to $+1$ and the vector (m_1, m_2) has a constant direction; x lines instead reveals a constant m_3 vector which implies constant magnitude for (m_1, m_2) vector that at, the same time, rotates through one revolution, being asymptotically equal to $(0, +1)$ at the x line endpoints. It is quite evident how, although the winding structure of the $DWSk$ appears quite dissimilar from that of the conventional skyrmion, again any point of the unit sphere can be covered by the space distribution of the magnetization vector. In this work [52], the $DWSk$ is shown to be resilient to a wiggle introduced in the domain wall, providing a strong numerical evidence of its stability. Also, a $DWSk$, boosted with an initial velocity towards a second identical soliton on the same domain wall, is demonstrated to experience a repulsive force. Last but not least, a more exotic phenomenon is presented, where DW skyrmions survive the process in which two half-walls straighten into a single wall, to subsequently move apart along the remaining straight wall due to their repulsive interaction. This is a further evidence in support of their stability.

Atomistic simulation results obtained by Lepadatu (2020) [49] show how, together with skyrmions and skyrmioniums, transient domain wall skyrmions can emerge in systems with structural inversion asymmetry (SIA), both antiferromagnetic (AFM) and ferromagnetic (FM), during magnetization recovery processes after material irradiation through an ultra-fast laser pulse. In spite of the creation of large number of $DWSk$ during the skyrmion creation stage, they are not found in the relaxed state due to both quick thermal decay and pair annihilation with opposite topological charge skyrmions.

Magnetic domain wall skyrmions were experimentally observed for the first time by Li et al. (2020) [50] using Lorentz Transmission Electron Microscopy (LTEM). The elusivity of prior experimental evidences is likely attributable to the small window of DMI strength and film thickness required for their stabilization [50] and, as previously shown, due to rapid thermal activated collapse [49]. The experimental inspection was carried out in an asymmetric multi-layer system based on $(\text{Pt}/[\text{Co}/\text{Ni}]_M/\text{Ir})_N$, where a reduction in M accounts for an enhanced interfacial DMI from the Pt/Co and the Ni/Ir interfaces, while N controls the optimal total film thickness for the nucleation of $DW\text{Sk}$. A qualitative magnetic phase diagram, result of a systematic study of this multi-layer system, depicts the region where $DW\text{Sk}$ are theoretically expected to be observed and were actually observed by LTEM (Figure 2.11 e)). Such a region corresponds to high DMI, increased above the critical value to stabilize chiral Néel DW, and low film thickness, where t is small enough to suppress the formation of hybrid DW, that are DW having a non-constant structure along the direction perpendicular to the film.

Domain wall skyrmions were also experimentally disclosed by Nagase et al. (2020) [51], again by using LTEM. In this study, a direct observation of these topological defects in cubic chiral magnetic thin-films of the type $\text{Co}_{8.5}\text{Zn}_{7.5}\text{Mn}_4$ (110), with thickness of $t \sim 50$ nm, was reported. More in detail, under the application of out-of-plane magnetic field, $DW\text{Sk}$ appear as pairing up with the conventional DW. In addition, micromagnetic simulation results suggest that $DW\text{Sk}$ can largely nucleate in cubic chiral magnet (110) thin-films with large magnetocrystalline anisotropy.

Je (2020) [4] numerically studied the dynamic process of the skyrmion nucleation, which is still object of the study, carrying out micromagnetic simulations using the Object Oriented MicroMagnetic Framework (OOMMF) public code with DMI package tool. In this work, the simulation parameters correspond to a 0.3 nm thick Ta/FeCoB/TaO_x thin-film. The transition of the sample into the skyrmionic state can be thermally activated, for example by shining a laser beam to exploit localized heating, so that to assist the system in overcoming certain barriers in the energy landscape to reach the magnetic skyrmion energy well. However, to switch between the single/multiple domain and skyrmionic states, the latter associated to a different total Q , requires a change in the topological charge, which is mediated by the emergence and annihilation of 1-D skyrmions, modifying domain wall morphology. In particular, for $D > 0$, Head-to-Head (H2H) and Tail-to-Tail (T2T) 1-D skyrmions – hereinafter called *anti-kink* and *kink* and characterized by topological charges $Q = -1$ and $Q = +1$ respectively – annihilate in pairs. Such spin textures, illustrated in Figure 2.13, are visually distinguishable from one another by the induced domain wall convex and concave profiles respectively, as Figure 2.14 f) shows (continuous line circles).

The localized bending of the domain wall is indicative of the 1-D skyrmion exceeding cost in terms of antisymmetric exchange energy [8]. As a matter of fact, in order to keep the In-Plane (IP) magnetization vector transverse to the domain wall for the maximum possible extent, to reduce at minimum its Bloch-like nature – disfavoured by the Dzyaloshinskii-Moriya Interaction – a narrow characteristic curvature is induced. In this study [4], it is reported the dominant role, played by 1-D skyrmions appearing in flat and circular domain walls, in the topology evolution of skyrmion generation. The system is initialized through a random magnetization state in the center of the simulation window, to mimic the nucleation of magnetic skyrmions from a thermally demagnetized region. The magnetization relaxation is induced in presence of an out-of-plane magnetic field of $\mu_0 H_{app} = +8 \text{ mT}$. The unitary discrete jumps of the topological charge revealed in the course of transient time are correlated to the annihilation of the topological defects embedded in the Néel domain walls.

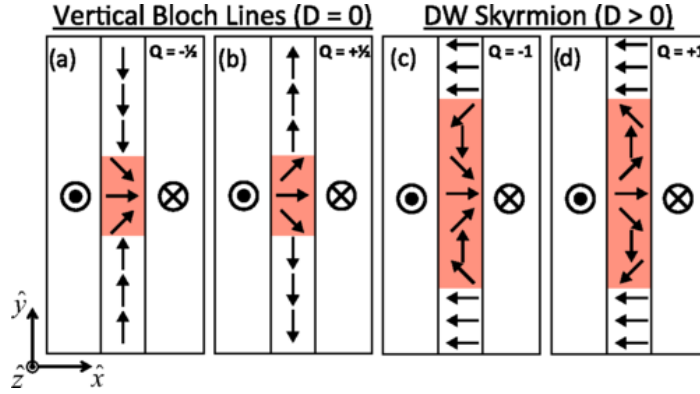


Figure 2.13: Schematics depicting the internal magnetization of a), b) $1 - \pi$ Vertical Bloch Lines of topological charge $Q = \mp 1/2$ for zero DMI and c), d) domain wall skyrmions of topological charges $Q = \mp 1$, Head-to-Head (H2H) and Tail-to-Tail (T2T) respectively, for positive DMI [8].

Chiral skyrmionic bubbles, embodying one or multiple 1-D skyrmions inside the otherwise homochiral Néel domain wall, have been numerically foretold as solitonic solutions [3]; nevertheless, apart from the work of Je (2020) [4], the dipolar interaction, which is potentially the primary reason accounting for the stability of such narrow magnetization knots, was not hold in consideration. The main contribution to the literature of the present thesis work, inclusive of dipolar energy term, is the evidence of the stability, after magnetization regaining, of a newfound particle-like excitation, here named double skyrmion (*DSk*), which likely survives concomitantly with other non-trivial magnetic spin textures. Hereafter the main micromagnetic simulation results centered on the double skyrmion will be presented, with the goal of investigating its distinctive static and dynamic properties when compared to a conventional skyrmionic bubble of well-defined chirality.

2.3.2 Numerical characterization results

The multidomain state

In this thesis work it is numerically evidenced that magnetic *kinks* can be stabilized, after magnetization recovery process, in both flat Néel domain walls and, anew, in the domain wall of Néel skyrmionic bubbles. To distinguish between these two peculiar cases, they are hereafter referred to as domain wall skyrmion (*DWsk*) or *kink*, and double skyrmion (*DSk*), respectively. As already stated, a random magnetization state imposed as initial magnetic configuration, depicted in Figure 2.14 a), allows to mimic the effect of material irradiation through an ultra-fast laser pulse, which causes the ferromagnetic layer to be fully demagnetized in short-time scale, as a direct consequence of the induced thermal heating ($T > T_C$, the Curie temperature). When the external magnetic field is set to zero (by contrast to the previously treated skyrmion bubble lattice), the initial demagnetized state, after several relaxation steps – as detailed in the following – numerically converges towards the (here called) magnetic multidomain state, illustrated in Figure 2.14 c). The magnetic configuration reveals the simultaneous presence of two Néel domain walls, the top one entrapping two *DWsk* ($2 \times$ quasi-particles of $Q = +1$), three conventional Néel skyrmionic bubbles ($3 \times$ quasi-particles of $Q = +1$) and, last but not least, two *DSk* ($2 \times$ quasi-particles of $Q = +2$), superposition of a Néel skyrmionic bubble and a *DWsk*. The total topological charge of the thin-film is thus expected to be $Q = +9$, a value which is fairly close to the numerical one, equal to $Q_{num} \sim +8.75$. The non-integer value of the numerical topological charge can be explained considering the finite size of the sample, the localization of magnetic *kinks* in nearly flat non-closed domain walls of finite extent, abruptly cut by the sample edges, and the space discretization in square unit cells. It is important to emphasise that the essential prerequisite to make magnetic *kinks* steadily visible at simulation level is to set an extremely refined mesh, which enhances the resolution above the characteristic length of these new topological structures. Here, the size of the unit cell, equal to $\ell_{cell} = 0.49$ nm, is fairly smaller than both the exchange length ($\Delta_d = 3.43$ nm) and the Bloch length ($\Delta_u = 3.55$ nm).

For a better understanding of the adopted technique, it is possible to follow the implemented steps in the same Figure 2.14. In detail, the random magnetization state of Figure 2.14 a) was first relaxed (`relax()` command) by imposing $N_{cells} = 1024 \times 1024$, so that to keep the `MaxAngle` value within specifications, as shown in Figure 2.14 b). Afterwards, the relaxed magnetic state, featured by several *kinks* ($Q = +1$) and *anti-kinks* ($Q = -1$) and a total topological charge $Q_{num} \sim +6.5$, was run (`run()` command) to properly study the dynamics of the topological charge evolution.

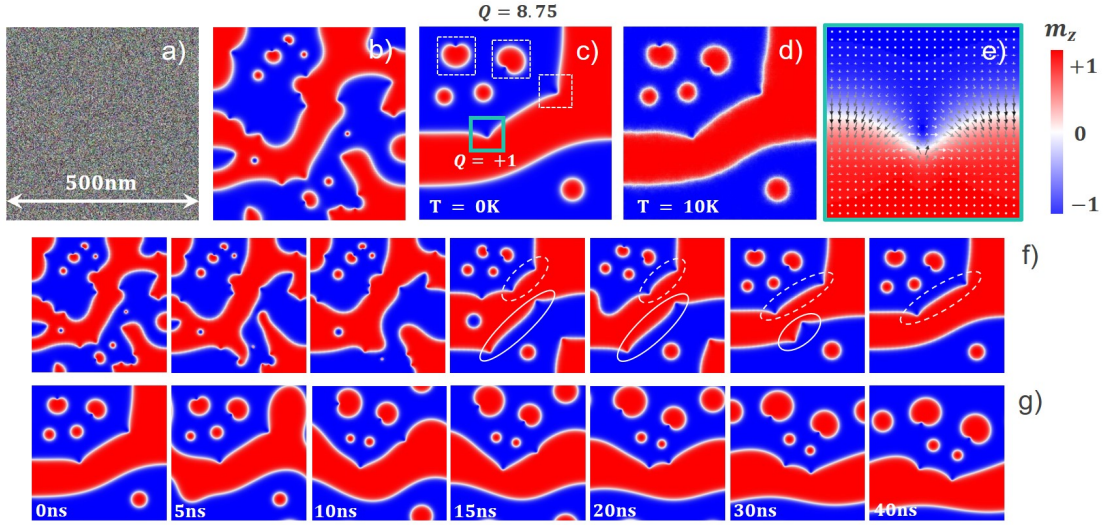


Figure 2.14: a) Initial random magnetization state. b) Relaxed magnetization state at $T = 0$ K (`relax()` command). c) Multidomain equilibrium state at $T = 0$ K (`run()` command). d) Multidomain state at $T = +10$ K after 20 ns of integration. e) Zoom on domain wall skyrmion accommodated by a left-handed (LH) Néel DW. f) Evolution of magnetization with integration time starting from the state obtained with `relax()` command of Figure b). g) CIP-SOT driven motion for $J_{app} = +5 \times 10^{10}$ A/m² injected parallel to x axis and PBC (1, 1, 0). The color scale is associated to the Out-Of-Plane (OP) magnetization. The applied magnetic field is zero.

In the course of the magnetization progression towards the local energy minimum of Figure 2.14 f), the attractive force between the two oppositely charged *DWSk* (encircled with continuous line), sited in correspondence of the bottom domain wall, is revealed. Indeed, the co-located *kink* ($Q = +1$) and *anti-kink* ($Q = -1$), visually discernable by the concave and convex profiles respectively, annihilated after having approached each other, resulting in a flat Néel domain wall. This finding is in agreement with result of Jennings and Sutcliffe (2013) [52]. The antithetical case, i.e. the repulsive force between equally charged 1-D skyrmions (encircled with dashed line), is also disclosed. This latter numerical evidence is confirmed by simulating the CIP-SOT driven motion of the equilibrium multidomain state, with $J_{app} = 5 \times 10^{10}$ A/m² oriented along x axis and PBC (1, 1, 0), as Figure 2.14 g) shows: particularly, the two *kinks* on the top domain wall start to draw closer to one another at first, to retreat after having reached a minimum critical distance, alongside the inversion of the domain wall slope.

Resilience of 1-D skyrmions to temperature and material inhomogeneity

A further inspection of the robustness of such topological objects demanded to check both the thermal stability and the resilience to granular structure. To this purpose, the equilibrium magnetic configuration of Figure 2.14 c) was imposed as initial state for micromagnetic simulations. The equilibrium magnetization distribution at non-zero temperature was then calculated from the numerical solution of stochastic Landau-Lifshitz Gilbert (sLLG) equation [53], by imposing an effective temperature of $T = 10$ K. As displayed in Figure 2.14 d), the effect of thermal perturbation is just that of blurring the contour of the domain walls, fact that numerically predicts the thermal stability at room temperature.

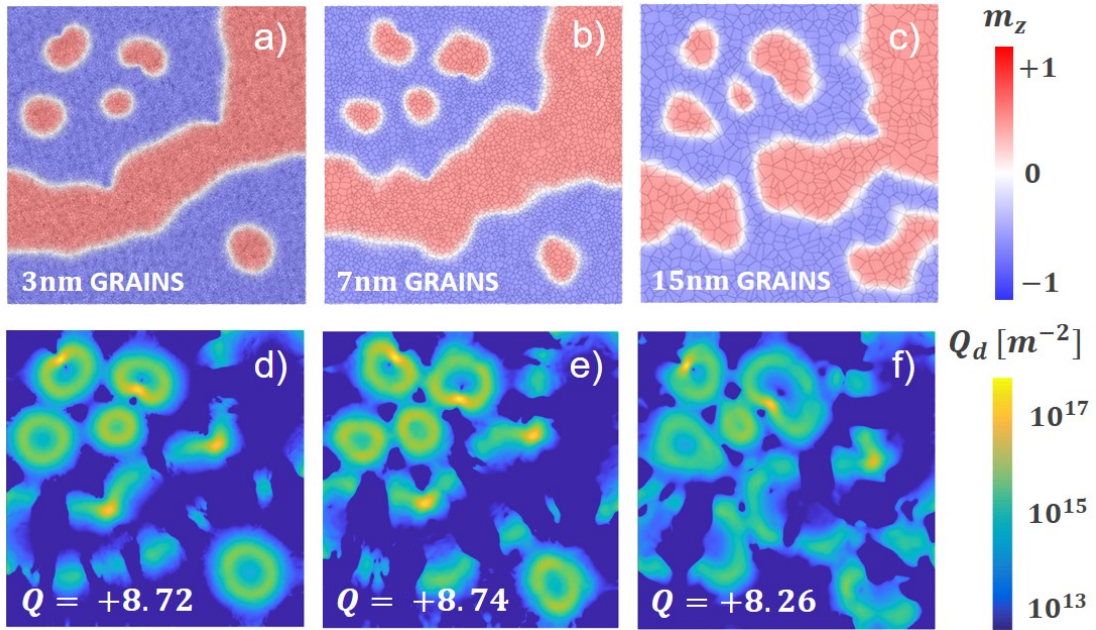


Figure 2.15: Out-Of-Plane (OP) equilibrium magnetization distribution superposed by the cartography of the granular structure for a) 3 nm, b) 7 nm and c) 15 nm grains, with normally distributed uniaxial magnetic anisotropy ($\sigma/\mu = 10\%$) and 10% exchange coupling reduction at the grain boundaries. From d) to e), corresponding maps of topological charge density with total integrated Q .

Thereafter, in order to model real polycrystalline materials, composed of many crystallites of variable size and orientation, grain-like regions were specified using Voronoi tessellation [37]. For the same purpose, a normal distribution of magnetic anisotropy K_u , with standard deviation to mean value equal to $\sigma/\mu = 10\%$, and an exchange coupling reduction of 10% between the grains, were set. Particularly, three case studies were treated, that are 3 nm, 7 nm and 15 nm grains.

Two main effects are observed, illustrated in Figure 2.15: first, the space reorientation of double skyrmions driven by the anisotropy fluctuation; second, the appearance of irregularities in the domain wall contour – more and more evidenced by the increase of grain size – which makes it difficult to visually discern between magnetic *kinks* and non magnetic warps, the latter upshot of the grains, at experimental level. However, what really matters is the survival of the topologically non-trivial magnetic *kinks* even in the presence of granularity. This observation directly translates into the conservation of the total topological charge, which is reduced by nearly one just in the worst case of 15 nm grains, where the red middle magnetic domain is splitted into two, provoking the disappearance of a *DWsk*. This can be also intuited by specifically looking at the maps of topological charge density Q_d of Figures 2.15 d), e), f): the topological charge density is indeed expected to be highly concentrated in the specific locations of ultra-confined 1-D skyrmions, fact that is confirmed by the presence of the yellow spots centered in correspondence with local *kinks* of Figures 2.15 a), b), c).

Having outlined the procedure to observe the double skyrmion and provided evidences of its stability, from here on the attention will be focused onto the profiling of the static and dynamic behavior of such kind of topological excitation, wholly compared to the case of homochiral skyrmionic bubble.

Static properties

With the aim of analyzing the static response of the double skyrmion (*Dsk*) and making a comparison with the conventional skyrmionic bubble (*Sk*), the corresponding total energy and effective diameter were extracted by varying independently the strength of the *i*DMI coefficient D and the amplitude of the out-of-plane Zeeman field $\mu_0 H_{app}$, for circular and square geometries, respectively.

In this context, owing to the *kink*-induced breaking of the spherical symmetry, the *Dsk* effective diameter and, for consistency, that of the *Sk* are numerically estimated according to the following algorithm:

- evaluation of the number of unit cells $N_{cells}^{m_z > 0}$ where $m_z > 0$;
- computation of the effective area where the condition $m_z > 0$ is satisfied, $A = N_{cells}^{m_z > 0} \ell_x \ell_y$, ℓ_x and ℓ_y being the unit cell lateral dimensions;
- calculation of the corresponding effective diameter, $\Phi = 2\sqrt{A/\pi}$.

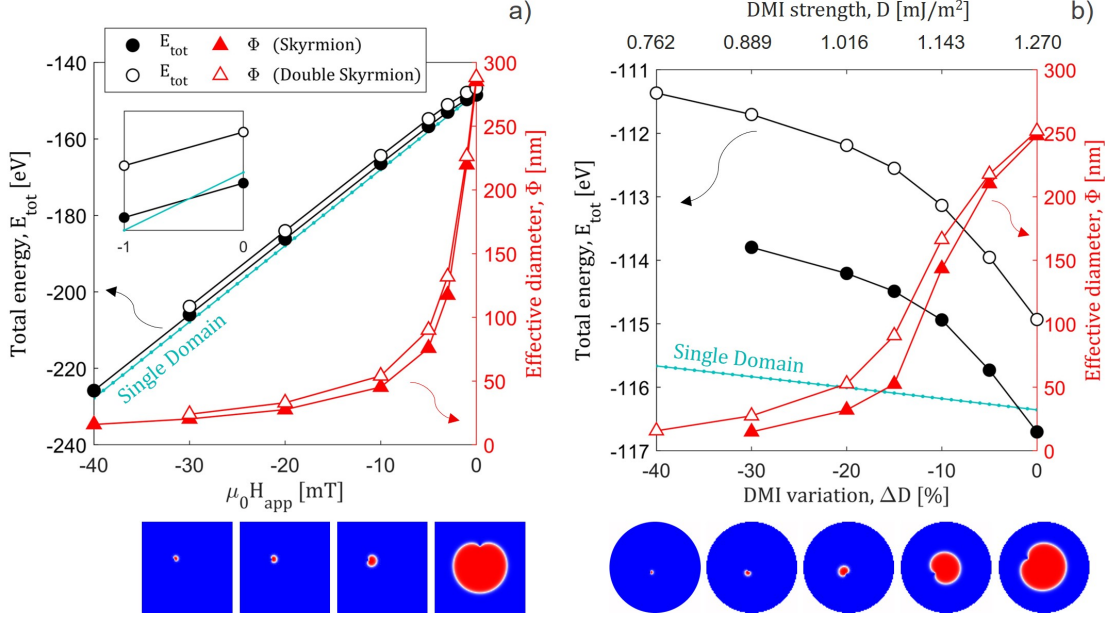


Figure 2.16: Comparison of double skyrmion and skyrmion total energy E_{tot} (black curve) and effective diameter Φ (red curve) characteristic variations vs. a) out-of-plane Zeeman field $\mu_0 H_{app}$ (square geometry) and b) i DMI coefficient D (circular geometry). The applied magnetic field in b) is zero. The pale blue lines represent the total energy distribution for the single domain state.

As evidenced by Figure 2.16, the overall behavior, common to the two topological excitations, is the linear decrease (respectively quadratic-like increase) of the total energy with the increase of the Zeeman field amplitude (respectively i DMI strength). However, the DSk energy exceeds the Sk one for all the explored conditions. This evinces how the DSk is a stable state that the system can visit, being then impeded to reach the Sk energy minimum because of the interposing energy barrier. Indeed, the DSk appears to be fostered just by the dipolar energy, while all the other contributions overstep the Sk case. Reasonably, this is attributable to the DSk larger effective area, better balancing the extent of the magnetic background, and, to a lesser extent, to the presence of the local magnetic whirl which, albeit extremely confined, helps balancing the magnetic volume charges in the Néel domain wall.

The graphs also point out that the size of the DSk , similarly to skyrmionic bubble, is extremely responsive to both control parameter, i.e. magnetic field, and internal material parameters, such as the strength of the i DMI. Upon toughening the external magnetic field, aligned parallel to the background magnetization (blue region), the effective diameter undergoes a rapid shrinkage.

However, there exists a critical magnetic field value $\mu_0 H_c = -40$ mT, identified with a resolution of -10 mT, below which the perimeter of the magnetic bubble becomes so short to no longer be able to withstand the equivalent tensile stress in the domain wall introduced by the magnetic *kink*, which is thus annihilated. The *DSk* is thus transformed into a conventional *Sk*. Put differently, the larger the strength of the applied negative Zeeman field, the lower the height of the energy barrier in between the *DSk* and *Sk* energy minima. The same contraction of the double skyrmion, observed for negative magnetic field values, occurs when the *i*DMI coefficient is reduced. Reasonably, due to reduction of *i*DMI, the energy of Néel domain wall is increased, which increases the total energy, as seen in Figure 2.16 b). Notably, the *DSk* exhibits an enhanced resilience to *i*DMI reduction, inspected in steps of 10% of variation, with respect to *Sk*. This is attributable to the *DSk* stronger topological protection ($Q = +2$ vs. $Q = +1$) and the likely higher associated energy barrier: indeed, while the *Sk* state is converted into the single domain state at $\Delta D = -40\%$, as displayed by the abrupt energy jump, the *DSk* vanishes at $\Delta D = -50\%$.

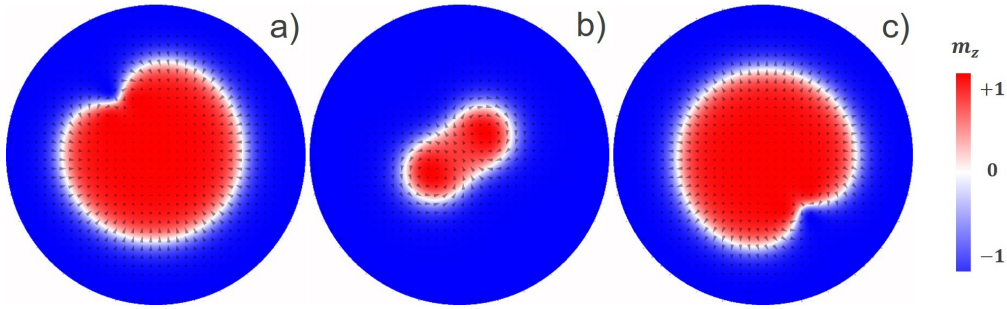


Figure 2.17: Equilibrium magnetization states at different *i*DMI for $\mu_0 H_{app} = 0$ mT, $K_u = 1.27$ MJ/m³ and circular geometry. a) Superposition of LH *Sk* bubble and T2T *DWSk* stabilised for $D = +0.5$ mJ/m². b) Bloch skyrmionic bubble with two $1-\pi$ VBL stabilised for $D = +0$ mJ/m². c) Superposition of RH *Sk* and H2H *DWSk* stabilised for $D = -0.5$ mJ/m². The color scale is associated to the Out-Of-Plane (OP) magnetization.

At present, it is possible to switch *i*DMI sign with a gate voltage (Fillion C. et al., private communication). It is thus interesting to check how a skyrmion and a double skyrmion would evolve with a continuous decrease of *i*DMI coefficient, even going to *i*DMI sign inversion. Indeed, the achievability of *D* sign inversion, where the *i*DMI sign controls the chirality of the skyrmionic bubble carrying the *kink*, would be another evidence of the stability of *DSk*. This study was carried out in collaboration with C. Fillion. In order to accomplish the numerical experiment without the support of an external magnetic field, the Quality Factor of the system was reduced to $Q = K_u/K_d \sim 1.002$, by imposing $K_u = 1.27$ MJ/m³.

In this way, the system approaches the Out-Of-Plane (OP) to In-Plane (IP) transition region and the cost of the domain wall, modelled by Equation 2.1, is thus compensated. This allows to stabilize Bloch skyrmionic bubble in absence of i DMI [54]. As a matter of fact, the PMA and the i DMI represent two distinguished phenomena triggered by similar physical reasons. Accordingly, to account for the reduction of K_u , the initial i DMI strength was downsized to $D = +0.5 \text{ mJ/m}^2$. Larger values of D would in fact lead to spin spiral state (negative σ_w). Figure 2.17 shows the DSk equilibrium states for various i DMI values. The initial state chosen to carry out the micromagnetic simulation is the left-handed (LH) Néel skyrmionic bubble with a tail-to-tail (T2T) *kink* in its domain wall, stabilized for circular geometry, in absence of Zeeman field and PBC, as shown in Figure 2.17 a). The i DMI was then stepped down by imposing $D_{step} = 0.01 \text{ mJ/m}^2$ and, one step at a time, the system was stabilised through the command `minimize()`. At the value $D = 0 \text{ J/m}^2$, a Bloch-like topological soliton with two diametrically opposite $1 - \pi$ VBL is stabilized, preserving the total topological charge ($Q = +2$). The two $1 - \pi$ VBL are featured by divergent directions of rotation. This topological excitation appears to be composed by two mutually dependent Bloch skyrmions of opposite whirling directions that are stuck together (sharing a part of the DW). Afterwards, when the D coefficient is further changing towards negative values up to $D = -0.5 \text{ mJ/m}^2$, the Bloch-like topological soliton is turned again into a double skyrmion, but of opposite chirality (with respect to positive D case), that is right-handed (RH), with a head-to-head (H2H) magnetic *kink*. The restoration of the Néel domain wall occurs through the expansion of the $1 - \pi$ VBL having the right attribute, i.e. H2H, at the expense of the other, which is annihilated. It is interesting to note how, with no i DMI, the local arching of the domain wall in correspondence of the $1 - \pi$ VBL is significantly reduced, if compared to the double skyrmion case. This is not surprising because the curvature of $DWSk$ is due to strength of i DMI [8]. In support of this, it is observed that such distinctive feature, in close proximity to the *kink*, becomes clearly even more pronounced when the i DMI is strengthened, confirming its central role in establishing such character. In order to validate the numerical experiment, the same was conducted again through the command `run()` by reducing the step value to $D_{step} = 0.1 \text{ mJ/m}^2$, to face the increased computational cost. The only spotted difference is the space re-orientation of the DSk in the course of the simulation. The process is demonstrated to be reversible and the trace and retrace steps energetically degenerated.

Influence of boundary conditions and sample shape

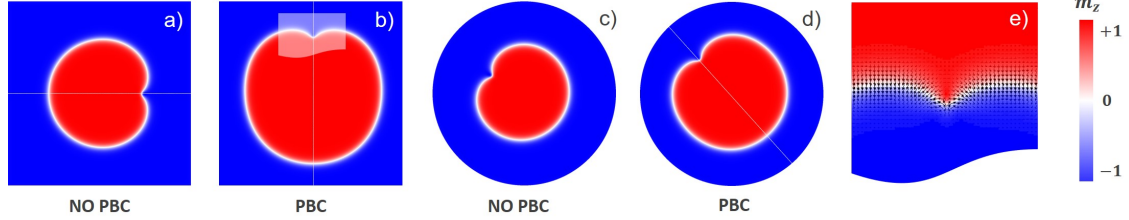


Figure 2.18: Impact of dipolar field on double skyrmion size and orientation. In detail, Out-Of-Plane (OP) equilibrium magnetization distribution with no applied magnetic field for a), b) square geometry and c), d) circular geometry, without and with Periodic Boundary Conditions (PBC), respectively. The white dashed line indicates the *kink* axis. e) Zoom on the 1-D skyrmion.

By tuning the shape of the sample and the Periodic Boundary Conditions (PBC), it is possible to control the isotropicity of the magnetic environment surrounding the double skyrmion, in such a way to investigate the impact of the magnetic field flux lines radiated by the magnetic background on the space orientation of the *kink*. With reference to Figure 2.18, it is possible to observe that, in case of square geometry and no PBC, the anisotropicity of the magnetic environment drives the magnetic *kink* to align along either the x or y axis, energetically equivalent. This is verified independently on the initial magnetization state. Indeed, differently from the conventional skyrmion, ideally enclosed by a perfectly circular domain wall, the double skyrmion local bending introduces a radial dependence of its domain wall position. Upon this, the *DSk* shortest axis is obtained by a transverse sectional plane cutting through the topological structure along the magnetic *kink* axis. This axis, minimizing the linear extent of the inner magnetic domain, lines up with the direction along which the extension of the outer magnetic domain, oppositely magnetized, is minimized as well. The same characteristic behavior is observed in presence of circular shape with PBC, where the inherent geometrical isotropicity of the simulation domain is disrupted upon imposing PBC, because of the identical copies of the sample contacting the magnetic background along x and y axes. Again, the *kink* re-orient itself so that to align along one of the isoenergetic axes minimizing the radiated dipolar field, now matching the main diagonals of the squared simulation region. As expected, for the circular sample, when PBC are removed, the magnetic *kink* randomly orients in space, attesting the energy equivalence of all the angular positions. Reasonably, micromagnetic simulation results reveal that the influence of the sample size and geometry lose their effectiveness when the *DSk* area is reduced, as shown on the bottom panels of Figure 2.16, where the *kink* orientation (in presence of negative Zeeman field) is now random.

Dynamic properties under current

The dynamic behavior of the double skyrmion was outlined by inspecting the Current In-Plane Spin–Orbit Torque (CIP-SOT) and Spin Transfer Torque (CIP-STT) driven dynamics. It is well known that a conventional skyrmionic bubble (Sk), when subjected to CIP-SOT, reaches a steady-state motion, with a characteristic Skyrmion Hall Angle (SkHA) in between the velocity and the current density vectors, as detailed in Section 1.5.2. This phenomenon is illustrated in Figure 2.19 a), where the white contour portraits the initial magnetization state.

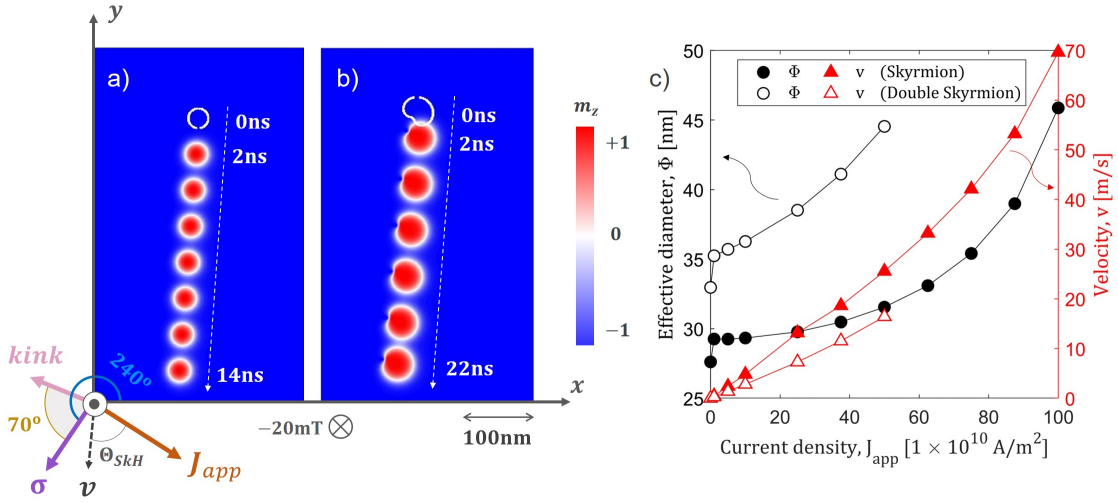


Figure 2.19: Illustration of CIP-SOT driven motion of a) skyrmionic bubble and b) double skyrmion, for $J_{app} = 50 \times 10^{10}$ A/m 2 and $\mu_0 H_{app} = -20$ mT applied perpendicular to the plane. The color scale refers to Out-Of-Plane (OP) magnetization. c) Comparison of effective diameter Φ (black line) and velocity v (red line) vs. CIP-SOT current density J_{app} characteristics for skyrmionic bubble and double skyrmion, with $\mu_0 H_{app} = -20$ mT applied perpendicular to the plane. The white contours in a) and b) represent the initial magnetization states.

In particular, for an applied current density $J_{app} = 50 \times 10^{10}$ A/m 2 , injected in the HM layer so as to induce an HM/FM interface spin polarization $\theta_\sigma = 240^\circ$ (with respect to x axis), the Sk follows a trajectory modified by the SkHA, numerically estimated to be $\Theta_{SkH} = 64.45^\circ$. The end of the track is reached in around 14 ns. Figure 2.19 b) sets out the double skyrmion (DSk) CIP-SOT driven motion, while maintaining unchanged the injection conditions. On the whole, the DSk dynamics comes very close to the Sk behavior, with the exception of four main discrepancies. In detail, the DSk , reaching the end of the track in nearly 22 ns, appears to be slower than conventional Sk . This may be due to the DSk larger effective area, when subjected to the same torque magnitude, as shown in Figure 2.19 c).

Also, its numerical SkHA, measured to be $\Theta_{SkH} = 65.74^\circ$, results slightly bigger, likely due to the greater topological charge. To better explore this phenomenon, the analytical SkHA was estimated according to the following equation, as detailed in Section 1.5.2:

$$\Theta_{SkH} = \frac{G}{\alpha D} \quad (2.3)$$

where α is the Gilbert damping coefficient.

Particularly, the terms G and D were computed by implementing the following analytical models for the dissipative matrix \mathbf{D} and the gyromagnetic vector $\mathbf{G} = G \hat{\mathbf{z}}$ [47]:

$$G = -\frac{M_s t}{\gamma} \iint dx dy \mathbf{m} \cdot \left(\frac{\partial \mathbf{m}}{\partial x} \right) \times \left(\frac{\partial \mathbf{m}}{\partial y} \right) \quad (2.4)$$

$$D_{ij} = \frac{M_s t}{\gamma} \iint dx dy \mathbf{m} \cdot \left(\frac{\partial \mathbf{m}}{\partial x_i} \right) \cdot \left(\frac{\partial \mathbf{m}}{\partial x_j} \right) \quad (2.5)$$

where M_s is the saturation magnetization, t is the thickness of the FM, γ is the gyromagnetic ratio and \mathbf{m} is the numerical magnetization tensor. First of all, the analysis of numerical results demonstrated that $G_{DSk} \sim 2 G_{Sk}$, implying that the simplified expression $G = -(M_s t / \gamma) \cdot 4\pi Q$, valid for conventional skyrmionic bubble, can be also adopted for double skyrmion. Secondly, again consistently to the magnetic skyrmion description, the main diagonal elements of the dissipative tensor turned out to be nearly equivalent ($D_{xx} = D_{yy} = D$), and several orders of magnitude larger than D_{xy} and D_{yx} , which can thus be neglected. Also, it was found that the DSk topological charge $Q = +2$, responsible for the doubled G value, is not fully compensated by D , being $D^{DSk} \sim 1.9 D^{Sk}$. This finally explains the slightly larger SkHA measured for the double skyrmion.

A fourth salient difference between the two topological excitations can be found in the characteristic *kink* orientation, aligned nearly transverse to the direction of motion. Specifically, the angle in between the *kink* alignment axis and the interface spin vector $\boldsymbol{\sigma} = \mathbf{J}_{app} \times \hat{\mathbf{z}}$ was measured to be approximately equal to 70° . To be more precise, during the transient period prior the steady-state motion and lasting around 2 ns, the double skyrmion rotates so as the *kink* can align along a preferred direction. This observation can be again reasoned in the frame of the DL-SOT analytical model. In particular, by imposing $\mathbf{J}_{app} = J_{app} \hat{\mathbf{x}}$, the DL-SOT force \mathbf{F}_{DL} can be computed according to the following expression [47]:

$$F_{DL,i} = \mu_0 M_s t H_{DL}^0 \iint dx dy \left(m_x \frac{\partial m_z}{\partial x_i} - m_z \frac{\partial m_x}{\partial x_i} \right) \quad (2.6)$$

where $H_{DL}^0 = C_{DL} J_{app} / \mu_0$, being C_{DL} the effective magnetic field per unit current density (in $\text{T A}^{-1} \text{m}^2$) and $i = x, y, z$.

As a matter of fact, for a purely Néel (respectively Bloch) magnetic skyrmion, such DL-SOT force is collinear (respectively transverse) to the current density vector [47]. Upon this statement one can infer that, due to the partial Bloch-like nature of the domain wall introduced by local *kink*, in contrast to the skyrmionic bubble, the double skyrmion would be subjected to a non-zero transverse force, affecting its motion. By implementing the above equation for a *DSk*, the transverse force component $F_{DL,y}$ was found to be orders of magnitude greater than Sk . Also, the map of the DL-SOT force density, revealed that $F_{DL,y}$ is highly concentrated on the *kink*. This could ultimately explain the torque experienced by the 1-D skyrmion during the SOT driven motion.

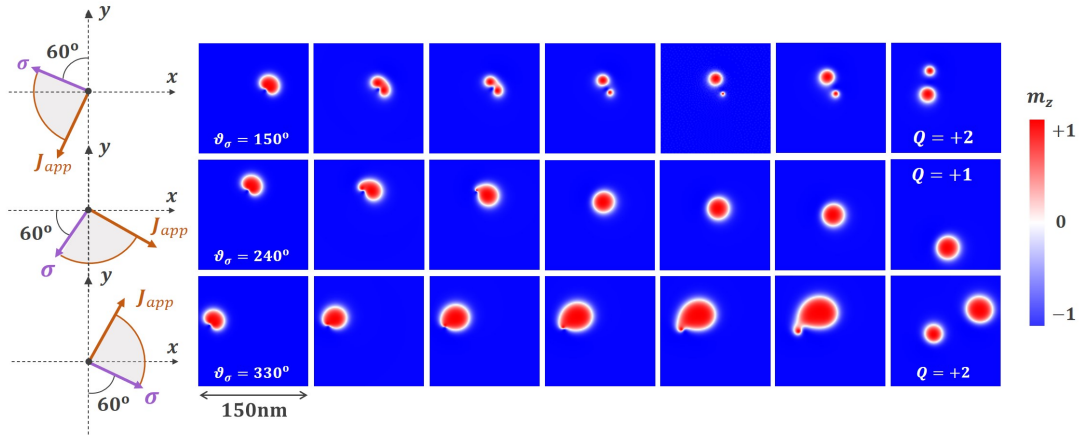


Figure 2.20: Illustration of double skyrmion response to CIP-SOT in high-current regime for $J_{app} = 100 \times 10^{10} \text{ A/m}^2$ and $\mu_0 H_{app} = -20 \text{ mT}$ applied perpendicular to the plane. The color scale refers to Out-Of-Plane (OP) magnetization. Top, middle and bottom lines are associated to interface spin polarizations $\theta_\sigma = 150^\circ$, 240° and 330° , respectively.

The double skyrmion dynamic response profiled up to this point generalizes to all the injection conditions included in the region of low and medium current regimes of Figure 2.19 c): here, the effective diameter and velocity of both topological solitons increase upon reinforcing the applied current density. However, it is possible to identify a critical current density value, measured to be $J_{app} = 50 \times 10^{10} \text{ A/m}^2$ with a resolution of $10 \times 10^{10} \text{ A/m}^2$, which marks the boundary with the high current regime. In the high current regime, as illustrated in Figure 2.20, the physics drastically changes. Characteristically, due to the powerful torque exerted by the spins accumulated at the HM/FM interface, the *DSk* topological charge is subjected to a non-conservative transformation, which is determined by the injection geometry.

In detail, such $Q = +2$ quasi-particle in the track can be converted either into two $Q = +1$ quasi-particles, i.e. two distinguished skyrmionic bubbles, or into one $Q = +1$ quasi-particle, i.e. one unique skyrmionic bubble. A methodical description of the current induced manipulation of the topological charge could open avenues to conceive high density skyrmionic devices.

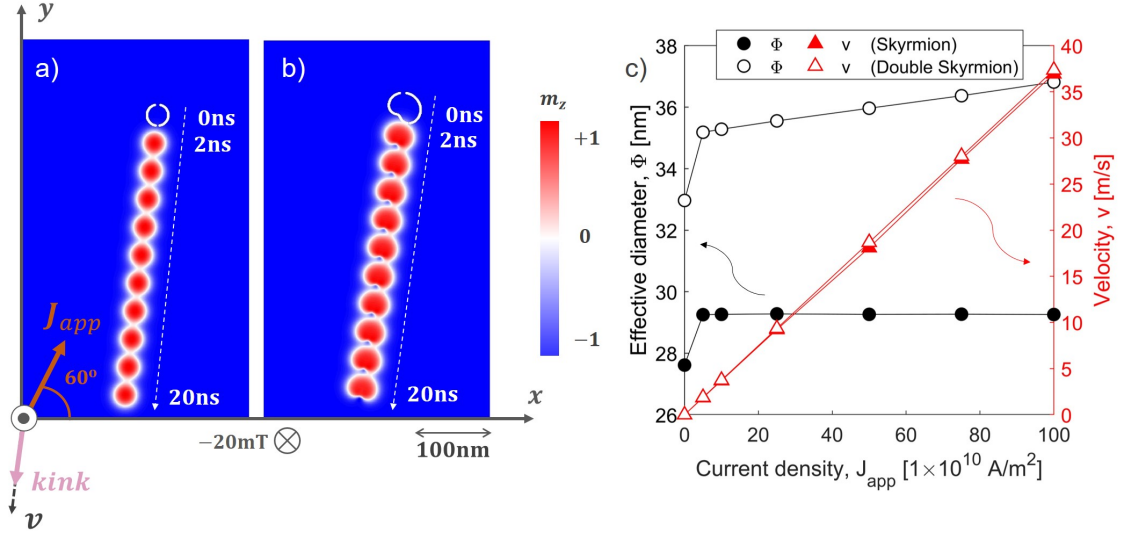


Figure 2.21: Illustration of CIP-STT driven motion of a) skyrmionic bubble and b) double skyrmion, for $J_{app} = 50 \times 10^{10}$ A/m 2 and $\mu_0 H_{app} = -20$ mT applied perpendicular to the plane. The color scale refers to Out-Of-Plane (OP) magnetization. c) Comparison of effective diameter Φ (black line) and velocity v (red line) vs. STT current density J_{app} characteristics for skyrmionic bubble and double skyrmion, with $\mu_0 H_{app} = -20$ mT applied perpendicular to the plane. The white contours in a) and b) represent the initial magnetization states. The electrical current polarization is 10%.

The double skyrmion CIP-STT driven dynamics, illustrated in Figure 2.21 for an electrical current polarization of 10%, reveals a physics far less complex than CIP-SOT driven motion. Indeed, the double skyrmion can be displaced along the track without being annihilated for all the explored conditions. In this instance, the *kink* is aligned along the displacement direction, particularly at the head of the motion. Indeed, the STT increases with magnetization gradient, that is much larger in the *kink*. As a consequence, the *kink* drives the motion. The direction of motion for both topological solitons is consistent with the electron flow; however, the trajectories present again a slight angular tilting with respect to the applied current density vector. This is again due to the Skyrmion Hall Angle, equivalent to the case for CIP-SOT driven motion, as expected.

What is more, the DSk and Sk velocity curves, varying linearly with the injected current density, are nearly superposed to each other. While the size of the Sk remains unaffected by the increasing exerted torque, the DSk effective diameter, beyond exceeding that of the Sk , exhibits a very slow linear increase.

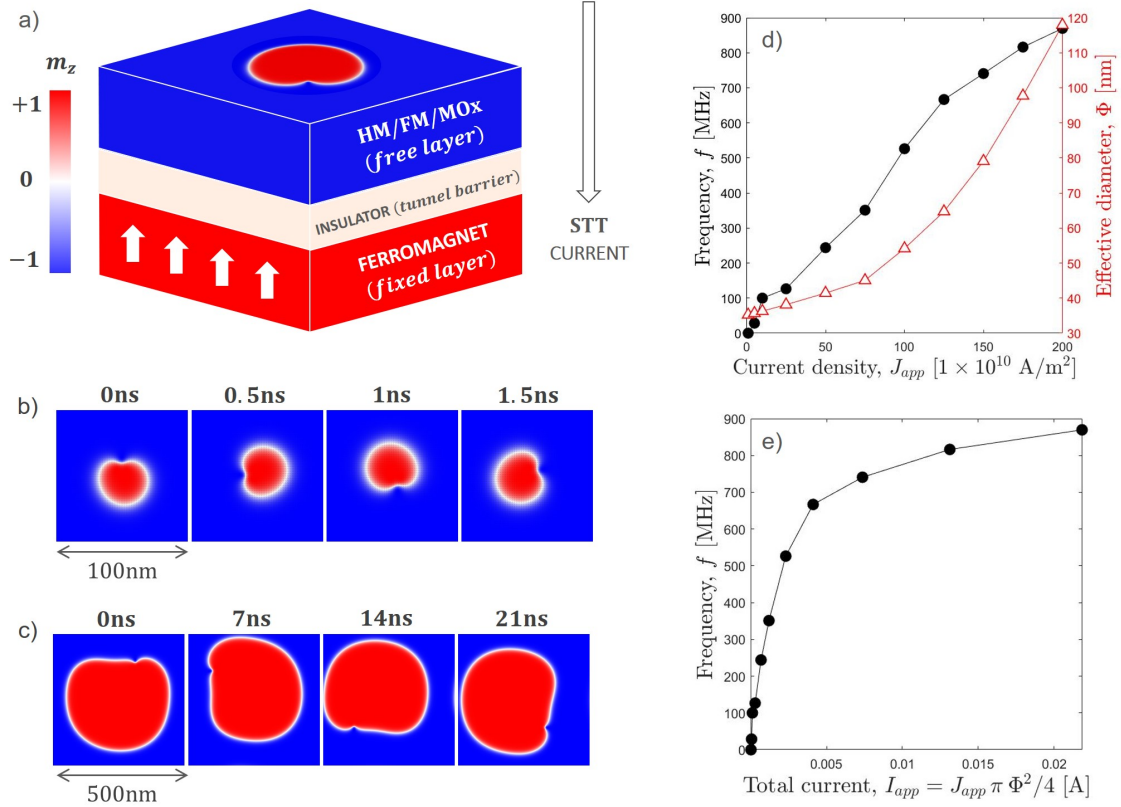


Figure 2.22: a) Schematics of Magnetic Tunnel Junction (MTJ) with the magnetic stack HM/FM/MOx used as *free layer* and CPP-STT current. Illustration of auto-oscillation sub-periods for PBC (1, 1, 0), $J_{app} = 100 \times 10^{10} \text{ A/m}^2$ at b) $\mu_0 H_{app} = -20 \text{ mT}$ and c) $\mu_0 H_{app} = 0 \text{ mT}$ applied perpendicular to the plane. d) Double skyrmion frequency of auto-oscillation f (black curve) and effective diameter Φ (red curve) vs. CPP-STT current density J_{app} for Out-Of-Plane (OP) Zeeman field $\mu_0 H_{app} = -20 \text{ mT}$ and PBC (1, 1, 0). e) Double skyrmion frequency of auto-oscillation f vs. CPP-STT current I_{app} for OP Zeeman field $\mu_0 H_{app} = -20 \text{ mT}$ and PBC (1, 1, 0), where I_{app} is the total current crossing the DSk magnetic domain. The color scale refers to OP magnetization.

A more exotic and fascinating physical phenomenon was observed when Current Perpendicular-to-Plane (CPP) STT in the presence of a perpendicular polarizer was applied to the double skyrmion. To be more detailed, in the numerically implemented experiment, the magnetic stack under study is used as a *free layer* of a Magnetic Tunnel Junction (MTJ), also comprising a thin insulator (tunnel barrier) and an Out-Of-Plane (OP) *fixed layer*, as illustrated in Figure 2.22 a). When a current is flowing perpendicular to the plane, the *fixed layer* thus provides on the double skyrmion spins that are polarized in the $+z$ or $-z$ direction. Subsequently to the injection of a STT current across the magnetic stack, a steady-state auto-oscillation of the double skyrmion is inducted, driven by the *kink* pinpointed in the domain wall. Indeed, owing to the electron spin perpendicular polarization, the Slonczewski torque (Equation 1.40) can affect only regions of the FM with non-zero In-Plane (IP) magnetization, i.e. the domain wall. Moreover, as an outgrowth of the broken rotational symmetry around the z axis, introduced by the presence of the local *kink*, the *DSk* reacts to the CPP-STT with a rotational motion, synchronized to the frequency of $m_{x,y}$ periodic oscillation (concurrent with the STT driven motion). This phenomenon is not observed for the *Sk* counterpart, responding just with a damped breathing mode (resonance mode causing the core of the swirling spin structure expanding and compressing periodically over time), due to *Sk* cylindrical symmetry.

The study was carried out in presence of an external magnetic field $\mu_0 H_{app} = -20$ mT, for consistency with the previous analysis (CIP-STT), and *up* polarization of the *fixed layer*. For positive current, the direction of the electron flow, opposing the electric current flux, is from the *fixed* to the *free* layer. As shown in Figure 2.22 b), depicting four time frames of a spinning sub-period for the case $J_{app} = 100 \times 10^{10}$ A/m², the topological soliton rotates anti-clockwise (ACW). The preferential direction of rotation can be more easily explained by repeating the experiment for a *kink* of charge $Q = +1$ located on a flat domain wall, i.e. a domain wall skyrmion (not shown). In this context, the left displacement of the non-trivial spin texture, modeled by the damping-like (DL) STT effective magnetic field, is in perfect agreement with numerical observations. In a conceptual experiment, this *DWSk* can be imaged as an extremely-localized 1-D skyrmion accommodated on the domain wall of a relatively huge skyrmionic bubble: the local *kink* thus perceives the extended circular domain wall as locally flat and undergoes an unidirectional displacement. If we now imagine to shrink the relative extent of the domain wall, this latter returns to be a circular, and no more linear, track in the *kink* frame of reference. The local *kink*, being confined in such track, while displacing towards the left, is forced to follow the contour of the domain wall, from which it cannot escape. The linear one-way (left) displacement is thus converted into a rotation motion with well-defined sense of rotation (ACW). Figure 2.22 d) shows how the frequency of

rotation, in the low and medium current regimes, increases upon reinforcing the applied current density, because of the even stronger CPP-STT torque. At the same time, the core of the double skyrmion, polarized coherently with the *fixed layer*, keeps expanding with the increasing frequency of rotation, slightly slowing down the auto-oscillations. As a result, the frequency of rotation exhibits a saturating behavior versus the total current injected in the *DSk*, computed by multiplying the applied current density by the *DSk* area, as shown in Figure 2.22 e). Indeed, as a consequence of the expansion of the core size, the *kink* to domain wall lengths ratio drastically decreases, meaning that the impact of the *kink*, which propels the motion, becomes even less significant. In support of this claim it is also proved that, if the applied magnetic field is shut down, thus the *DSk* area is increased, e.g. for $J_{app} = 100 \times 10^{10} \text{ A/m}^2$, the frequency of rotation decreases by more than one order of magnitude, as illustrated in Figure 2.23 c). Upon this, one can infer that the effectiveness of the oscillatory motion can be improved by reversing the polarization of the fixed layer from *up* to *down* or, equivalently, by inverting the sign of injected current.

By gradually reinforcing the STT current density above a critical value ($\sim J_{app} = 200 \times 10^{10} \text{ A/m}^2$), marking the border with the high current regime, first multiple *up* magnetic domains are nucleated, then a final saturated *up* magnetization state is obtained (not shown). The critical applied current density is observed to decrease when the damping factor of the material increases. Interestingly, the dynamic evolution of the multi-domain states in high-current regime reveals the presence of several *kinks* ($Q = +1$) and *anti-kinks* ($Q = -1$) localized in the domain walls. This observation opens the perspective of using such an MTJ structure for both nucleating double skyrmions and further activating their auto-oscillation. The established steady rotation, in its turn, opens avenues for realizing *DSk*-based spin-torque nano-oscillators in overdamped materials.

2.4 Other non-trivial spin textures

A randomly distributed thermal field can catalyze the spontaneous nucleation of one or multiple 1-D skyrmions in the domain wall of a skyrmionic bubble. The usual numerical procedure adopted to stabilise and further characterize a conventional skyrmionic bubble is to initialize the micromagnetic simulator by a circular magnetic domain antiparallel to the magnetic environment (see Section 2.1). The interfacial-DMI then promotes the generation of an in-between Néel-type domain wall – with well-defined chirality – during the energy relaxation transient phase. Having an external random perturbation during this stage, e.g. induced by a thermal field, excites the nucleation of extremely confined 1-D skyrmions in such domain wall. In other words, the heat energy, either due to the ambient temperature (during relaxation) or due to a laser pulse (prior to relaxation), assists the magnetization to locally counteract the Dzyaloshinskii-Moriya interaction, bringing out local magnetic *kinks* breaking the chiral homogeneity of the domain wall. Against this backdrop, the dipolar field seems to play a crucial role, promoting the local whirling of In-Plane (IP) magnetization – to close the magnetic field flux lines radiated by the domain wall – as it thermally floats. To corroborate this idea, the dipolar interaction was disabled and no twists of magnetization were in fact observed in the domain wall during the transient time. This finally proves that domain wall skyrmions not only withstand thermally induced fluctuation but that they are effectively triggered by it. Figure 2.23 illustrates a sequence of thermally nucleated non-trivial spin textures, described by integer topological charge values varying from $Q = +2$ to $Q = -3$ in steps of $Q = -1$. The final topological charge is determined by the balance, at the first time steps of energy relaxation, between 1-D skyrmions of both topological charge $Q = +1$ (*kinks*) and $Q = -1$ (*anti-kinks*), which annihilate in pairs. The design of an experimental protocol to locally nucleate 1-D skyrmions in a controlled manner may pave the way to develop versatile skyrmionic devices where the digital information is encoded in topological charge of the solitonic magnetic texture. Furthermore, the even larger number of (*anti-*)*kinks* may make the auto-oscillation of such topological solitons increasingly efficient.

During the thesis work, further to double skyrmion ($Q = +2$) and skyrmion ($Q = +1$), the attention was focused on the so-called magnetic droplet [55], characterized by a skyrmionic bubble ($Q = +1$) having an *anti-kink* on the domain wall ($Q = -1$): the total topological charge is thus $Q = 0$, as the uniform magnetization state. The magnetic droplet presents a total energy that, despite still larger than skyrmionic bubble, is slightly smaller than double skyrmion. This is because the droplet area is closer to the value which would exactly compensate the area of the outer magnetic domain. This, compared to the *DSk* case, implies a reduction of the stray field radiated out of the sample, thus of dipolar energy.

Nevertheless, the droplet can be stabilized only in a narrow range of both out-of-plane negative Zeeman field ($\mu_0 H_c = -2$ mT) and i DMI strength values ($\Delta D_c = -8\%$), as shown in Figures 2.24 a) and b). It disappears otherwise into the ground single domain state, which could be explained by a smaller or vanishing annihilation barrier as compared to non-zero Q spin textures. Upon this, it is prevented to effectively establish control of the droplet size, as a consequence of the loss of total topological charge. However, despite being extremely susceptible to annihilation under CIP-STT and/or SOT compared to (double) skyrmion, the droplet can be moved in a track along the direction of the applied current. Moreover, due to its zero topological charge, it is not subjected to Skyrmion Hall Effect (not shown).

The behaviour of the droplet under CPP-STT was then tested. In Figure 2.24 c) it is possible to observe how for $J_{app} = 100 \times 10^{10}$ A/m², $\mu_0 H_{app} = -2$ mT applied perpendicular to the plane and no PBC, the droplet auto-oscillates. First, the droplet spinning motion opposes the direction of rotation observed for double skyrmion. Indeed, for a left-handed (LH) skyrmionic bubble, the magnetic *anti-kink* ($Q = -1$) of the droplet is configured Head-To-Head (H2H). This is in opposition to the magnetic *kink* ($Q = +1$) of the double skyrmion, which is in fact Tail-to-Tail (T2T). The 1-D skyrmion specificity indeed determines the space distribution of the effective magnetic field which, in its turn, controls the displacement direction. The opposite sense of rotation of the droplet with respect to the DSk may be explained again through the direction of motion of the *anti-kink* within a flat domain wall. Second, under the same injection conditions, the droplet frequency of rotation ($f \sim 30$ MHz) at $\mu_0 H_{app} = -2$ mT is smaller than what measured for double skyrmion ($f \sim 38$ MHz) for no applied magnetic field. This is likely due to the elongated shape of the droplet which, contrary to the double skyrmion, does not adapt to the sample geometry while rotating. Also, being $\mu_0 H_{app} = -2$ mT the critical Zeeman field, it is prevented to further reduce the droplet size to speed up the auto-oscillation. Upon these considerations, the magnetic droplet reveals ultimately weaker stability and tunability than double skyrmion.

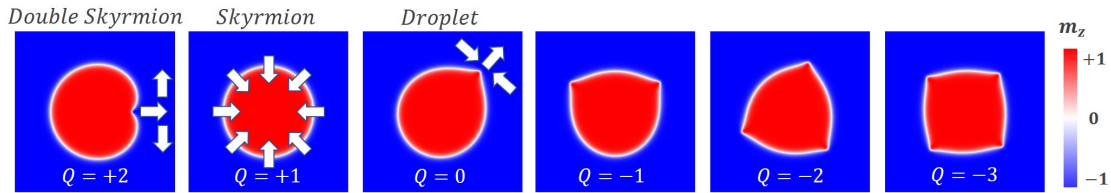


Figure 2.23: Illustration of different non-trivial spin textures numerically stabilised in Pt/Co(0.9 nm)/MgO. The white arrows schematically represent the 1-D skyrmion magnetic configuration for the double skyrmion ($Q = +2$) and the droplet ($Q = +0$), and the IP magnetization in the domain wall of skyrmion. The color scale refers to Out-Of-Plane (OP) magnetization.

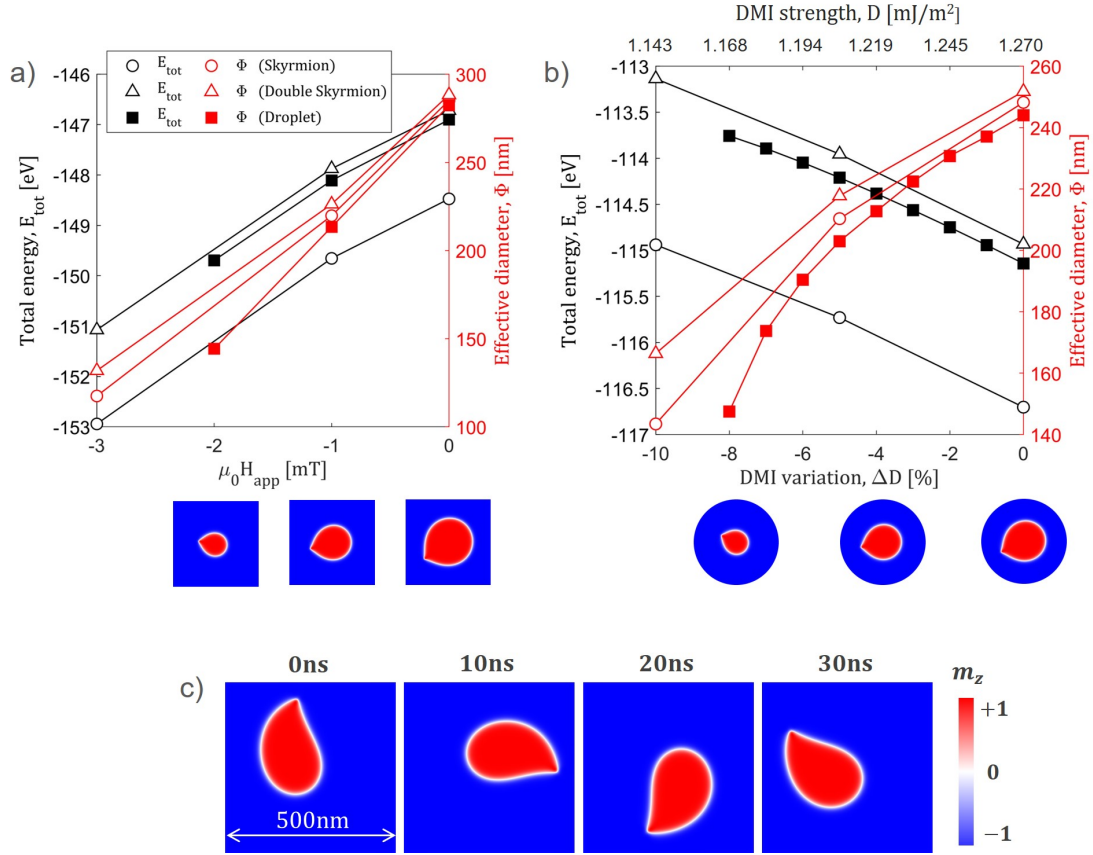


Figure 2.24: Droplet total energy E_{tot} (black curve) and effective diameter Φ (red curve) compared to double skyrmion and skyrmion characteristic behavior vs. a) Out-Of-Plane (OP) Zeeman field $\mu_0 H_{app}$ (square geometry) and b) i DMI coefficient D (circular geometry). c) Illustration of droplet auto-oscillation sub-periods under CPP-STT for no PBC, $J_{app} = 100 \times 10^{10}$ A/m² and $\mu_0 H_{app} = -2$ mT applied perpendicular to plane. The color scale refers to OP magnetization.

Chapter 3

Conclusions & perspectives

The possibility to stabilize Néel magnetic skyrmions at ambient temperature in sputtered ultra-thin films has been recently demonstrated for the magnetic stack of the type Pt/Co(0.9 nm)/MgO, thanks to the large interfacial Dzyaloshinskii–Moriya Interaction (*i*DMI) of such systems [5]. These topological solitons have aroused great interest not only for the underlying physics, but also because their adjustable nanometric size and effective Spin–Orbit Torque driven motion make them promising as dense storage data bits, either for memory and logic applications or for neuromorphic computing [2]. In this thesis work, the aforementioned thin-film system was investigated by micromagnetic modelling, with a view to improve the understanding of the physics underneath *i*DMI and to identify and characterize potential peculiar stable states. To follow the main achievements of this master thesis will be highlighted.

Upon being thermally demagnetized by an ultra-fast laser pulse, on the basis of the Zeeman field acting during the magnetization recovery process, the ferromagnetic layer can reach two distinct stable states, that are: (1) the **hexagonal-like skyrmion bubble lattice**, (2) the **magnetic multidomain state**.

1. The skyrmion bubble lattice is made up of fifteen Néel skyrmions ($Q = +15$) joined by the mutual (long-range) dipolar interaction. The magnetic skyrmions are shown to survive thermally induced fluctuations and to expand apart from each other when the repulsive force from the sample edges is disabled, upon imposing Periodic Boundary Conditions. This is along the lines of prior experimental observations present in literature [7].
2. The magnetic multidomain state, besides flat domain walls ($Q = 0$), comprises concurrent non-trivial spin textures that are: the **skyrmionic bubble** ($Q = +1$); the **domain wall skyrmion** ($Q = +1$), i.e. a 1-D skyrmion located on a flat domain wall; and the **double skyrmion** ($Q = +2$), i.e. a 1-D skyrmion tracked on a circular domain wall. The 1-D skyrmion is a confined

region of the domain wall where the in-plane magnetization rotates by $2 - \pi$, which results in a strong bending of the domain wall. Furthermore, its core magnetization opposes the chirality enforced by the i DMI sign. The numerical uncovering of the domain wall skyrmion is perfectly consistent with the most recent experimental findings in literature but for different magnetic stacks [50]. Anyway, the observation of the double skyrmion stability after magnetization recovery process is unprecedented and represents the major contribution to the literature of this thesis work (F. Nasr et al., in preparation). The multidomain state has been demonstrated to survive thermal field, again inducing a blurring of the domain wall, and granularity typical of polycrystalline materials. This proves that the ultra-confined 1-D skyrmions are extremely robust and hard to be unwhirled.

Additionally, the conventional skyrmionic bubble ($Q = +1$) and the novel double skyrmion ($Q = +2$) were isolated and characterized with regard to static and dynamic properties.

In sight of experimentally operating the voltage gating of interfacial magnetic properties, a skyrmionic bubble phase diagram was composed by combining variations of magnetic anisotropy K_u and i DMI coefficient D . In particular, starting from a skyrmion bubble, it was shown that the tuning of the i DMI strength makes it accessible either the nanometer magnetic skyrmion (D reduction) or the spin spiral state (D increase). Concurrently, the variation of the interface magnetic anisotropy allows either to reduce the critical i DMI strength to enter the spin spiral phase (K_u reduction) or to reduce the skyrmionic bubble size and eventually access to the single domain state (K_u increase). Then, the magnetic response of the sample to a Zeeman field was investigated at the reference values of D and K_u , by extracting the skyrmionic bubble hysteresis loop. Furthermore, the application of a magnetic field was observed to restore the skyrmionic bubble of polarity $p = -1$ starting either from the up single domain state ($\mu_0 H_{app} < 0$) or from the spin spiral state ($\mu_0 H_{app} > 0$).

The double skyrmion was then cross-referenced to conventional skyrmionic bubble, by systematically studying the two topological excitations in parallel. Overall, both the static and dynamic properties for the two cases studies were shown to be akin to each other. Particularly, the accomplishment of both size tuning – operated by control parameter, i.e. magnetic field, and internal material parameters, such as the i DMI strength – and chirality reversal were numerically predicted. Also, the effective displacement in a track both under Current-In-Plane (CIP) Spin Transfer Torque (STT) and Spin-Orbit Torque (SOT) was observed. However, the double skyrmion ($Q = +2$) may be converted into a single 2-D skyrmion ($Q = +1$) either in presence of a strong Zeeman field, anti-parallel to the core polarity – as a consequence of the contraction of the domain wall – or under high CIP-SOT –

as a consequence of the strong spin torque acting on the magnetic texture. Also, it was proved that there exist particular CIP-SOT current injection geometries in the heavy-metal layer which produce a conservative transformation of the topological charge in high-current regime, i.e. double skyrmion ($Q = +2$) conversion into two magnetic skyrmions ($2 \times$ *quasi-particles* of $Q = +1$). What is more, contrary to skyrmionic bubble, the action of Current Perpendicular-to-Plane (CPP) Spin Transfer Torque (STT) in a Magnetic Tunnel Junction (MTJ), with the Pt/Co(0.9 nm)/MgO used as *free layer* and perpendicularly polarized *reference layer*, may induce the double skyrmion auto-oscillation. Here, the rotational motion is driven by the 1-D skyrmion and the specific direction of rotation at fixed chirality is determined by *reference layer* polarization, either *up* or *down*.

The thermal nucleation of one or multiple 1-D skyrmions on the otherwise homochiral bubble domain wall for the trilayer system Pt/Co(0.9 nm)/MgO, evidenced by micromagnetic simulations, calls for validation via experimental work. The establishment of opto-electrical control of such topological spin textures, i.e. by using ultra-fast laser pulses, combined with spin-polarized current and gate voltage, would break new ground to design novel high-density skyrmionic devices, based on:

- the discrete variation of topological charge, controlled by the number of 1-D skyrmions on the chiral bubble domain wall;
- the topological charge (non-conservative) manipulation;
- the physical mechanism of auto-oscillations.

Bibliography

- [1] Gambardella, P. & Miron, I. M. (2011). Current-induced spin–orbit torque. *Phil. Trans. R. Soc. A.*, *369*, 3175–3197. DOI: <http://doi.org/10.1098/rsta.2010.0336>
- [2] Fert, A., Reyren, N. & Cros, V. (2017). Advances in the Physics of Magnetic Skyrmions and Perspective for Technology. *Nat. Rev. Mater.*, *2*, 17031. DOI: <https://doi.org/10.1038/natrevmats.2017.31>
- [3] Kuchkin, V. M., Barton-Singer, B., Rybakov, F. N., Blügel, S., Schroers, B. J. & Kiselev, N. S. (2020). Magnetic skyrmions, chiral kinks, and holomorphic functions. *Phys. Rev. B*, *102*, 144422. DOI: <https://doi.org/10.1103/PhysRevB.102.144422>
- [4] Je, S.G. (2021). Topological charge analysis of dynamic process of transition to Néel-type skyrmion: role of domain wall skyrmions. *Curr. Appl. Phys.*, *21*, 175–179. DOI: <https://doi.org/10.1016/j.cap.2020.10.021>
- [5] Boulle, O., Vogel, J., Yang, H., Pizzini, S., de Souza Chaves, D., Locatelli, A., ... Gaudin, G. (2016). Room-temperature chiral magnetic skyrmions in ultrathin magnetic nanostructures. *Nat. Nanotechnol.*, *11*, 449–454. DOI: <https://doi.org/10.1038/nnano.2015.315>
- [6] Juge, R., Je, S.G., de Souza Chaves, D., Buda-Prejbeanu, L., Peña-Garcia, J., Nath, J., ... Boulle, O. (2019). Current-Driven Skyrmion Dynamics and Drive-Dependent Skyrmion Hall Effect in an Ultrathin Film. *Phys. Rev. Appl.*, *12*, 044007. DOI: <https://doi.org/10.1103/PhysRevApplied.12.044007>
- [7] Je, S.G., Vallobra, P., Srivastava, T., Rojas-Sánchez, J., Pham, T., Hehn, M., ... Boulle, O. (2018). Creation of Magnetic Skyrmion Bubble Lattices by Ultrafast Laser in Ultrathin Films. *Nano Lett.*, *18*, 7362–7371. DOI: <https://doi.org/10.1021/acs.nanolett.8b03653>
- [8] Cheng, R., Li, M., Sapkota, A., Rai, A., Pokhrel, A., Mewes, T. ... Sokalski, V. (2019). Magnetic domain wall skyrmions. *Phys. Rev. B*, *99*, 184412. DOI: <https://doi.org/10.1103/PhysRevB.99.184412>
- [9] Voinigescu, S. (2013). *High-Frequency Integrated Circuits* (The Cambridge RF and Microwave Engineering Series). Cambridge: Cambridge University Press. DOI: <https://doi.org/10.1017/CB09781139021128>
- [10] Hirohata, A., Yamada, K., Nakatani, Y., Prejbeanu, I.L., Diény, B., Pirro, P.

- & Hillebrands, B. (2020). Review on spintronics: Principles and device applications. *J. Magn. Magn. Mater.*, 509, 166711. DOI: <https://doi.org/10.1016/j.jmmm.2020.166711>
- [11] Hirohata, A. (2015, September 2). Shift from electronics to spintronics opens up possibilities of faster data. Retrieved from <https://theconversation.com/shift-from-electronics-to-spintronics-opens-up-possibilities-of-data-45864>
- [12] Moore, S. K. (2020, July 21). A Better Way to Measure Progress in Semiconductors. It's time to throw out the old Moore's Law metric. Retrieved from <https://spectrum.ieee.org/semiconductors/devices/a-better-way-to-measure-progress-in-semiconductors>
- [13] Khanna, V. (2016). Short-Channel Effects in MOSFETs. *Integrated Nanoelectronics: Nanoscale CMOS, Post-CMOS and Allied Nanotechnologies*, 73–93. New Delhi: Springer. DOI: <https://doi.org/10.1007/978-81-322-3625-2>
- [14] Asenov, A. (1998). Random dopant induced threshold voltage lowering and fluctuations in sub-0.1 μm MOSFET's: A 3-D “atomistic” simulation study. *IEEE Trans. Electron Devices*, 45, 2505–2513. DOI: <https://doi.org/10.1109/16.735728>
- [15] IEEE International Roadmap for Devices and Systems (2020). *More Moore*.
- [16] Titiksha Srivastava. Engineering and dynamical control of interfacial properties in ultra-thin films to tune magnetic spin textures. *Materials Science* [cond-mat.mtrl-sci]. Université Grenoble Alpes, 2019. English. NNT: 2019GREAY001. tel-02273960.
- [17] Brataas, A., Kent, A. D. & Ohno, H. (2012). Current-induced torques in magnetic materials. *Nat. Mater.*, 11, 372–381. DOI: <https://doi.org/10.1038/nmat3311>
- [18] Dai, M. & Hu, J.M. (2020). Field-free spin-orbit torque perpendicular magnetization switching in ultrathin nanostructures. *npj Comput. Mater.*, 6, 78. DOI: <https://doi.org/10.1038/s41524-020-0347-0>
- [19] Jiang, M., Asahara, H., Sato, S., Kanaki, T., Yamasaki, H., Ohya, S. & Tanaka, M. (2019). Efficient full spin-orbit torque switching in a single layer of a perpendicularly magnetized single-crystalline ferromagnet. *Nat. Commun.*, 10, 2590. DOI: <https://doi.org/10.1038/s41467-019-10553-x>
- [20] Parkin, S., Hayashi, M. & Thomas, L. (2008). Magnetic Domain-Wall Racetrack Memory. *Science*, 320, 190–194. DOI: <https://doi.org/10.1126/science.1145799>
- [21] Zhang, X., Zhou, Y., Song, K., Park, T.E., Xia, J., Ezawa, M., ... Woo, S. (2020). Skyrmion-electronics: Writing, deleting, reading and processing magnetic skyrmions toward spintronic applications. *J. Phys.: Condens. Matter.*, 32, 143001. DOI: <https://doi.org/10.1088/1361-648X/ab5488>
- [22] Krause, S. & Wiesendanger, R. (2016). Skyrmionics gets hot. *Nat. Mater.* 15, 493–494. DOI: <https://doi.org/10.1038/nmat4615>

- [23] Wang, L., Feng, Q., Kim, Y., Kim, R., Lee, K., Pollard, S., . . . Noh, T. (2018). Ferroelectrically tunable magnetic skyrmions in ultrathin oxide heterostructures. *Nat. Mater.*, *17*, 1087–1094. DOI: <https://doi.org/10.1038/s41563-018-0204-4>
- [24] Fert, A., Cros, V. & Sampaio, J. (2013). Skyrmions on the track. *Nat. Nanotechnol.*, *8*, 152–156. DOI: <https://doi.org/10.1038/nnano.2013.29>
- [25] Kang, W., Huang, Y., Zhang, X., Zhou, Y. & Zhao, W. (2016). Skyrmion-Electronics: An Overview and Outlook. *Proceedings of the IEEE*, *104*, 2040–2061. DOI: <https://doi.org/10.1109/JPROC.2016.2591578>
- [26] Woo, S., Song, K., Han, H.S., Jung, M.S., Im, M.Y., Lee, K.S., . . . Chang, J. (2017). Spin-orbit torque-driven skyrmion dynamics revealed by time-resolved X-ray microscopy. *Nat. Commun.*, *8*, 15573. DOI: <https://doi.org/10.1038/ncomms15573>
- [27] Dzyaloshinskii, I. (1958). A thermodynamic theory of “weak” ferromagnetism of antiferromagnetics. *J. Phys. Chem. Solids*, *4*, 241–255. DOI: [https://doi.org/10.1016/0022-3697\(58\)90076-3](https://doi.org/10.1016/0022-3697(58)90076-3)
- [28] Moriya, T. (1960). New Mechanism of Anisotropic Superexchange Interaction. *Phys. Rev. Lett.*, *4*, 228–230. DOI: <https://doi.org/10.1103/PhysRevLett.4.228>
- [29] Bayreuther, G., Dumm, M., Uhl, B., Meier, R. & Kipferl, W. (2003). Magnetocrystalline volume and interface anisotropies in epitaxial films: Universal relation and Néel’s model (invited). *J. Appl. Phys.*, *93*, 8230–8235, DOI: <https://doi.org/10.1063/1.1558638>
- [30] Berganza, E., Jaafar, M., Fernández-Roldán, J. Á., Goiriena-Goikoetxea, M., Pablo-Navarro, J., García Arribas, A., . . . Asenjo, A. (2020). Half-hedgehog spin textures in sub-100 nm soft magnetic nanodots. *Nanoscale*, *12*, 18646–18653. DOI: <https://doi.org/10.1039/D0NR02173C>
- [31] Park, Y.K., Kim, D.Y., Kim, J.S., Nam, Y.S., Park, M.H., Choi, H.C., . . . Min, B.C. (2018). Experimental observation of the correlation between the interfacial Dzyaloshinskii–Moriya interaction and work function in metallic magnetic trilayers. *NPG Asia Mater.*, *10*, 995–1001. DOI: <https://doi.org/10.1038/s41427-018-0090-x>
- [32] Fert, A. & Levy, P. (1980). Role of Anisotropic Exchange Interactions in Determining the Properties of Spin-Glasses. *Phys. Rev. Lett.*, *44*, 1538. DOI: <https://doi.org/10.1103/PhysRevLett.44.1538>
- [33] Kim, K.W., Lee, H.W., Lee, K.J. & Stiles, M. D. (2013). Chirality from Interfacial Spin-Orbit Coupling Effects in Magnetic Bilayers. *Phys. Rev. Lett.*, *111*, 216601. DOI: <https://doi.org/10.1103/PhysRevLett.111.216601>
- [34] Slonczewski, J. C. (1996). Current-driven excitation of magnetic multilayers. *J. Magn. Magn. Mater.*, *159*, L1-L7. DOI: [https://doi.org/10.1016/0304-8853\(96\)00062-5](https://doi.org/10.1016/0304-8853(96)00062-5)
- [35] Gilbert, T (2004). A phenomenological theory of damping in ferromagnetic

- materials. *IEEE Trans. Magn.*, 40, 3443–3449. DOI: <https://doi.org/10.1109/TMAG.2004.836740>
- [36] Landaue, L. & Lifshitz, E. (1992). On the theory of the dispersion of magnetic permeability in ferromagnetic bodies. *Physik. Zeits. der Sow.*, 8, 153–169. DOI: <https://doi.org/10.1016/B978-0-08-036364-6.50008-9>
- [37] Vansteenkiste, A., Leliaert, J., Dvornik, M., Helsen, M., Garcia-Sanchez, F. & Van Waeyenberge, B. (2014). The design and verification of MuMax3, *AIP Adv.*, 4, 107133. DOI: <https://doi.org/10.1063/1.4899186>
- [38] Thiaville, A., Nakatani, Y., Miltat, J. & Suzuki, Y. (2005). Micromagnetic understanding of current-driven domain wall motion in patterned nanowires. *EPL*, 69, 990–996, DOI: <https://doi.org/10.1209/epl/i2004-10452-6>
- [39] Garate, I., Gilmore, K., Stiles, M. & MacDonald, A. (2008). Non-Adiabatic Spin Transfer Torque in Real Materials. *Phys. Rev. B*, 79, 104416, DOI: <https://doi.org/10.1103/PhysRevB.79.104416>
- [40] Wikipedia contributors (2020, October 29). Runge–Kutta methods. *Wikipedia, The Free Encyclopedia*. Retrieved January 05, 2021, from https://en.wikipedia.org/w/index.php?title=Runge%E2%80%93Kutta_methods&direction=next&oldid=985965450
- [41] Conde, S., Fekete, I. & Shadid, J. N. (2018). Embedded error estimation and adaptive step-size control for optimal explicit strong stability preserving Runge–Kutta methods. *arXiv: Numerical Analysis*. <https://arxiv.org/abs/1806.08693>
- [42] Fook, H., Ian, C. A. C., Gan, W., Purnama, I. & Lew, W. (2015). Mitigation of Magnus Force In Current-Induced Skyrmion Dynamics, IEEE International Magnetism Conference (INTERMAG), Beijing, 2015. Beijing, BJ: IEEE. DOI: <https://doi.org/10.1109/INTMAG.2015.7157020>
- [43] Kovalev, A. & Sandhoefner, S. (2018). Skyrmions and Antiskyrmions in Quasi-Two-Dimensional Magnets. *Front. Phys.*, 6. DOI: <https://doi.org/10.3389/fphy.2018.00098>
- [44] Bobeck, A. H., Bonyhard, P. I. & Geusic, J. E. (1975). Magnetic bubbles—An emerging new memory technology. *Proceedings of the IEEE*, 63, 1176–1195. DOI: <https://doi.org/10.1109/PROC.1975.9912>
- [45] Bernand-Mantel, A., Camosi, L., Wartelle, A., Rougemaille, N., Darques, M. & Ranno, L. (2017). The skyrmion-bubble transition in a ferromagnetic thin film. *SciPost Phys.*, 4. DOI: <https://doi.org/10.21468/SciPostPhys.4.5.027>
- [46] Thiele A. A. (1973). Steady-State Motion of Magnetic Domains. *Phys. Rev. Lett.*, 30, 230–233. DOI: <https://doi.org/10.1103/PhysRevLett.30.230>
- [47] Romeo Juge. Exploring different facets of magnetic skyrmion nucleation and dynamics in ultra-thin films. *Materials Science* [cond-mat.mtrl-sci]. Université Grenoble Alpes, 2020. English. NNT: 2020GRALY005. tel-02947020f.
- [48] Zhou, Y., Iacocca, E., Awad, A. A., Dumas, R. K., Zhang, F. C., Braun, H. B. & Åkerman, J. (2015). Dynamically stabilized magnetic skyrmions. *Nat.*

- Commun.*, 6, 094402. DOI: <https://doi.org/10.1038/ncomms9193>
- [49] Lepadatu, S. (2020). Emergence of transient domain wall skyrmions after ultrafast demagnetization. *Phys. Rev. B*, 102, 094402. DOI: <https://doi.org/10.1103/PhysRevB.102.094402>
- [50] Li, M., Sapkota, A., Rai, A., Pokhrel, A., Mewes, T., Mewes, C., ... Sokalski, V. (2020). Experimental observation of magnetic domain wall skyrmions. <https://arxiv.org/abs/2004.07888>
- [51] Nagase, T., So, Y., Yasui, H., Ishida, T., Yoshida, H., Tanaka, Y. ... Nagao, M. (2020). Observation of domain wall skyrmions in chiral magnets. <https://arxiv.org/abs/2004.06976>
- [52] Jennings, P. & Sutcliffe, P. (2013). The dynamics of domain wall Skyrmions. *J. Phys. A: Math. Theor.*, 46, 465401. DOI: <https://doi.org/10.1088/1751-8113/46/46/465401>
- [53] Leliaert, J., Mulkers, J., De Clercq, J., Coene, A., Dvornik, M. & Van Waeyenberge, B. (2017). Adaptively time stepping the stochastic Landau-Lifshitz-Gilbert equation at nonzero temperature: Implementation and validation in MuMax3. *AIP Advances*, 7, 125010. DOI: <https://doi.org/10.1063/1.5003957>
- [54] Bernand-Mantel, A., Muratov, C. B. & Simon, T. M. (2020). Unraveling the role of dipolar versus Dzyaloshinskii-Moriya interactions in stabilizing compact magnetic skyrmions. *Phys. Rev. B*, 101, 045416. DOI: <https://doi.org/10.1103/PhysRevB.101.045416>
- [55] Sisodia, N., Muduli, P. K., Papanicolaou, N. & Komineas, S. (2021). Chiral droplets and current-driven motion in ferromagnets. *Phys. Rev. B*, 103, 024431. DOI: <https://doi.org/10.1103/PhysRevB.103.024431>